Terahertz Photoconductive Antennas Design and Modelling

From Advanced Design Strategies to Nano-Fabrication

Ruo-Bin Han

SUBMITTED IN FULFILMENT OF THE REQUIREMENTS FOR THE DEGREE OF
DOCTOR OF PHILOSOPHY

JAMES WATT SCHOOL OF ENGINEERING

COLLEGE OF SCIENCE AND ENGINEERING

07 11 2025

Abstract

The demand of high bandwidth and data transmission rate in future wireless communications is one of the most urgent problems in academia. Terahertz (THz) wave is located between the microwave and infrared region, covering a wide bandwidth in which a high potentiality of communication applications is competent. Within this spectrum, the development of THz antennas with enhanced radiation performance has become a major research focus. Photoconductive antennas (PCAs) have emerged as key components in THz systems due to their broad bandwidth, high data transmission rate, and simple structure. However, its low radiation power due to limited optical-to-THz conversion efficiency has been the problem that most plagues the academic world.

The motivation of this PhD study is to enhance the performance of THz PCAs through structural and material innovations, and to design and fabricate high-performance PCAs on this basis. Several PCA designs have been designed, modelled, and fabricated, and molybdenum disulfide (MoS_2) and graphene quantum dots (GQDs) have been incorporated into the proposed PCAs. Nano-fabrication methods of the proposed PCAs based on novel materials and nano-structures have been successfully completed. Measurements of surface current and THz radiation emission demonstrate the superiority of these proposed PCA designs. The combined research on material research, antenna structural design, successful implementation of nano-fabrication techniques, and the measurements demonstrating enhanced photocurrent and THz emission has not only provided a promising high-performance THz emission source for THz applications but also paved the way for future experimental strategies and performance characterization methods in THz PCA research.

University of Glasgow

College of Science & Engineering

Statement of Originality

Name: Ruo-Bin Han

Registration Number: XXXXXXXX

I certify that the thesis presented here for examination for a PhD degree of the University of Glasgow is solely my own work other than where I have clearly indicated that it is the work of others (in which case the extent of any work carried out jointly by me and any other person is clearly identified in it) and that the thesis has not been edited by a third party beyond what is permitted by the University's PGR Code of Practice.

The copyright of this thesis rests with the author.

No quotation from it is permitted without full acknowledgement.

I declare that the thesis does not include work forming part of a thesis presented successfully for another degree.

I declare that this thesis has been produced in accordance with the University of Glasgow's Code of Good Practice in Research.

I acknowledge that if any issues are raised regarding good research practice based on review of the thesis, the examination may be postponed pending the outcome of any investigation of the issues.

Signature: Ruo-Bin Han

Date: 31 October 2025

List of Publications

Published Paper

1. **Ruo-Bin Han**, et al. *"Advancements in terahertz-enabled photoconductive antenna design: a review."* International Journal of Microwave and Wireless Technologies. Vol 17, no 6, 977-993, 2025. doi:10.1017/S1759078725102274.
2. **Ruo-Bin Han**, et al. *"T-ray Photoconductive Antenna Design for Biomedical Imaging Applications."* 2023 International Microwave and Antenna Symposium (IMAS), Cairo, Egypt, 2023, pp. 195-198. (Won 1st prize of BEST STUDENT PAPER AWARD)
3. **Ruo-Bin Han**, et al. *"A terahertz photoconductive antenna design for gain enhancement based on the Chinese Totem Tai-Chi."* 2023 IEEE International Symposium on Antennas and Propagation and USNC-URSI Radio Science Meeting (USNC-URSI), Portland, OR, USA, 2023, pp. 615-616.
4. **Ruo-Bin Han**, et al. *"Terahertz Photoconductive Antenna Based on Tai-Chi Totem and Plasmonic Structure for Cancer Detection."* 2024 11th International Conference on Wireless Networks and Mobile Communications (WINCOM), Leeds, United Kingdom, 2024, pp. 1-6.
5. **Ruo-Bin Han**, et al. *"Terahertz Photoemitter Using Plasmonic Inter-combined Tooth Based on MoS2-GaAs Structure."* 2024 IEEE International Symposium on Antennas and Propagation and INC/USNC-URSI Radio Science Meeting (AP-S/INC-USNC-URSI), Firenze, Italy, 2024, pp. 2653-2654.
6. Tomas Pires, **Ruo-Bin Han**, et al. *"Ultrahigh Sensitive Terahertz Metasurface with 2D MoS2 for Refractive Index Biosensing."* 2024 18th European Conference on Antennas and Propagation (EuCAP), Glasgow, United Kingdom, 2024, pp. 1-5.
7. Tomas Pires, **Ruo-Bin Han**, et al. *"Hybrid Metal-Topological Insulator Terahertz Metasurface for Ultrasensitive Refractive Index Biosensing."* 2024 IEEE International Symposium on Antennas and Propagation and INC/USNC-URSI Radio Science Meeting (AP-S/INC-USNC-URSI), Firenze, Italy, 2024, pp. 2787-2788.

8. Tomas Pires, **Ruo-Bin Han**, et al. *"Comparison between a Highly Sensitive H-shape Terahertz Metasurface Absorber and an EIT-like Terahertz Metasurface for Refractive Index Biosensing"* 13th International Conference on Metamaterials, Photonic Crystals and Plasmonics (META 2023), Paris, France, 18-21 July 2023. pp. 746-747.

Paper Under Preparation

1. **Ruo-Bin Han**, et al. *"Boosting Performance of Nanofabricated MoS_2-GaAs THz Photo-emitter for Skin Cancer Detection"* planned submission: IEEE Transactions on Antennas and Propagation.
2. **Ruo-Bin Han**, et al. *"Enhancement of THz Large-Area Photo-emitter Operation based on Graphene Quantum Dots"* planned submission: IEEE Transactions on Antennas and Propagation.

Contents

List of Tables

List of Figures

Acknowledgements

First and foremost, I am extremely thankful to my dearest supervisor Prof Qammer Abbasi for all his support of my PhD study. The great help from him and our group is the source of my efficient research. With proper guidance and motivation, I am glad to work in this exciting area, and grateful to have this chance.

I would also thank my co-supervisors Prof Muhammad Imran and Prof Joao Ponciano, who provide valuable suggestions and are always helpful to give guidance whenever I need it.

Special thanks to all the friends in the Abbasi Lab group. Without the help from Dr Abdoalbaset, Tomas, Mostafa, Vimal, Noman, Shujaat, Mahmoud, and all of my dear group members, I couldn't make as much progress with the research of these years. I am also grateful to all JWNC staffs, without whose support the fabrication process will by no means be carried out. The same gratitude should be extended to Dr Hwansik who assisted me in conducting numerous THz-TDS measurements. Also, there were the lovely staffs from the University of Manchester who provided me with considerable assistance in the PCA measurements.

Finally, I feel thankful to my parents, my beloved girlfriend Mia, and my PhD friends Haotian, Ivan, YaoGe, Yifei, Huxi, Liyuan, Jingyan... for the support I have had during the difficult times I faced in this research project. Meantime, I also want to express my deep gratitude to Derrick, Allan, Alex, and Pique-see-through. The ”football days” spent with them were among the rare and truly enjoyable moments of relaxation during my PhD studies. And there's my childhood friend Charles, even though he has never been to the UK, he always accompany my life through the internet, offering me advice and sharing in the occasional Counter-Strike moments with me.

It is undeniable that there was continuous pressure during the PhD study period, especially during the time when I was conducting experiments, I was diagnosed with a tumor and needed to undergo a very risky surgery. However, my supervisor and colleagues spared no effort in supporting me, and my family and friends have also continuously encouraged me. I am extremely grateful to all those who have helped. Thank you very much.

This thesis kind of put a full stop to my student days. However, time never stops to wait for its followers. I hope this thesis can not only be a fulfilled end to my study, but also be a great start of being a researcher, constantly inspiring me to make contributions to this lovely world.

Declaration

I declare that, except where explicit reference is made to the contribution of others, that this dissertation is the result of my own work and has not been submitted for any other degree at the University of Glasgow or any other institution

---

Ruo-Bin Han

Chapter 1

Introduction

In recent communication engineering research, terahertz (THz) communication is gaining increasing scrutiny as a promising field [1][2]. THz technology has been extensively used in numerous areas such as imaging and sensing [3]. In the meantime, the combination of optical research and radio frequency (RF)/microwave (MW) technology is becoming a vital theory in order to achieve high-performance THz sources [4–8]. The THz band is the unit of frequency band that is located between the optical and microwave region, which refers to the range from 0.1 THz to 3 THz (100 GHz to 3000 GHz) [9]. Given the broad expanse of the THz spectrum and the more directional performance of THz waves, there exists significant potential for the arise of numerous novel prospects and opportunities. THz waves have a high penetration rate against various materials including wood, plastic, fabric, leather, paper, and the surface of human skin[8]. Their non-ionizing and non-invasive nature, combined with sensitivity to water, spectral specificity, penetration capability, and high resolution, make THz radiation an excellent tool for diversified utilization[10]. For instance, THz imaging is used in the medical field due to its very weak photons, which pose minimal risk to the human body[11][12]. Therefore, several new THz sensing technologies are implemented in medical use such as THz cardiovascular detecting applications[13–15]. In the new concept of healthcare 4.0, THz biosensors operating at 0.286 and 0.85 THz are used in the detection of liver and cervical cancers[14, 16, 17]. Beyond healthcare, THz sensing have been applied in many aspects such as agriculture, security, and wireless communication. THz sensing devices can assess the health of crops

at the cellular level through wireless sensor networks inside plants[18]. 6G for Urban Air Mobility (UAM) can be used to support large-scale aircraft deployments to enable on-board wireless networks[19]. Moreover, THz technology is also employed in airport security apparatus, miniaturized radars for gesture detection, THz synthetic aperture radar (SAR) imaging, and light detection and ranging (LiDAR) systems [9, 20–22]. Given the wide range of potential THz applications, the demand for reliable sources that can generate stable, high-frequency THz waves has become increasingly urgent. Several methods for generating THz radiation from RF/MW techniques and optical techniques have been investigated over the past two decades, such as frequency multiplier[23], THz vacuum tube[24], quantum cascade laser (QCL)[25], resonant tunnelling diodes (RTDs)[26] and THz photoconductive antenna (PCA). However, hybrid concepts that combine optical and RF/MW technology is more recently being developed to provide reliable THz radiation source, among which a PCA is one of the conspicuous research directions [27–29].

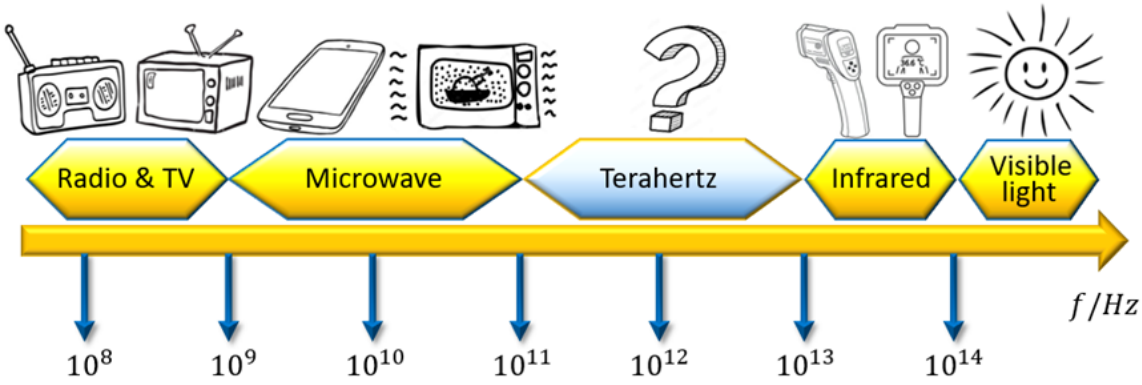

Figure 1.1: Electromagnetic spectrum illustrating the THz frequency band's placement between optical and microwave regions.

1.1 Background of THz PCA

As mentioned earlier, the increasing popularity of THz applications has been driving extensive research into the development of various THz sources. Several methods have been investigated, drawing from RF/MW and optical domains. For example, frequency multipliers, resonant tunneling diode and Gunn diode have extended MW technologies into the THz range by transferring the electronics with lower frequency to THz bandwidth upon

the negative differential resistance property [30–35], while vacuum tube sources such as travelling wave tube (TWT) and backward wave oscillator (BWO) can generate THz radiation using the free electrons emission from a MW tube [24]. Optical approaches such as THz QCL with GaAs nanometre layer separated by AlGaAs barriers have also been explored, which can deliver high output power with narrow linewidths [36] [25]. However, disadvantages of these THz sources cannot be ignored. When it comes to high frequency range, frequency multipliers and diodes suffer from extremely low output power and limited radiation bandwidth [30]. Although a BWO can generate 0.6 THz radiation with an output power up to 52 mW, it operates on the principle of interaction between electron beams and electromagnetic waves, which requires large magnetic biases and high voltage power supplies, leading to high energy consumption and bulky system size [30] [24]. QCL system requires various cryogenic cooling system because the operating temperature is commonly 210 - 261 K, and the output power markedly decreases at room temperature [37]. Meanwhile, although RTDs have shown promise as THz sources, the output power remains limited at higher frequencies [26]. These limitations have motivated the development of hybrid methods that combine optical excitation with RF/MW antenna engineering, and consequently, PCAs have attracted considerable research interest as one of the most prominent THz emitters. In the 1980s, the combination of femtosecond lasers and PCAs was first demonstrated by [38], marking a breakthrough in the field of THz research. Since then, PCAs have evolved into one of the most widely used sources of THz radiation. PCA has the characteristics of a simple structure and low cost and is uncomplicated in fabrication [39–41]. Both academia and industry have high hopes for this promising direction. According to [42], the global THz PCA market has shown a rapid growth trend since 2015, with a compound annual growth rate of 24.6% from 2015 to 2020, and a market size of 520 million US dollars in 2020. In this context, high performance PCA will certainly have its uses in THz applications. In the past decade, the exploration of PCAs has emerged one after another. As for the design concept of a PCA, it is currently believed that the three major elements affecting its performance are the intensity of the optical laser source used to excite PCA to produce THz waves, the material of the PCA electrodes and substrate, and the geometric structure design[43]. Researchers have developed THz PCAs with various structures such as bow-tie[28], dipole[44], tilting

cross[45], and interdigitated array PCAs[46], etc. In terms of materials, III-V compounds have been utilized due to their short lifetimes and high electron mobility, which are essential for efficient THz emission [47]. In addition, two-dimensional (2D) materials have attracted the attention of PCA researchers. From graphene, which has been considered in various photoconductive material applications for years, to MXene, which has become a hit recently, all of them have shown tremendous attractive characteristics in the field of optoelectronics[48]. Besides, molybdenum disulfide (MoS_2) and similar transition metal dichalcogenides (TMDs) have been proven for applications such as light harvesting and batteries[49]. Research have proven that TMDs exhibit strong light-matter interactions that are able to greatly improve the efficiency of light absorption because of the presence of band nesting and van Hove singularities in the density of states in such materials [50]. These developments in material science and structural design have underlined the continuing efforts to overcome the intrinsic limitations of conventional THz sources, opening new opportunities for high performance PCAs as promising THz emitters.

1.2 Identifying the Problem

Despite many admired advantages of PCAs that are mentioned above, the current PCA designs suffer from a fatal flaw: the extremely low optical-to-THz conversion efficiency, for the energy loss during the wave frequency step-down is nonnegligible [47]. Due to the small size of PCA, carrier transport are within micrometre-scale, even nano-scale structures, leading to a low power level, which is another reason for the low optical-to-THz conversion rate[51]. The THz radiation efficiency can only reach 0.1% in a pulsed system (PCA) and 1% in a continuous wave system (photomixer) compared to the input power of femtosecond laser [52] [53]. In the previous PCA enhancement literature, there has been a lack of joint research on the relationship between the enhancement of THz radiation and the material and antenna structure, and most of the existing literature only compares the studies on traditional substrates and electrodes with different geometric structures. Methods to

improve the THz radiation generated by PCAs are the most essential direction of PCA research at present. Furthermore, it is observed that existing PCA studies involving the use of new materials and novel structural designs at the nano-scale level have mainly focused on simulation and theoretical research, with relatively few experimental demonstrations. In one word, the biggest current challenge in the field of THz PCAs is to design high performance PCA through hybrid approaches that integrate advanced materials with optimized structures, while also overcoming the gap in nano-fabrication techniques.

1.3 Research Motivation and Objectives

This thesis is devoted to enhance the THz radiation from PCAs by addressing novelty in materials and geometric designs, and fulfill the fabrication of the proposed antennas. The motivation for this research arises from the current research gap of combining material science and advanced electrode design strategies. In addition, research on 2D materials and TMDs has been mostly applied in other photonic fields, and there is still a lack of studies applying them to PCA design. This PhD study is also motivated by consummating the use of these materials in PCAs with sufficient simulations and successful fabrication demonstrations. As discussed in the previous section, THz PCAs have been regarded as highly promising THz source. It is believed that high-performance PCAs could provide reliable, efficient, and broadband THz emitters suitable for both academic research and industrial applications, therefore addressing the current research gap is essential to unlock the full potential of THz technologies in next-generation communication, security, and medical diagnostics. In this PhD study, theoretical research on PCA materials and geometric structures is fully reviewed. Three PCA designs using various enhancing methods have also been proposed, simulated, and fabricated. The main objectives of this thesis are summarized as follows:

1. To design and model high-performance PCAs focusing on improving optical-to-THz conversion efficiency and THz emission power by utilizing hybrid methods of structural

and material innovations.

2. To apply PCA nano-fabrication techniques combining 2D materials and nano-structures, and apply high-precision fabrication of nano-structures along with novel materials such as MoS_2 and graphene quantum dots (GQD) in E-beam lithography progress.

3. To propose a PCA simulation process based on COMSOL-CST Cross-Simulation. Compared to simulations using common discrete ports, this method can obtain more reliable results.

4. To establish a PCA design framework that links material science, geometric structure, and fabrication strategies to overall PCA performance, providing guidelines for the next generation of high-performance THz emitters.

1.4 Key Contributions

The main contributions of this PhD thesis can be summarized as follows:

- This PhD study put forward a PCA modelling method based on COMSOL-CST Cross-Simulation, which provides enhanced reliability and accuracy compared to traditional CST simulation methods.
- This PhD study provides the design of a THz spiral PCA using hybrid enhancement methods combining 2D materials and nano-structures. Graphene quantum dots (GQDs) and plasmonic contact nanofingers are implemented to this PCA. The surface current measurement shows that the photocurrent is increased by GQD.
- A novel THz PCA based on TMD material and inter-combined geometric structure is also proposed in this thesis. This THz Tai-Chi PCA is based on monolayer molybdenum disulfide (MoS_2) and is equipped with plasmonic nanofingers. The measurement indicates a significant increase of the surface current due to MoS_2. Meanwhile, the nano-fabrication process of MoS_2 is also provided.

- An ultra-wideband large-area THz PCA is proposed as one of the achievements in this PhD study. This SI-GaAs based PCA design not only shows a wide operational frequency range, but also is expected to generate higher THz radiation than LT-GaAs based PCA.
- In this PhD study, nano-scale antenna electrodes are successfully fabricated with high precision. Furthermore, MoS_2 and GQD have also been applied in fabrication of the proposed PCAs, and the fabrication progress has been summarized, providing a reference for PCA nano-fabrication.

1.5 Thesis Overview

This thesis is organized as follows:

Chapter 1: Introduction

This chapter provides the overall background and motivation of the research. It introduces the essential role THz sources plays in various applications, highlights the importance of PCA research, and identifies the current research gaps in material science, electrode design, and nano-fabrication. The aims, objectives, and key contributions of the thesis are also outlined.

Chapter 2: Literature Review

A comprehensive review of the state-of-the-art in THz PCA is presented. This includes an overview of how PCA generate THz radiation at the physical level. The limitations of conventional PCAs and recent advancements with novel materials and nano-scale designs are critically discussed.

Chapter 3: GQD-Based THz Spiral PCA for THz Imaging

This chapter provides the design, modelling, fabrication, and measurement of a GQD-based THz spiral PCA for THz imaging applications such as security inspection. A Cross-Simulation Method is proposed in this chapter. The new simulation process uses surface current data from COMSOL, and the PCA in CST software is excited by the exported surface current data. This method provides improved accuracy and reliability to the simulations. In simulations, Si hyper hemispherical lens and plasmonic contact nanofingers have been utilized to enhance the radiation of the THz spiral PCA. In fabrication progress, the deposition of GQD is introduced in detail. Measurement results show that the surface current is increased after deposition of GQD, indicating an enhancement of carrier density. This results contribute to the development of GQD in the field of THz PCAs and related THz technologies by providing key information that how GQD structures influence the generation of photo carriers and surface current.

Chapter 4: THz Photoemitter Based on Inter-Combined Tai-Chi Electrodes and MoS_2-GaAs Structure for Cancer Detection

This chapter details the design methodology and numerical simulations of proposed PCA based on the shape of Tai-Chi totem. In simulations, hyper hemispherical lens and plasmonic nano-fingers are applied along with new geometric electrode designs. The simulation on human skin shows that the PCA performs well at a depth of $\approx$ 0.4 - 1 mm from the human skin surface, indicating a good prospective of this design on skin cancer detection applications. Comparisons between the proposed Tai-Chi photoemitter and other PCAs are provided, indicating a significant performance enhancement result from the use of geometric and material innovations. In fabrication, EBL has been employed to realize nano-scale antenna electrodes and plasmonic fingers, and a monolayer MoS_2 has been deposited beneath electrodes layer and substrate. Measurement results show a significant increase of the surface current due to the implementation of patterned monolayer MoS_2. This work provides a potential THz emission source for future skin cancer detection, and also contributes to the research of MoS_2 in optical-THz field.

Chapter 5: Interdigitated PCA Design for Ultra-Wideband THz Emission

Two large-area interdigitated PCAs have been designed and fabricated, one of which tested. The measurement of the tested interdigitated PCA shows that the THz radiation performance is advanced. Comparison between the proposed PCA and a reference large-aperture PCA is provided, indicating a good performance of the large-area electrode structure. The outcome of this chapter not only demonstrates the significant improvement in PCA performance by large-are electrodes, but also contributes a ultra-wideband THz photoemitter to future THz technologies.

Chapter 6: Conclusion and Future Work

This final chapter summarizes the research outcomes and highlighting the major achievements. Furthermore, several research plans in this PhD study have not yet been completed, and these have also been summarized and presented as future work.

Chapter 2

Literature Review

2.1 Theory of THz PCA

For PCA enhancement, it is generally believed that there are three major methods: improving the quality of the laser source, using more suitable materials, and designing more advanced geometric structures[43]. Since current PCA excitation is usually using 780 nm (free space laser excitation) and 1550 nm (fibre-coupled PCA) lasers excited by sapphire laser crystals, this method is not included in the scope of the PhD research. This thesis focuses on the latter two, which are materials and geometric structures. Meanwhile, PCA can also be utilized as THz radiation detector. However, this PhD study focuses on designing and modelling high-performance photoconductive THz sources, thus the PCA detectors are not included in this research. This thesis concentrates on photoconductive THz emitters (emission PCAs).

2.1.1 Optical Excitation

In the scenario of exciting a PCA, femtosecond pulses are applied instead of conventional waveguides. In practice, the laser can be coupled to the THz antenna either through air or by fibre. Currently, the most commonly used laser source is the titanium-doped sapphire (Ti^{3+}:sapphire) femtosecond pulsed laser. In typical PCA excitation process, Ti^{3+}:sapphire oscillator provides stable optical energy, while in some typical systems such as PCA arrays, high power laser modelled by amplifier is replacing oscillator laser. In a 780 nm free space laser system, the laser illuminates the PCA thorugh air. On the PCA surface, the fluence is determined by

$$F = \frac{E}{A} \tag{2.1}$$

where E is the energy of a femtosecond pulse and equals to the laser power divided by repetition frequency, and A represents the beam size. In an oscillator laser system, the repetition frequency is usually settled at 80 MHz, while an amplifier system has lower repetition frequency from 1 kHz to 1 MHz. In this PhD study, the topic is the design and modelling of PCAs excited by free space laser, thus fibre coupled laser will not be discussed.

2.1.2 THz PCA Structure and Equivalent Circuit

The THz PCA consists of a photoconductive substrate and a set of DC-biased conductive electrodes, converting the laser pump into the THz band to generate THz waves[38]. Such devices are widely accepted as a dependable source for THz generation considering their compact size and cost-effective operation. The electrodes are usually a pair of metal dipoles, while a gap is located in the center between the electrodes. 2.1 illustrates the physics of the performance of a THz photoemitter.

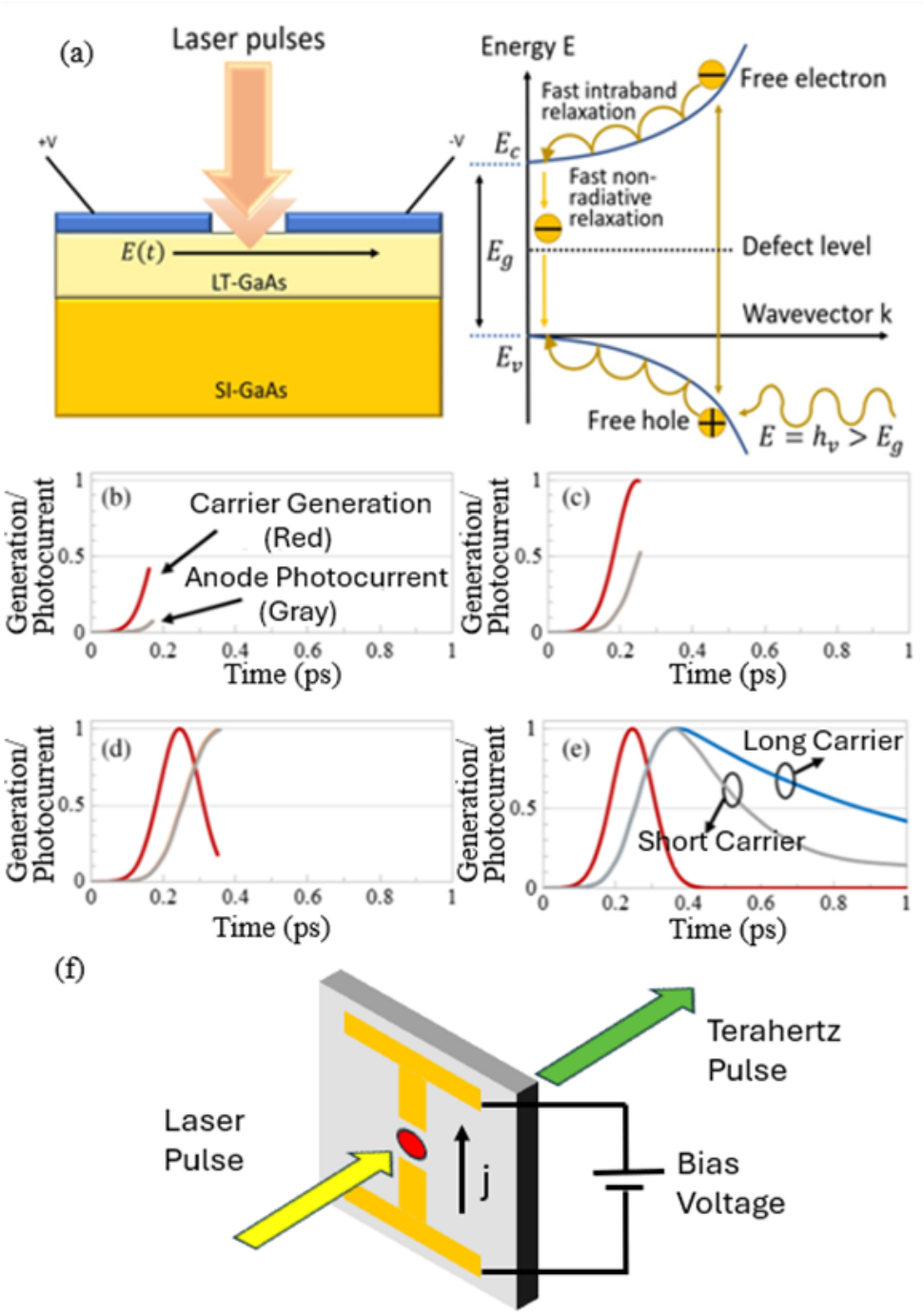

Figure 2.1: (a) The excitation of PCA by laser; (b)-(e) generation of photocurrent in semiconductors (red trace) and photocurrent in the antenna gap for the photoconductive material for long carrier lifetime and short carrier lifetime, represented by gray and blue trace, respectively [19]; (f) Illustration of a PCA. Bias voltage is applied to both electrodes and surface current is generated on the substrate.

The energy from the laser is propagated and absorbed by the substrate, while the transient photocurrent is generated between the electrodes[54][55]. Physically, the generation of THz waves is due to the surface current created by electron-hole effect of photoconductive substrates when they are driven by femtosecond laser. Laser absorption happens when the photon energy of the femtosecond pulse exceeds the bandgap of the substrate material, creating electron-hole pairs because the electrons are driven from the valence band into the conduction band. The photocarriers are accelerated by the bias voltage between electrodes. Resulting from Maxwell Equations, such sub-picosecond movement of carriers is capable to radiate THz waves. In a PCA, the required optical excitation is an ultrashort femtosecond pulse, while a device driven by continuous laser is referred as a photomixer. Figure 2.2 illustrates the physical effect inside a PCA, in which the electron-hole pairs excited by laser are accelerated due to biasing.

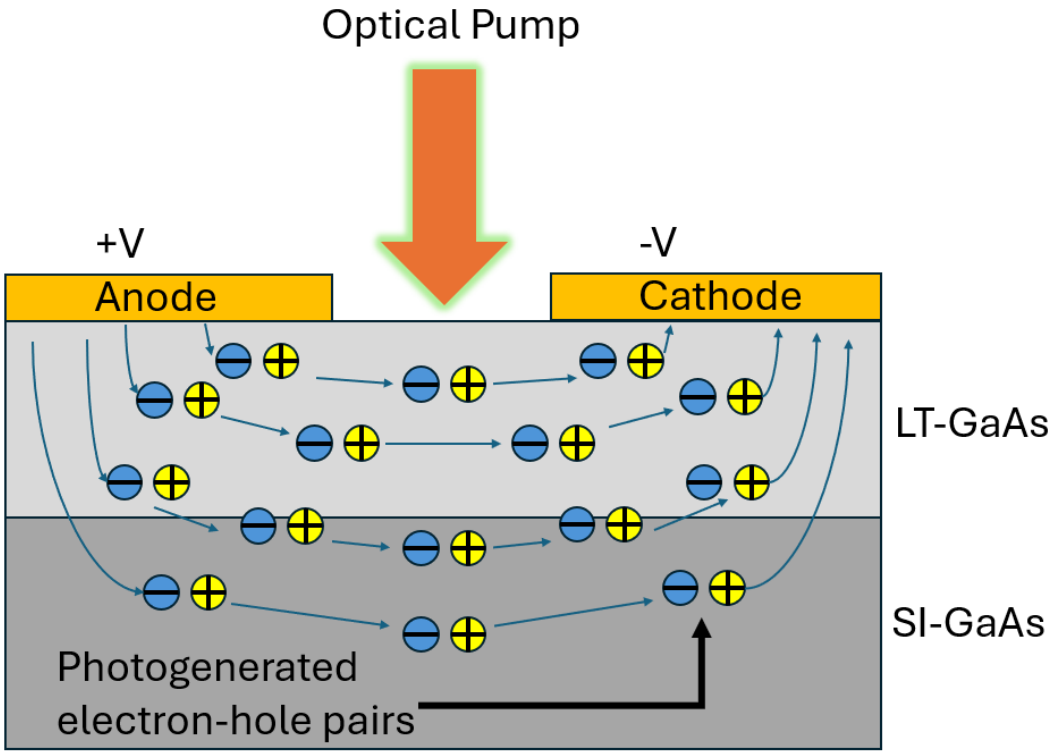

Figure 2.2: Generation and acceleration of electron-hole pairs while the laser pulse is absorbed at the PCA gap.

The semiconductor conductivity when PCA is excited by a laser pulse is given by the following equation [51]:

$$\sigma = q\left(n_e\mu_e + n_h\mu_h\right) \tag{2.2}$$

where q is the elementary charge, n_e and n_h are the concentration of the electrons and holes, and μ_e and μ_h are their mobilities. When applying bias voltage, an external field E_{bias} will drive the photo carriers and the acceleration is described as[51]:

$$\frac{dv_{e.h}}{dt} = -\frac{v_{e.h}}{\tau_{eff}} + \frac{qE}{m_{e.h}} \tag{2.3}$$

where $v_{e.h}$ and $m_{e.h}$ represent the drift velocity and the mass of electron-holes, while τ_{eff} is the effective acceleration time of carriers. E is the local field which determined by $E = E_{bias} - \frac{P}{\alpha\varepsilon_0}$, where P is the polarization due to the separation of electrons and holes, α is the static dielectric susceptibility of the substrate material, and ε_0 is the vacuum permittivity. Applying the laser and bias voltage, the accelerated carriers generate photocurrent on the material surface, which can be calculated by 2.4 [56]:

$$I_{dc}(t_d) = \frac{2}{\sqrt{\varepsilon_r}+1} \cdot \frac{h}{T} \int_0^T E_{\mathrm{THZ}}(t+t_d)\, \sigma_s(t)\, dt \tag{2.4}$$

In equation 2.4, t_d denotes the time delay before the optical pulses reach the PCA gap, while h represents the illuminated length along the detector electrode. T specifies the interval between optical gating pulses. The term E_{THz} refers to the incident THz electric field generated within the SI-GaAs substrate. σ_s(t) is the time-dependent surface conductivity at the PCA gap, which is defined as Equation 2.5[56], where R and I(t) represent the optical reflectivity and the incident optical pulse intensity as a function of time, respectively.

$$\sigma_s(t) = \frac{e(1-R)}{h\omega} \int_{-\infty}^{t} I(t') \exp\left(-\frac{t-t'}{t}\right) dt' \tag{2.5}$$

The THz electric field output can be determined by Equation 2.6, in which I_{dc} is the photocurrent within the PCA gap computed in Equation 2.4.

$$E_{THz}(t) \propto \frac{dI_{dc}(t)}{dt} \tag{2.6}$$

Additionally, free space path loss (FSPL) of THz signals can be computed by the Friis transmission equation[57], in which d represents the wavelength. In accordance with Equation 2.7, the THz frequency band experiences increased path loss compared to low frequency range. This is because the molecular absorption losses can cause significant attenuation [58].

$$\mathrm{FSPL} = 20\log\left(\frac{4\pi d}{\lambda}\right)\ [\mathrm{dB}] \tag{2.7}$$

The performance efficiency of a PCA is determined by two key components: radiation efficiency and impedance matching efficiency, defined as follows [38]:

$$\eta_r = \frac{P_r}{P_{\mathrm{in}}}, \quad \eta_m = \frac{P_{\mathrm{in}}}{P_s} \tag{2.8}$$

With these, the total efficiency of PCA can be determined by ratio of radiated power to input power, shown in Equation 2.9

$$\eta_t = \eta_m \eta_r = \frac{P_r}{P_s} \tag{2.9}$$

Therefore, the optical-to-THz conversion efficiency of a PCA is defined by the proportion of laser power concentrated on the PCA gap relative to the power of the emitted THz signal. Research conducted by [59] estimated the conversion efficiency with the following approximation:

$$\eta_{\mathrm{LE}} = \frac{P_E}{P_L} \approx \frac{eV_b^2 \mu \tau^2 \eta_L f_R}{h f_L l^2} \tag{2.10}$$

In the above equation, e and μ denote the electron charge and mobility, V_b is the applied bias voltage, τ represents the photocurrent decay time, η_L indicates the illumination efficiency, f_R and f_L are the laser's repetition rate and frequency, respectively, and l signifies the length of the PCA gap.

2.1.3 THz-TDS measurement

The PCA measurement device is THz time domain spectroscopy (THz-TDS) system, which stands out as one of the most extensively used tools for capturing THz signals, Figure 2.3 shows a typical setup of the THz-TDS system, in which the PCA is mounted between the laser and followed by parabolic mirrors.

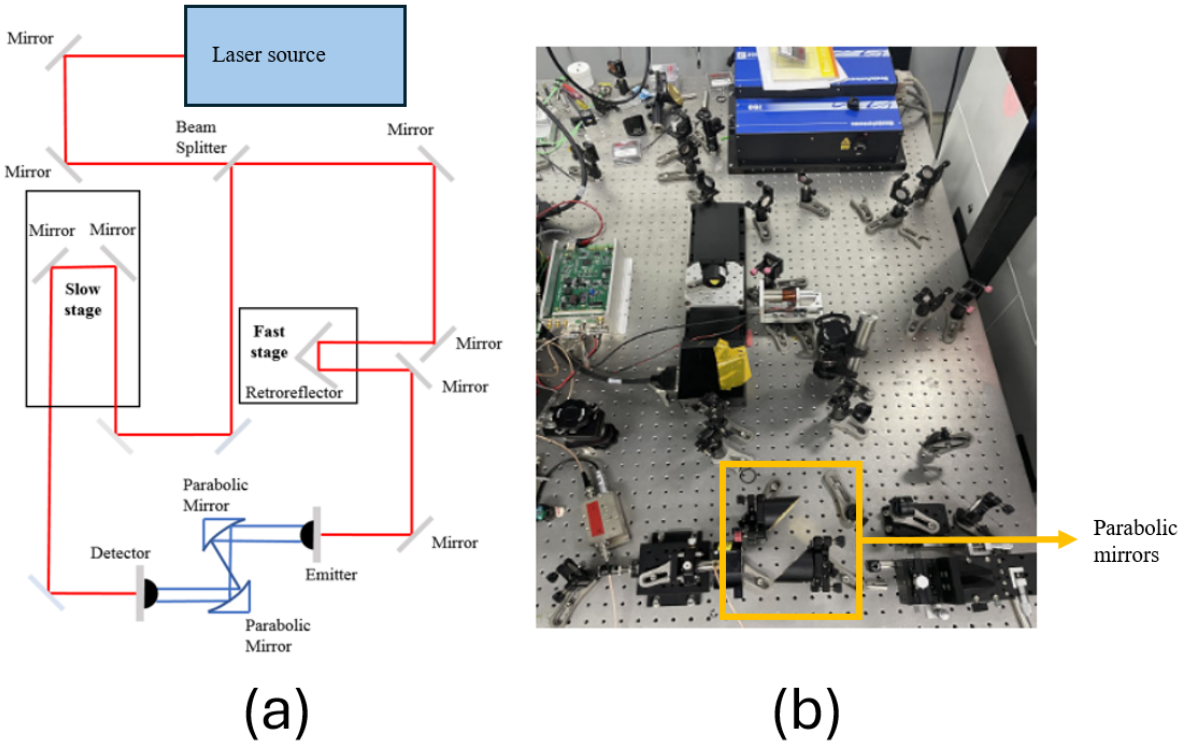

Figure 2.3: (a) Schematic diagram of a THz-TDS system; (b) A typical setup of THz-TDS system [60].

When measuring THz radiation of a photoemitter using a THz-TDS system, the optical pump is divided by a beam splitter, one of which (pump beam) is directed onto the biased PCA, the other passes through the delay line then reaches the detector. The emitted THz signals are collimated by a pair of parabolic mirrors and are focused onto the detector. Normally, a lock-in amplifier is connected to the detector, and the software system calculates the THz radiation in the time domain based on the scanned data from the delay line. By applying Fourier Transform to the time-domain signal, the power spectrum of the THz radiation in the frequency domain can be obtained.

2.1.4 Substrate Materials

In photoconductive material studies, the substrate materials are required to possess faster carrier mobility, shorter carrier lifetime, and higher resistivity. Thus, researchers have used GaAs (gallium arsenide), InGaAs (indium gallium arsenide), GaP (gallium phosphide), GaAsBi (bismuth gallium arsenide), Ge (germanium) and ZnTe (zinc telluride) in various designs[61–65]. All of these materials have the following in common: sufficiently short lifetime, excellent electronic mobility, and suitable breakdown field. Table 2.1 shows information about some commonly used photoconductive materials.

Table 2.1: Comparison of the properties of SI-GaAs, LT-GaAs, LT-InGaAs, GaP, Ge, and ZnTe

Material	Carrier lifetime (ps)	Mobility ($cm^2/V{\cdot}s$)	Resistivity ($\Omega{\cdot}cm$)	Breakdown field (V/cm)
SI-GaAs	≈100 [66]	8500 [67]	10^7 to 10^9[68]	$4*10^5$ [67]
LT-GaAs	0.3-1[69]	200[66]	10^6 to 10^8[70]	$5*10^5$[66]
InGaAs	sub-picosecond [71], larger than LT-GaAs [72]	26[73]	760[73]	$\approx 6*10^4$[73]
GaP	Between 6800 to 28100 [74]	250[74]	$1.86*10^{10}$[74]	N/A
Ge	700[75]	3900[76]	20[75]	$\approx 10^5$ [77]
ZnTe	≈ 0.5[78]	46 [78]	8.5 [78]	N/A

Among the above materials, the most widely used ones are SI-GaAs and LT-GaAs. In the second generation of semiconductors, GaAs plays an important role in the field of RF power amplifier devices. According to [79], natural materials usually lack satisfactory THz wave transmission efficiency, thus III-V compound semiconductors have become the most favoured THz photoconductive materials. This is because researchers are able to manipulate the composition of such compounds to optimize their electrical and optical properties. As mentioned earlier in this chapter, the PCA can be excited when the photon energy of laser exceeds the material bandgap. The photon energy can be easily calculated by

$$E = \frac{hc}{\lambda} \tag{2.11}$$

where h is Planck's Constant ($6.626*10^{-34} J \cdot s$), c is speed of light, and λ is the wavelength of laser. From this, the calculated photon energy of 780 nm free space laser is 1.59 eV. A typical case of SI-GaAs utilized in PCAs is that GaAs has a band gap of 1.424 eV (871 nm) at room temperature [80], which is compatible with the commonly used Ti3+: sapphire laser source and can be stimulated by such optical pump to produce electron-hole effects [47]. Meanwhile, LT-GaAs grown by molecular beam epitaxy (MBE) show high crystallinity and significantly increased carrier mobility. LT-GaAs grown from 175-250°C have extremely short carrier lifetimes (less than 1 ps) compared to SI-GaAs. Table 2.2 shows different carrier lifetimes of LT-GaAs grown at 175-300°C, indicating that at the low-temperature scale under 300°C, the higher the growth temperature, the longer the carrier lifetime.

Table 2.2: Carrier lifetimes of LT-GaAs at different growth temperature

Growth temperature (°C)	175	200	225	250	300
Carrier lifetime (ps)	0.18-0.38 [81]	0.325-0.425 [81]	0.4-0.5 [81]	0.61-0.71 [81]	1.3 [82]

In addition, THz radiation performance is influenced by the annealing temperature of LT-GaAs. A significant improvement of THz radiation is observed when the postgrowth anneal temperature exceeds 550 °C. This is because the As-Ga antisite defect is reduced at this temperature. When the annealing temperature reaches 550–700 °C, As-Ga antisites begin to migrate and annihilate each other. This process significantly reduces the density of mid-gap states that cause non-radiative recombination. As a result, the carrier lifetime increases into the sub-picosecond range, which is suitable for THz wave generation, and the resistivity also improves [83][84].

From Figure 2.4, the positive correlation between the carrier lifetime and the annealing temperature within a certain temperature range can be clearly observed. When the annealing temperature goes over 850 °C, the GaAs crystal can be damaged. Therefore, it is most appropriate to control the annealing temperature within the range of 550 - 850 °C, based on the requirements of the THz emitter.

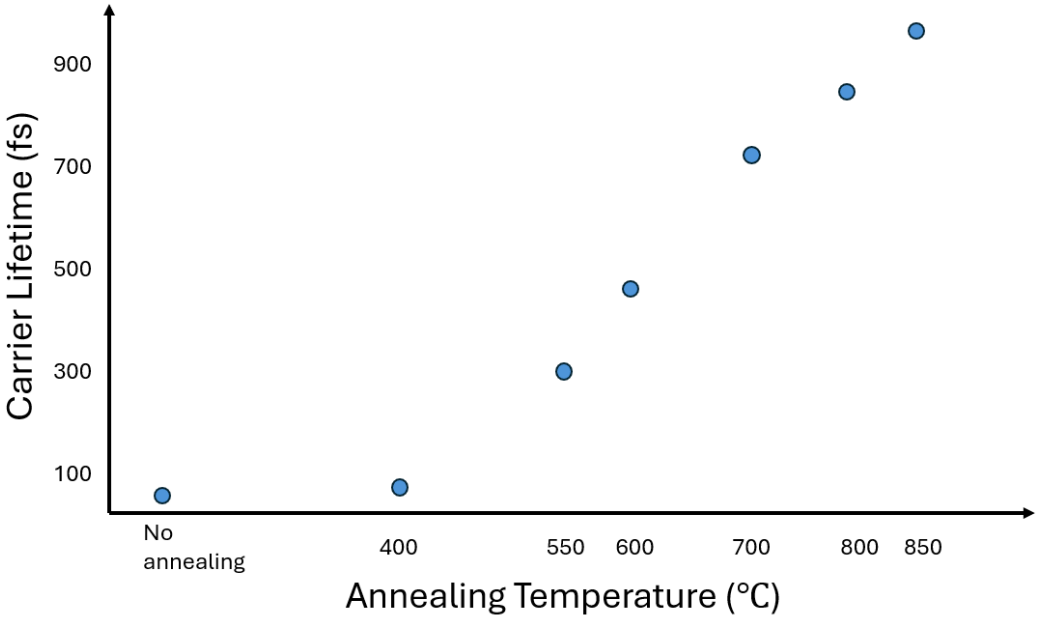

Figure 2.4: The relationship between carrier lifetime and annealing temperature in LT-GaAs.

However, the cost of LT-GaAs is extremely high compared to SI-GaAs. Therefore, as a cheaper material, SI-GaAs has been used in the proposed PCA designs in this PhD study.

2.2 Boosting THz Radiation by Si Hyper Hemispherical Lens

For most PCAs, GaAs is the substrate material, which has a refractive index of n 3.4 at THz frequencies. During the THz radiation, the relatively high refractive index leads to strongly diffracted emission at the substrate-air interface. Therefore, silicon (Si) with a refractive index of 3.4 is an ideal material for lenses [85], and the use of Si hyper hemispherical lenses with a refractive index similar to GaAs can reduce refraction losses and thus increase the radiated THz wave power. As shown in Figure 2.5, the lens can collimate THz radiation, decrease the diffraction at substrate-air interface, as well as enlarge the radiation boundary angle α because the reflection occurred at the edge of GaAs is reduced to a large extent.

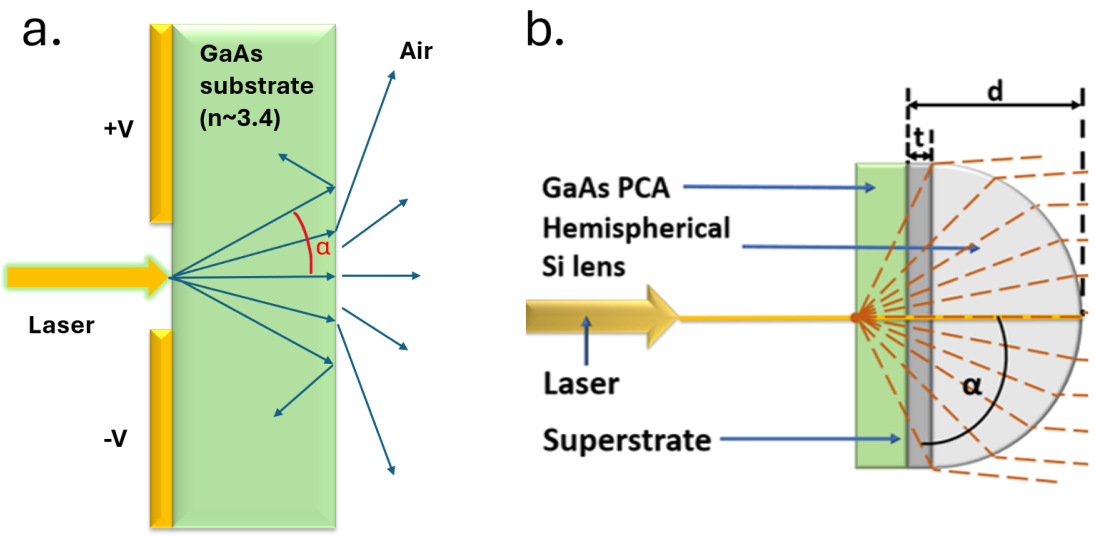

Figure 2.5: (a) THz radiation diffraction at the substrate-air interface; (b) A Si hyper hemispherical lens is applied at the bottom of PCA to increase the boundary angle and decrease the THz divergence in air.

According to the refractive index, the boundary Angle α of total reflection can be calculated by $\arcsin(n^{-1}) \approx 17.1°$, and the solid Angle Ω describing the emitted terahertz wave is [86]:

$$\Omega = 4\pi \sin^2 \frac{\alpha}{2} = 2\pi (1 - \cos \alpha) = 2\pi \left(1 - \sqrt{\frac{n^2 - 1}{n^2}}\right) \tag{2.12}$$

If the geometric structure of the hyper hemispherical lens is regarded as a joint of a standard hemisphere and a cylinder, it can be considered that the radius of the cylinder and the hemisphere are the same. The distance between the PCA gap on emitter surface and the tip on lens edge is d, presenting the thickness of the lens. The thickness of the cylinder part of hyper hemispherical lens is t. Depending on the thickness of the PCA substrate, the dimension of t alters in order to achieve high performance enhancement. To defining the dimensions of a Si hyper hemispherical lens, the relationship between the radius of hemisphere part, the thickness of lens, and thickness of the PCA is shown in Equation 2.13 [86]:

$$d + h = R(1 + \frac{1}{n}) \tag{2.13}$$

where h is the thickness of the PCA placed on the lens, R represents the radius of the sphere, and n is the refractive index ($\approx$ 3.4 for Si). The thickness of the lens $d = t + R$. Therefore, the simplified equation is:

$$d = 1.294R - h \tag{2.14}$$

The relationship among d, t, and R is also shown in Figure 2.5.

It has been almost 30 years since hyper hemispherical lens being used in collimating THz waves from PCA. As early as 1994, [87] had proposed a theoretical analysis of hyper hemispherical Si lens. Several PCA designs with Si hyper hemispherical lens are mentioned in [88], and theoretical studies and experimental results are provided to support them. This research has summarized a gain improvement of up to 13 dB by employing Si lens to PCAs. Another research has tested the enhancement of a photoemitter using a hyper hemispherical lens, in which the THz radiation is increased by 5.7% [89]. An innovative conclusion on Si hyper hemispherical lens is drawn in the research of [90], in which the detailed research and conclusive analysis of an all-dielectric meta-lens for THz PCA has been made. This research has proposed a meta-lens that consists of a single, patterned layer based on Si hyper hemispherical lens. It is capable to provide almost parallel output beam within its designed frequency range. The results show that the radiation power from the PCA equipped with the lens is improved by hundreds of μW in the THz frequency range from 0.1 to 1.5 THz. The radiation patterns of this research is shown in Figure 2.6, (a) - (c).

Recent studies also show that the design of hyper hemispherical lens can be further optimized to obtain higher enhancement of THz PCA. Research in [91] has proposed a PCA coupled with a leaky lens and the results show that the leaky lens PCA emits higher radiation (Figure 2.7 (a)). Research in [10] also indicates a 52 μW radiation power increase compared to conventional PCA (Figure 2.7 (b)). From these research, it can be concluded

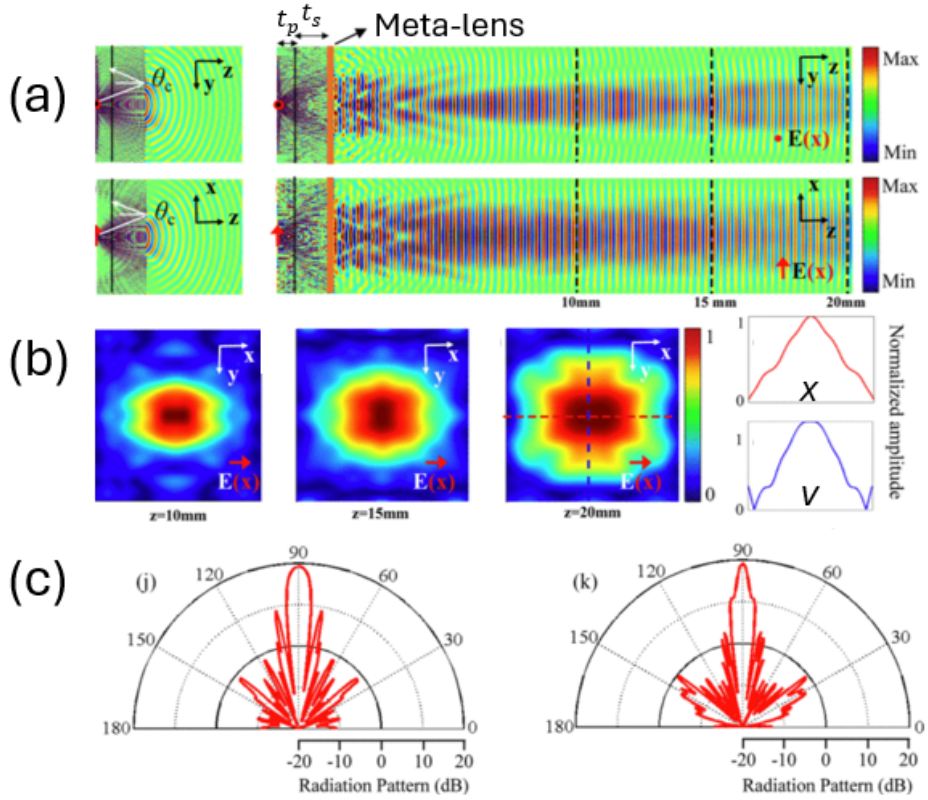

Figure 2.6: (a) Results of E-field distribution of a point current dipole PCA with the meta-lens in both y-z plane and x-z plane at 1 THz; (b) The simulation of cross section amplitude distribution in the x-y plane when z=10mm, 15mm, and 20mm; (c) 1D farfield radiation pattern of the meta-lens-based PCA on both the y-z plane and the x-z plane [90].

that elliptical leaky lens can enhance the PCA performance effectively. However, these studies are limited to simulation stage, and the subsequent antenna fabrication and measurements are not published. Nevertheless, it can still be inferred that the design of the hyper hemispherical lens can be further improved.

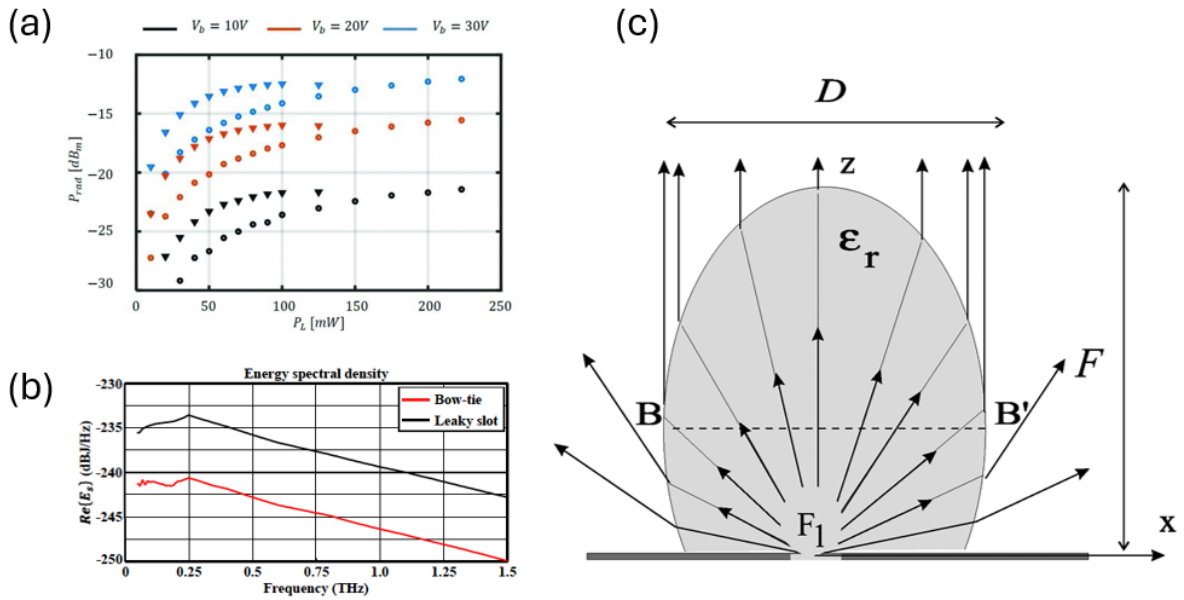

Figure 2.7: (a) THz radiation power (Prad) radiated by a standard PCA (circles) and a leaky lens PCA (triangles) as a function of laser power (Pinc) for different bias voltages in [91]; (b) Simulated energy spectral densities radiated by a conventional bow-tie (red) and a leaky lens antenna (black) in [10]; (c) Diagram of an elliptical dielectric lens in [92]. It also shows the transmitted ray picture that focuses energy toward broad side.

Although there is still room for improvement in its design, the Si hyper hemispherical lens remain one of the simplest and most efficient methods for THz PCA radiation enhancement. In spite of this, the utilization of Si hyper hemispherical lens also faces challenges. It should be noticed that the required size of the lens is influenced by the dimension of the PCA substrate, thus there can be significant differences between the results and the expected outcomes if the substrate thickness and the lens size are inconsistent. In addition, the precise alignment of the lens with THz PCA is another important challenge to be addressed during the fabrication process. Our proposed solution on the alignment problem is to use 3D printing to create a proper PCA mount, and to reserve a space at the required location on the back side for installing the lens. In this PhD study, Si

hyper hemispherical lens as been employed in simulations and actual PCA fabrications as a main approach to enhance PCA performance. Two Si hyper hemispherical lenses with difference sizes are shown in Figure 2.8. These two lenses are implemented to the fabricated PCAs in this PhD study to boost the THz radiation emission.

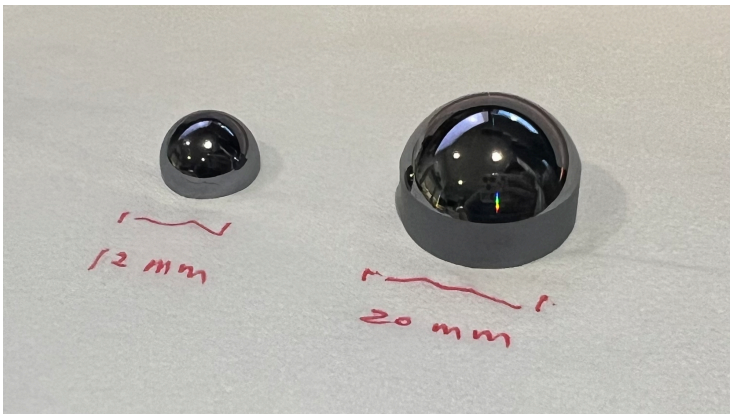

Figure 2.8: Two Si hyper hemispherical lenses provided by BATOP Company. These two lenses are implemented to the fabricated PCAs in this PhD study to enhance THz emission.

2.3 Enhancing Optical-to-THz Conversion by Material Innovations

2.3.1 MoS_2-GaAs Based Structures

During the last decade, (MoS_2) and similar transition metal dichalcogenides (TMDs) have been proven for applications such as light harvesting and batteries [49]. Research have proven that TMDS exhibit strong light-matter interactions that are able to greatly improve the efficiency of light absorption because of the presence of band nesting and van Hove singularities in the density of states in such materials [49] [50]. In recent years, monolayer and multilayer TMD, such as monolayer MoS_2 nanostructures, can effectively

reduce the loss of surface plasmon polaritons (SPPs) due to their direct band gap and powerful spin-orbit coupling, thus they become potential materials for SPPs in the next generation of 2D materials [93–96]. Figure 2.9 demonstrates the diagram of MoS_2 in molecular level.

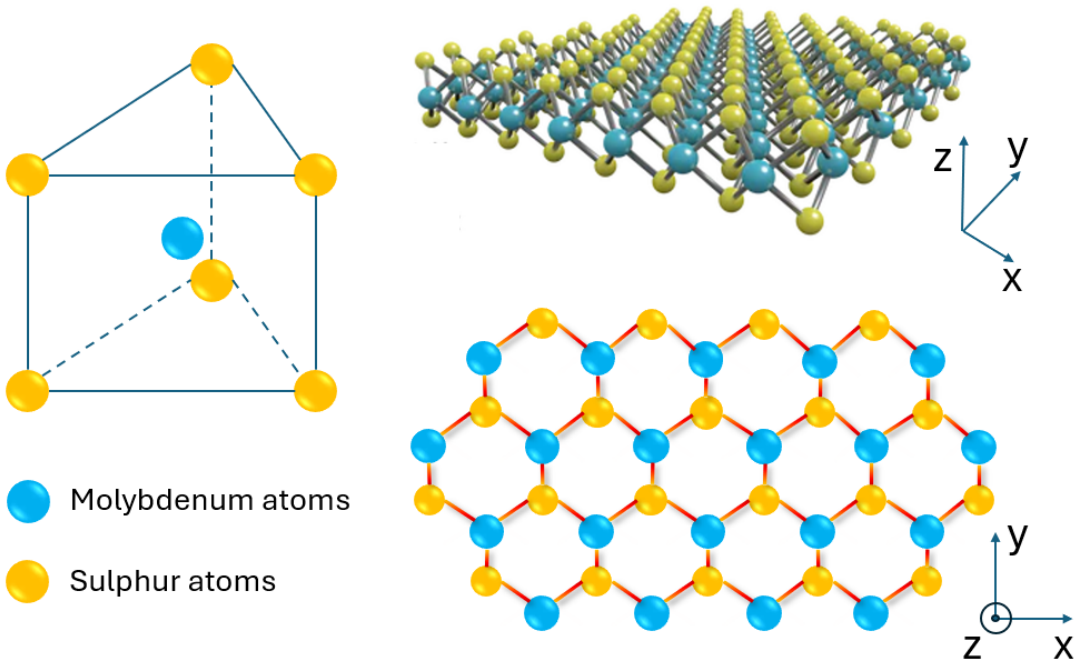

Figure 2.9: The structure of molybdenum atoms (blue) and sulphur atoms (yellow) in MoS_2 crystal.

Based on the research at the physical level, the enhancement effect of MoS_2 on optical-to-THz conversion efficiency mainly stems from the ultrafast response due to the quick thermalization of extremely non-thermal carriers, which has an increased rate because the screen effect is reduced in monolayer MoS_2 and similar 2D materials. The optical bandgap of monolayer MoS_2 is $\approx$ 1.83eV [97], which is higher than the photon energy of the 800 nm excitation laser. Theoretically, the absorption rate of monolayer MoS_2 in optical regions should be low, because the photon energy cannot exceed the bandgap. However, research shows that MoS_2 has very large laser absorption rate in its sub-bandgap region. This situation is probably due to edge states, impurities, and defects [97–100]. In research of [101], an ultrafast transient absorption of monolayer MoS_2 in its sub-bandgap region between 0.86μm and 1.4μm is reported. This research shows the ultrafast transient absorption of monolayer MoS_2 in this region can reach 6%, and the absorption enhancement can

be up to 4.2%. In research of [102], ultrafast carrier dynamics in monolayer MoS_2 is observed under time-resolved photo-luminescence and THz spectroscopy. The reaction time of photoconductivity and photo-luminescence is 350 fs. When the research come to MoS_2 crystal instead of a monolayer, it can act as an optical-to-THz conversion device, thus the absorption of laser becomes more pronounced. The process of MoS_2 crystal absorbing photon energy and generating surface current is derivated in [103], in which the surface current on MoS_2 is

$$J_s(t) = \int_0^{\delta} J(t)\, dz \tag{2.15}$$

In Equation 2.15, $J(t)$ is the current density, δ is the penetration depth of the laser into MoS_2 crystal, and dz is the distance increment into the crystal [103]. From this, the surface photoconductivity to pump fluence ratio, represented by $\sigma_s(t)$, can be computed as:

$$\sigma_s = \frac{e(1-R)\,\mu_{tr} F_{opt}}{\hbar\omega} \tag{2.16}$$

In Equation 2.16, e represents the electron charge, R is the reflectivity of MoS_2 and μ_{tr} is the transient carrier mobility. F_{opt} represents the optical pump fluence, while $\hbar\omega$ is the photon energy. The absorption enhancement efficiency of MoS_2 measured in [103] is shown in Figure 2.10 (c). In addition, in research of [104], the carrier concentration of monolayer MoS_2 gradually increases under a bias voltage, which results in an effective improvement of the laser absorption capacity. This indicates that a bias voltage can modulate the optical power conversion to MoS_2, which meets the design requirements of a PCA.

Based on the above research, this PhD study has proposed the design principles for MoS_2-GaAs THz emissions. Having Equation 2.15 and 2.16, a conclusion can be drawn that the optical absorption capacity of an entire monolayer MoS_2 film can be lower than patterned monolayer flakes, because the MoS_2 flakes are increasing F_{opt} within their small areas. In addition, to maximize the laser absorption efficiency of p-type MoS_2 and n-type GaAs, a specific layout of monolayer MoS_2 needs to be introduced, rather than simply deposit a large monolayer film that covers the PCA. Illustration diagrams of a dipole PCA with patterned monolayer MoS_2 flakes at PCA gap are shown in Figure 2.10 (a) and (b).

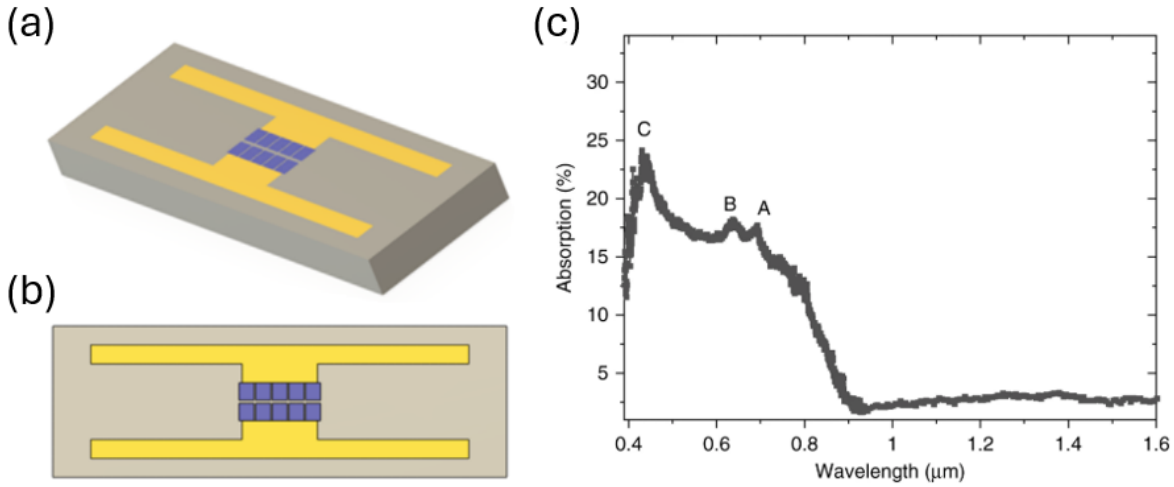

Figure 2.10: (a) (b) Illustration of patterned monolayer MoS_2 flakes deposited within PCA gap of a dipole PCA; (c) The laser absorption enhancement of monolayer MoS_2. It can be observed that the monolayer MoS_2 can increase the absorption efficiency of 800 nm laser by $\approx 14\%$.

Employing such patterned monolayer MoS_2 flakes can utilize the localized fields at the edges and ends to enhance the acceleration efficiency of photo carriers. In this case, the electron-hole pairs are mainly generated in GaAs, while MoS_2 plays the role to efficiently divide and accelerate those pairs. In this PhD study, modelling of MoS_2-GaAs PCA is given, showing the expected enhancement of THz radiation and the E-field at PCA gap. In Chapter IV, a PCA based on patterned MoS_2 monolayers has been fabricated and studied. The detected on-wafer surface current data perfectly conforms to the research and simulation that MoS_2 is boosting the surface current between the electrodes.

2.3.2 Graphene and GQD-Based Structures

Graphene, with a Young's modulus of 1.5 Tpa, an absorption coefficient of 24×10^4 cm^{-1} and a mobility of 2×10^5 $cm^2 \cdot V^{-1} \cdot s^{-1}$, has entered people's field of vision in the past decade and has become one of the options to improve the performance of PCA. The Fermi level (Ef) of the intruding graphene layer can be adjusted by tuning gating voltage [105], substrate effect [106], external doping [107], optical doping [108], and other important

means. Graphene is a single thick sheet of carbon atoms arranged in a hexagonal form [109], shown in Figure 2.11. Its optical, electrical, and mechanical properties are superior, and it is closely related to the latest semiconductor technology by regulating its properties [110].

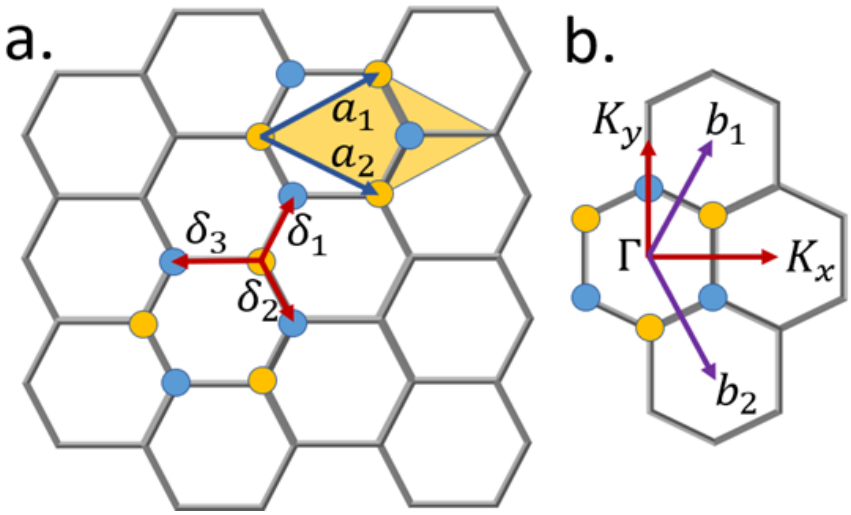

Figure 2.11: (a) Illustration of graphene hexagonal lattice, where a_1 and a_2 are unit vectors representing the sublattice and two atoms per cell. The bond length between the two nearest atoms is δ. The blue arrows represent the lattice vectors. (b) b_1 and b_2 represent reciprocal lattice vectors at Brillouin zone.

In the study of the electromagnetic properties of graphene, the Maxwell equation is first considered to simulate the propagation of electromagnetic waves along the surface of graphene [111]. However, Maxwell's equations lack analytical methods in some cases, so numerical techniques become a crucial part of guided wave propagation and scattering in graphene materials [112]. The most common numerical techniques used to analyze this problem include the finite-difference time-domain method (FDTD) [113–115], finite element method (FEM) [116][117], and the method of moment (MOM) [118][119]. Graphene models in theoretical electromagnetics research and antenna design can be simulated using a variety of commercial simulation software, such as CST, COMSOL, HFSS and FDTD Solutions [112][120].

The conductivity model of graphene at THz frequencies was first proposed by G. Hanson in 2008 [121]. Using the result expression from the Kubo formula [122], the conductivity equation is expressed as:

$$\sigma(\omega) = \frac{2e^2}{\pi\hbar}\frac{k_B T}{\hbar}\ln\left[2\cosh\left(\frac{E_F\gamma}{2k_B T}\right)\right]\frac{i}{\omega + i\tau^{-1}} \tag{2.17}$$

The constants $\hbar$, e, and k_B are the reduced Planck constant, the charge of single electron, and the Boltzmann's constant, respectively. The variables T, E_F, and τ represent the temperature, chemical potential, and relaxation time of the graphene layer. Chemical potential change ΔE_F is positively correlated with device performance. The study further shows that high-quality graphene sheets exhibit extended relaxation times, which increase electrical conductivity and thereby improve the performance. From this, it can be stated that the advantage of graphene-based PCA lies in the exceptional carrier dynamics of this material in THz frequency range. When the graphene in the PCA receives optical excitation, due to the ultra-fast carrier relaxation and relatively slow electron-hole recombination, the number of graphene particles will be reversed near the Dirac point, resulting in the real part of the conductance oscillating in the THz range [123][124]. Based on this, Dubinov and his group designed a graphene heterojunction THz emitter containing a Fabri-Perot resonator [125], in which graphene generates photoelectrons and holes, therefore THz radiation is produced because of the light-sound phenomenon driven by the electron-hole pairs in the conduction and valence bands. Researchers in PCA field are also using graphene to replace traditional metal electrodes. In [126] and [127], photoemitter and photomixer using GaAs substrate and graphene electrodes are designed and modelled, in which higher radiation efficiency have been reported, shown in Figure 2.12 (a) and (b). Research of [128] proposed a THz dipole PCA using simple graphene electrodes but obtain a high gain, shown in Figure 2.12 (e). Figure 2.12 (c) (d) illustrate the use of graphene in MIMO antennas and metasurfaces, pointing out the prospects of graphene in other THz applications [129] [130].

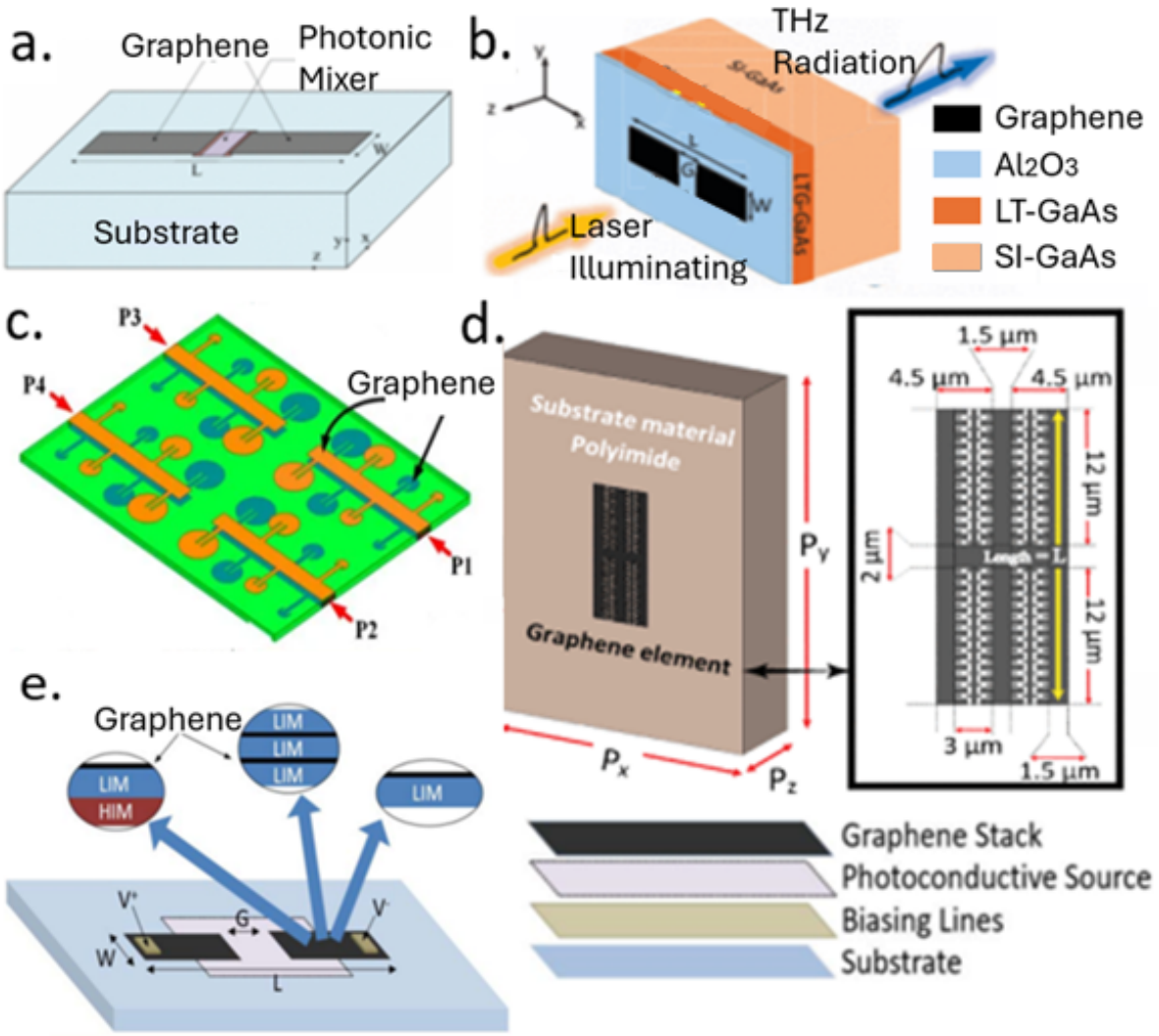

Figure 2.12: (a) A dipole PCA consists of two graphene strips placed on a substrate and integrated with a photo mixer at the antenna gap [126]; (b) A graphene-based PCA with superstrate combined with LT-GaAs and SI-GaAs [127]; (c) The schematic view of a graphene-based circular-patched Yagi-like THz MIMO antenna design [129]; (d) The schematic representation of the unit cell of a graphene-based THz sensor, while the design is a THz metasurface composed of a plurality of groups of the unit, showing a high sensitivity to THz waves on a broadband (0.2 6 THz) [130]; (e) A diagram illustrating a dipole PCA made of graphene with dimensions W×L, featuring a gap of length G and powered by a laser source. The electrodes may vary in structure, with different graphene-based stacks offering their unique benefits [128].

There are more recent studies of how graphene enhance THz photoemitters and photodetectors. Research of [131] reports a 3D graphene photodetector with a high specific detectivity of $1*10^{10}$ Jones and a response rate of up to 3.1 A/W under 980 nm excitation. In [132], the researchers demonstrates a graphene-based structure that significantly boost the coherent THz detection among unbiased THz emission devices at room temperature. [133] illustrates PCAs using nanometer scale plasmonic structures based on graphene is capable of remarkable increase in responsibility (several orders of magnitude). The design in [134] achieves a noise equivalent power of less than 300 $pW/\sqrt{Hz}$. A graphene hot-carrier fast lane is reported in 2022, which strongly enhanced THz generation by 80 times with low bias and 10 times with high bias when excited by 800 nm laser [135]. Given these, graphene is playing and will continue to play a fundamental role in the future research of THz PCA on account of its unique features exhibited in the THz band.

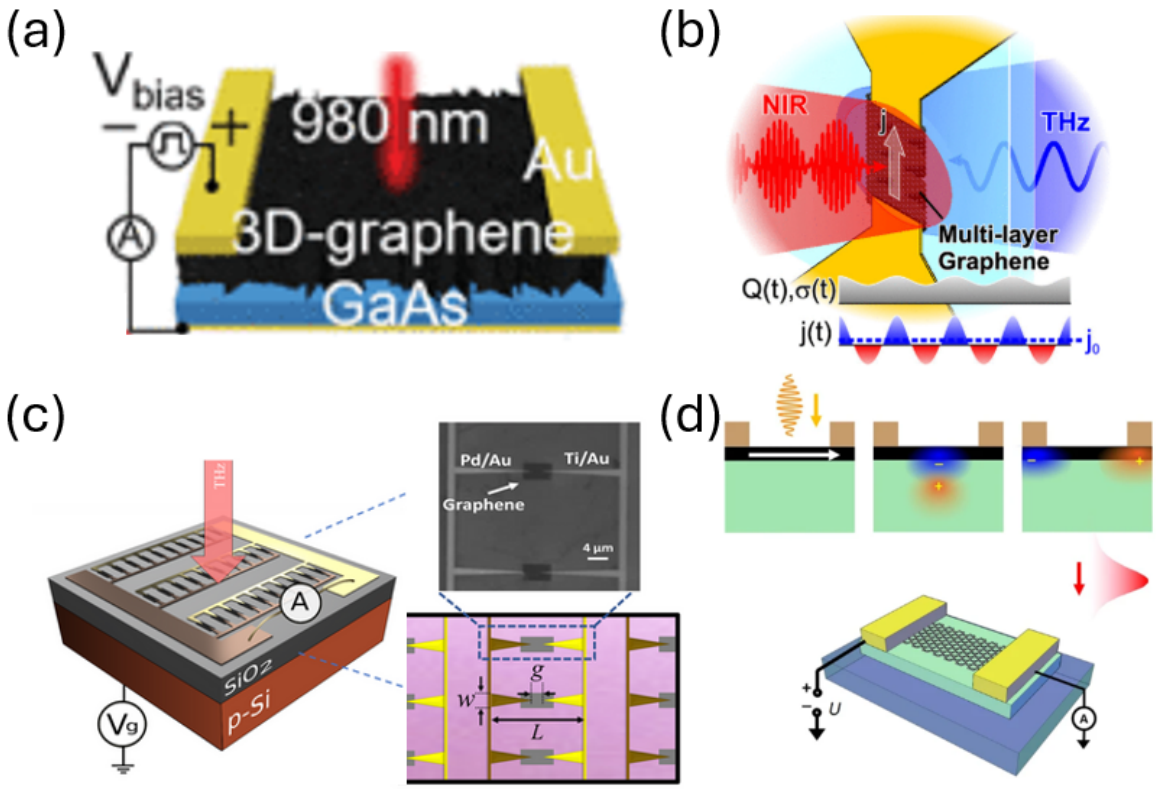

Figure 2.13: (a) The PCA decive with 3D graphene within Au electrodes in research [131]; (b) Schematic of the graphene multilayer within PCA gap for coherent THz detection via rectified photocurrent j0 [132]; (c) 3D schematic of the THz detector showcases parallel-connection PCA arrays arranged in N=15 rows and M=41 columns on a Si substrate; (d) The proposed device with a graphene hot-carrier fast lane between two electrodes [135], in which the substrate is 300 nm Si layer on top of a thick sapphire layer.

According to recent research, graphene has been more extensively used in THz photodetectors instead of photoemitters. Because of its lower conductivity compared to metals at THz frequencies, it is expected that photoemitters based on graphene structures provide lower gain. Also, being photoemitter, the THz radiation can be asymmetrical due to the slow wave influence [127]. However, it cannot be directly determined that the enhancement effect of graphene-type materials on THz photoemitters is limited. In recent years, GQD, as a new type of graphene material, has been playing an increasingly important role in the research of the THz field. GQD possesses numerous remarkable characteristics in optical-THz field, such as adjustable bandgap, edge effect, and can be applied in nonlinear optics, THz emission and detection domains [136] [137]. Research of [138] has reported that due to quantum confinement, GQD exhibits an extraordinarily high variation of resistance with temperature. In Figure 2.14, the relationship between the resistance of GQD and temperature is illustrated. A SEM figure of a typical 150 nm GQD is also shown in this figure. It should be noted that GQD can only be observed using SEM when the size is large. For most of small GQDs, the transmission electron microscopy (TEM) needs to be used in their observation.

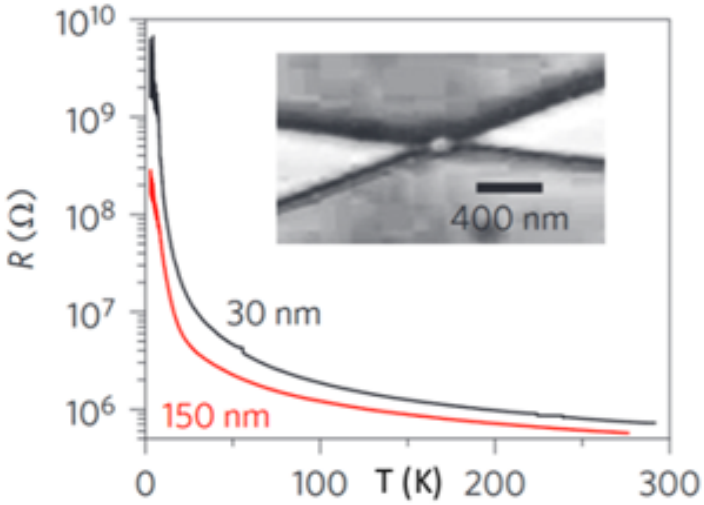

Figure 2.14: Resistance of GQD versus temperature and a SEM picture of a typical 150 nm GQD based on a bow-tie device [138].

In research of [139], the experiments of oxide GQD (GOQD) and reduced oxide GQD (rGOQD) have been conducted using THz-TDS. The results show that GOQD-based structure provides higher conductivity and carrier density when excited by a 800 nm laser with 1.3 W optical power and 79 MHz repetition frequency. Although the surface defects

within the GQD structure hindered the movement of carriers and lead to a decrease in carrier mobility, it can still be concluded that GQD is an emerging material with great prospects that is suitable for THz photoemitters. This study indicates that GQD could enhance THz radiation by increasing the carrier density at the PCA gap. The increase of carrier density on PCA when applying GQD could be due to the improved Fermi level of GQD under a sufficient bias voltage and laser power. When the Fermi level of GQD is low, the carriers are mainly in the interband conductivity regime, and there is a high carrier loss. As the Fermi level of GQD increases to a high level, the system enters the intraband conductivity regime, where the majority of the valence band states below the Fermi energy are occupied, hence less carrier loss occurs. This phenomenon is know as Pauli Blocking, illustrating in Figure 2.15. It can be assumed that when the bias voltage and laser power exceed a critical value, the Fermi energy of GQD can be increased to a sufficient level, hence the carrier density is significantly enhanced, resulting in the surface current increase on the PCA.

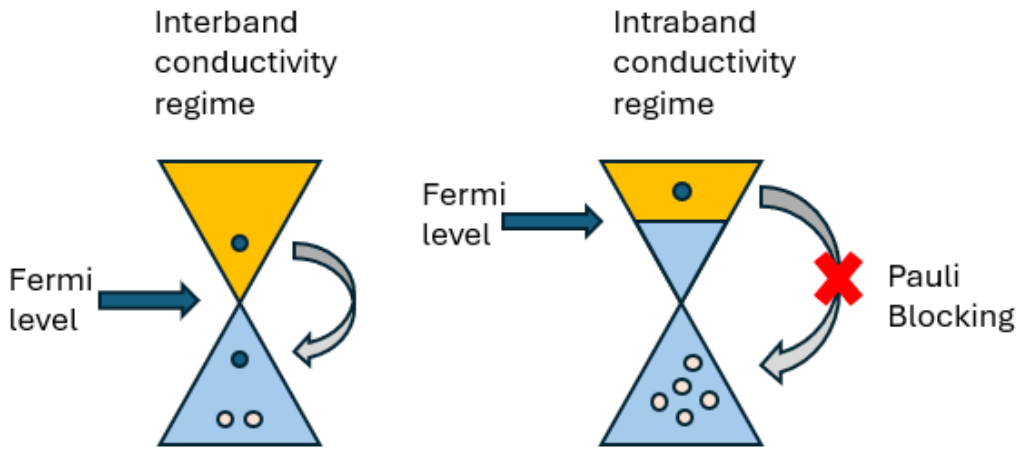

Figure 2.15: An illustration of the Pauli Blocking due to the increased Fermi level. When the Fermi level is high, the GQD becomes intraband conductivity regime and the valence energies are occupied, hence less carrier loss occurs.

Unfortunately, in recent years, there have been relatively few studies on GQD-based PCA, neither have such PCA designs been fabricated and published. Therefore, applying the GQD structure to the PCA design to enhance the performance of the carrier generation is a novel direction, but it still requires experimental validation.

Overall, instead of using graphene electrodes or applying multilayer graphene to PCA gap, this PhD study explores the enhancement of THz emission using GQD-based PCA structures. Similar to designs in Figure 2.13 (a) - (d), the GQD sheet is deposited between the electrodes, in order to enhance the carrier density within the gap area, therefore enhance the THz radiation. The detailed PCA designs and the enhancement of photocurrent is introduced in the next chapter. This PhD research proposes the design, fabrication and measurement of a GQD-based PCA. It is expected to contribute to the development of GQD in the field of THz PCAs and related THz technologies by providing key information that how GQD structures influence the generation of photo carriers and surface current.

2.4 Enhancing THz Radiation by Nano-Structures

Nanotechnology has developed rapidly in recent years, and the nano-scale fabrication industry is no longer out of reach. Currently, various nano-structures have been successfully integrated into PCA designs, most of which are at PCA gap. Some of these designs have been fabricated and proved to be effective means to improve the performance of THz wave generation, such as plasmonic structures and nano-scale semiconductor particles. These nano structures has led to a higher level of interaction between the photoconductive semiconductor and the optically pumped beam.

2.4.1 Plasmonic Concentrators

The plasmonic effect represents the interaction between the incident electromagnetic field and the free electrons in the metal concentrators, which depends on the shape, size, and spacing of the metal structure and the dielectric constant of the material [140]. They can increase the interaction between the optical pumped beam and the photoconductive semiconductor, thereby improving the absorption efficiency of the optical conductive material

substrate to the laser, thus enhancing the PCA radiation. When two plasmonic objects are close enough, the interaction between them can squeeze the field and concentrate the local field [141], allowing a great number of photo carriers to arrive at the electrodes. Thus, due to these tiny concentrators, also known as nano particles, the optical-to-THz conversion efficiency can be improved.

The configuration of the plasmonic concentrators is intended to generate surface plasmon waves when illuminated by optical pumps. Surface plasmons refer to the coherent oscillations of electrons that arise at the interface of a metal and a dielectric medium. Upon coupling with an incident electromagnetic wave, the resultant surface plasmons have the ability to propagate along the dielectric interface [142]. To couple surface plasmons with electromagnetic waves, specific conditions need to be put in place. It is necessary to ensure that the parallel wave vectors of surface plasmons and electromagnetic waves have to match, which depend on the permittivity values of the metal and the dielectric materials utilized in the corresponding structure [143]. By matching the electromagnetic waves and surface plasmon wave vectors, the nano particles patterned on the surface can promote the excitation of the surface plasmon waves [144]. This ability to generate surface plasmons provides a range of exceptional possibilities to direct and control electromagnetic waves. Such plasmonic nano particles can focus laser energy into the near field, thereby improving the efficiency of THz-emitting [145–151]. Figure 2.16 illustrates the plasmonic concentrators that positioned between the PCA electrodes.

In [51], the theoretical principle of the absorbed optical power P by the substrate in volume V can be expressed by Equation 2.18, which can explain the increase on the concentration of nonequilibrium charge carriers near the electrodes with E increased. In this equation, the enhancement of an electric field is described by the local field enhancement factor $\delta = \frac{|E|}{|E_0|}$, and σ is a medium conductivity.

$$P = \frac{1}{2} \int \sigma \delta^2 |E_0|^2 dV \tag{2.18}$$

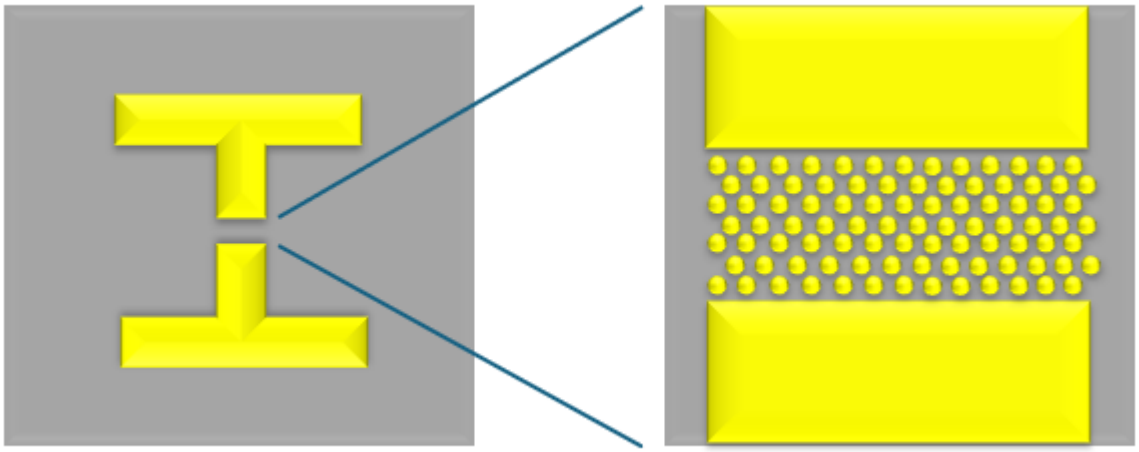

Figure 2.16: Plasmonic concentrators (also known as plasmonic nano particles) that applied at the PCA gap. The actual size of these nano particles can be smaller, from 3 nm to 100 nm.

The local electric field enhancement is due to the plasmon resonance generated in the concentrators. The plasmon resonance excited in the concentrators asymmetrically scatters the incident optical pump, redistributing the field within the semiconductor substrate. As a result, the local electric field near the electrodes becomes stronger, thereby increase the optical-to-THz conversion efficiency.

In research of [152], silver nano particles have been employed to a log-periodic spiral PCA, and the provided results show that this design obtains an enhancement of optical-to-THz conversion efficiency 2 times larger compared with another similar structure, and the strongest enhancement is around 1 THz. The research of [155], [156], and compare conventional PCA and advanced PCA with plasmonic concentrators, all based on SI-GaAs substrate and 800 nm optical pump. Similar conclusion to [152] have been made, that approximately 100% increment over 0.1 - 1.1 THz range is implemented to the radiation power. In another study, a similar nanostructure using hexagonal plasmonic concentrators is proposed. Its resulting THz field is increased by 60% compared to the conventional PCA [154]. From these studies, the conclusion can be drawn that plasmonic concentrators play an important role in enhancing the local optical field within the PCA gap, thus increasing the optical-to-THz conversion efficiency of PCA.

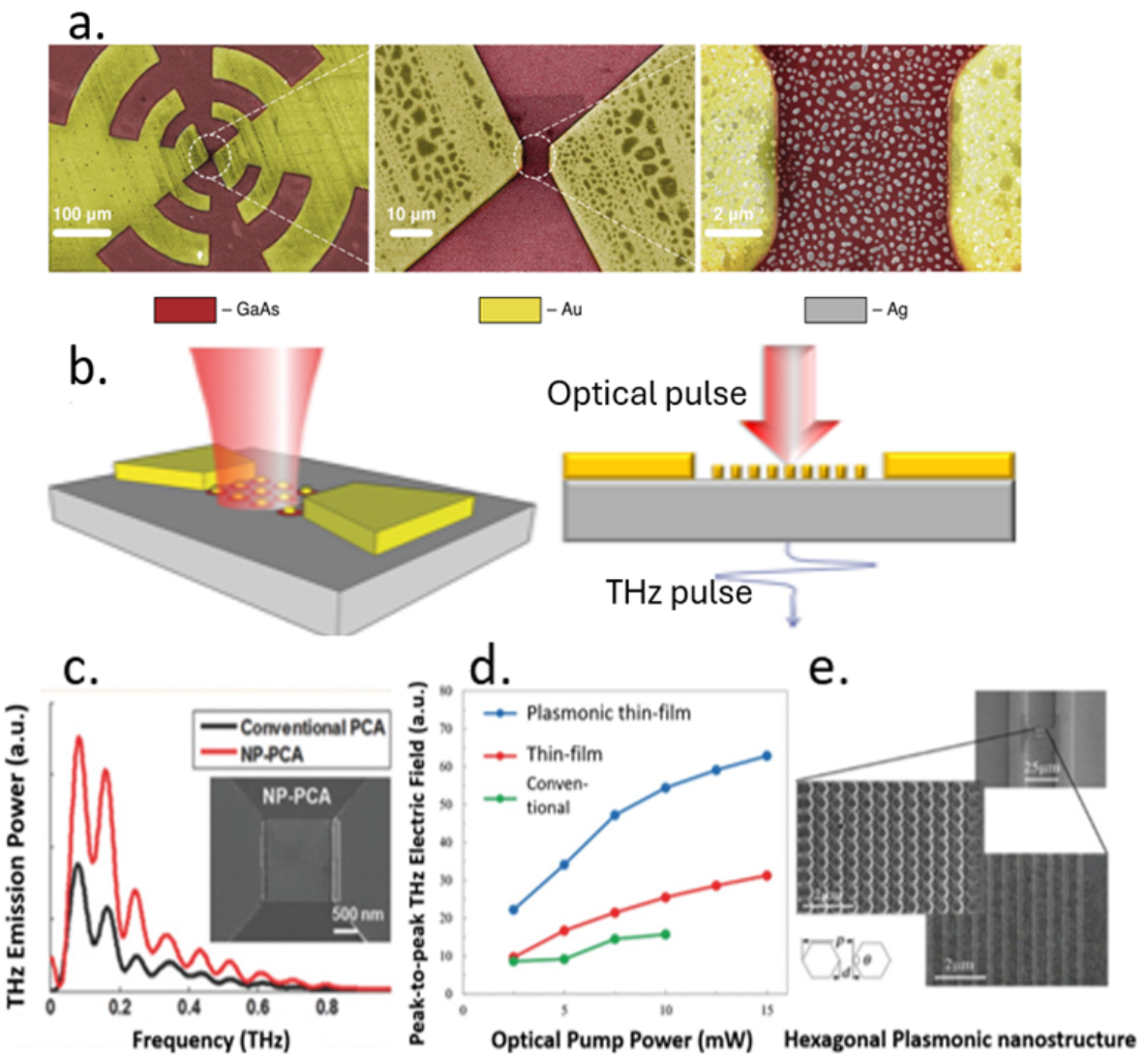

Figure 2.17: (a) Silver plasmonic concentrators (also known as silver nano particles) that applied at the PCA gap in research [152]; (b) The demonstration of a PCA with plasmonic concentrators design [153]; (c) Comparison of measured THz emission power with conventional design and plasmonic concentrators design; (d) Comparison of radiation results of PCA with hexagonal nanostructure, plasmonic light concentrators, and conventional design; (e) SEM of the hexagonal plasmonic nanostructure [154].

Although there are many advantages, challenges of utilizing plasmonic concentrators on THz PCAs are inevitable as well. Plasmonic concentrators can generate strong localized fields and high heat loss under near-infrared pumping, which leads to degradation of the PCA, resulting in unstable radiation performance [153]. The heat loss is reported as the main bottleneck restricting the enhancement of the optical-to-THz conversion efficiency of these structures [157]. In addition, the plasmonic concentrators are extremely small in size, which cause difficulty in fabrication, making it challenging to achieve repeatability in large-scale deposition. To alleviate these limitations and challenges, research on another nanostructure is reviewed. Compared to plasmonic concentrators, the next section introduces the research of plasmonic contact nanofingers, which is more capable in fabrication and is more suitable for PCAs of difference sizes and geometries. Furthermore, because the contact nanofingers are larger in size than plasmonic concentrators and directly connected to the electrodes, they are less affected by the heating effect and are less influenced by degradation.

2.4.2 Plasmonic Nanofingers

In more studies, another plasmonic nanostructure that widely utilized in PCAs to enhance the optical-to-THz conversion efficiency is plasmonic nanofingers, also known as contact fingers. Similar to the plasmonic optical concentrator, the plasmonic contact electrode can excite the surface plasmon waves and tightly confine them to the metal-photoconductor interface, thereby increasing the laser absorption in the active region of the photoconductor near the contact electrodes [158] [159]. Another advantage of using contact nanofingers is that they are directly connected to the PCA, which reduces the transport path length of the photocarriers to the device contact electrodes [160–162]. An illustration of a PCA with contact nanofingers is depicted in Figure 2.18. It can be seen that they are like extensions of antenna electrodes, making them easier to fabricate than other nano structures such as concentrators.

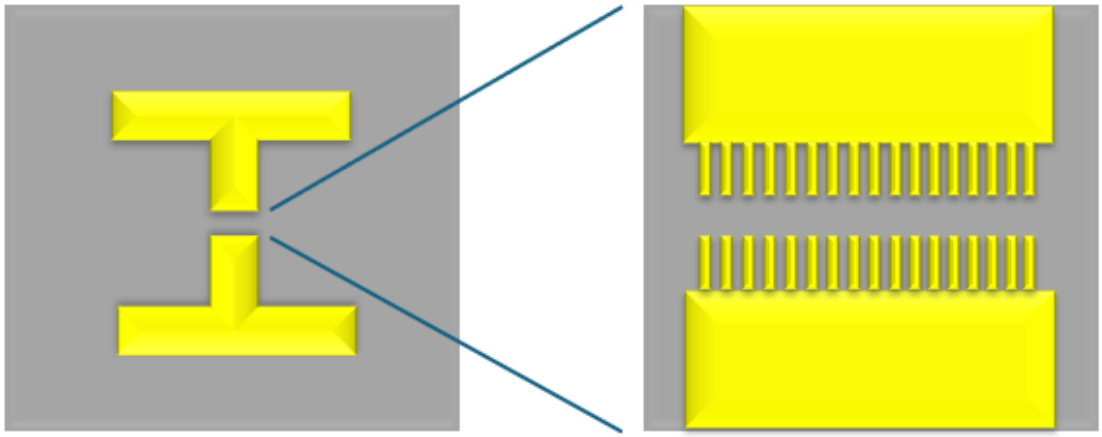

Figure 2.18: Plasmonic nanofingers (also known as contact fingers) at PCA gap.

With such contact nanofingers, a 1.9 mW THz radiation power increase is obtained at the 0.1-2 THz range in research of [163], shown in Figure 2.19 (a). Figure 2.19 (b) - (d) indicate the enhancement of PCA performance based on plasmonic contact nanofingers in different papers, all of which have reported a considerable radiation increase. In [64], unincorporated plasmonic contact fingers have improved the amplitude of THz signal by 2 times of a GaAsBi-based PCA, shown in Figure 2.19 (e). In addition, the research in [60] reports a 50% higher measured THz signal from PCA with plasmonic contact fingers at a frequency of 0.1 - 2 THz. [164] has reported a significant performance enhancement by plasmonic contact fingers, in which the THz radiation power is increased 50 times. Many studies on contact nanofingers have provided similar results, therefore the integration of plasmonic nanofingers is poised to enable substantial improvements in the performance of the forthcoming generation of high-performance, cost-effective PCAs.

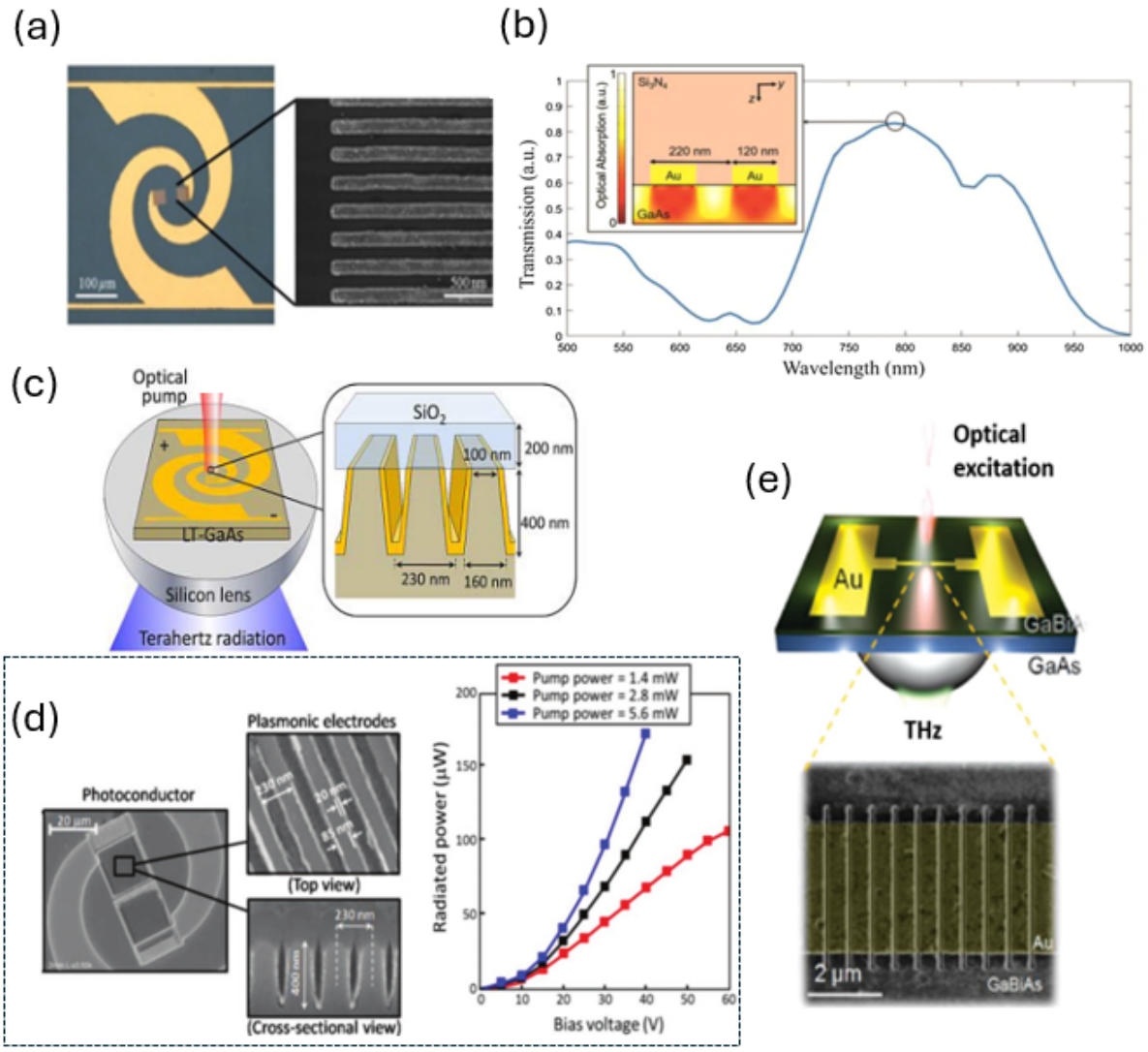

Figure 2.19: (a) A log-spiral PCA design with plasmonic contact electrodes in research [163]; (b) Figure of the increased optical transmission performance of a PCA array based on plasmonic contact nanofingers [165]; (c) (d) The demonstration and SEM of a 3D plasmonic gratings design for PCA contact electrodes and the measured radiation power comparison with different excite power of 1.4mW, 2.8mW and 5.8mW [166]; (e) The implementation and SEM figure of an unincorporated plasmonic grating at the PCA gap [64].

When contact nanofingers are applied to THz PCAs, the main challenge researchers faced is that the required precision exceeds the capabilities of traditional lithography techniques. High-resolution E-beam lithography has to be employed. Moreover, the dimensions of the nano-fingers can be further optimized to achieve higher enhancement of THz radiation. In this PhD study, E-beam lithography has been used in the fabrication of all PCA devices, and plasmonic contact nanofingers have been integrated to the proposed PCA structures to increase the radiation performance.

2.5 Large-Area Electrodes for High-Power THz Emission

For boosting THz PCA radiation by optimizing the electrode and gap structure, in addition to the nano-structures mentioned earlier, increasing the size of PCA using large-area electrodes to enable the utilize of a high-power laser excitation is also a feasible approach. In conventional PCAs, when the optical power reaches a high level, the PCAs often suffer from saturation effect, where carrier screening and recombination will limit the output THz radiation. This phenomenon occurs when the generated carrier density is large, resulting in a nonlinear response [167] [168]. To overcome this effect, employing large-area electrodes that distribute optical excitation and delay the saturation is a potential solution [47] [169].

Figure 2.20 shows the diagram of a large-area interdigitated PCA and a conventional dipole PCA. Suppose the gap of the conventional PCA is 5 μm. In contrast, the common feature of the large-area PCA is that the gap between each microstrips can also be 5 μm, and it is like an array that connects many 5 μm PCA gaps. This configuration consists

of a single anode and cathode, thus all the gaps between the open ended parallel sub-electrodes are sharing the same bias voltage. The active area of such structure can reach hundreds of μm^2 hence allows the optical pump to be spread over a larger area to reduce the saturation [170] [171].

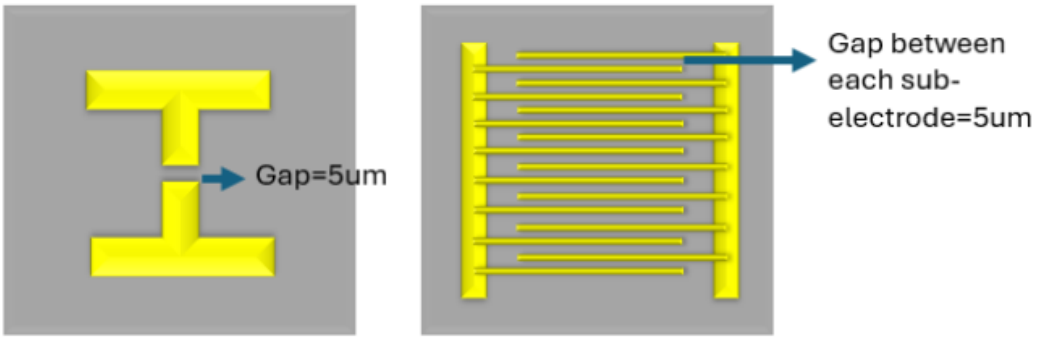

Figure 2.20: Comparison of the diagrams of conventional PCA and large-area interdigitated PCA. It can be seen that the interdigitated PCA has a larger effective area that can be excited by laser pump.

Research of [170] has proposed an interdigitated PCA with a shadow mask that blocks the incident laser from non-excitation areas, and the THz pulse emission has been increased to 85 V/cm. Another photoemitter using large-area electrodes has produced a nearly two times higher peak THz emission compared to a conventional PCA with a 3 cm antenna gap under 30 V bias voltage [172]. A $\approx$ 8.5 times THz boost and + 9.3 dB increase is achieved in the research of [173] in which the large-area PCA is coupled with tightly packed sapphire-fibre-based microlenses. Another distinctive feature is that, different from small PCAs that commonly use LT-GaAs substrate, large-area PCAs typically exhibit higher radiation power when based on SI-GaAs substrates. Study [174] has investigated the performance of interdigitated PCA based on different substrates, among which SI-GaAs substrate offers the PCA optimal radiation. Similar to this research, [160] also provides the conclusion that SI-GaAs-based large-area PCA has higher radiation power level compared to LT-GaAs large-area PCA. This is because the carrier lifetime of excess carriers in LT-GaAs is shorter, and higher carrier mobility levels are accommodated in SI-GaAs substrate, therefore a larger number of photocarriers is drifted to the electrodes within a fraction of the oscillation period of the THz radiation [81].

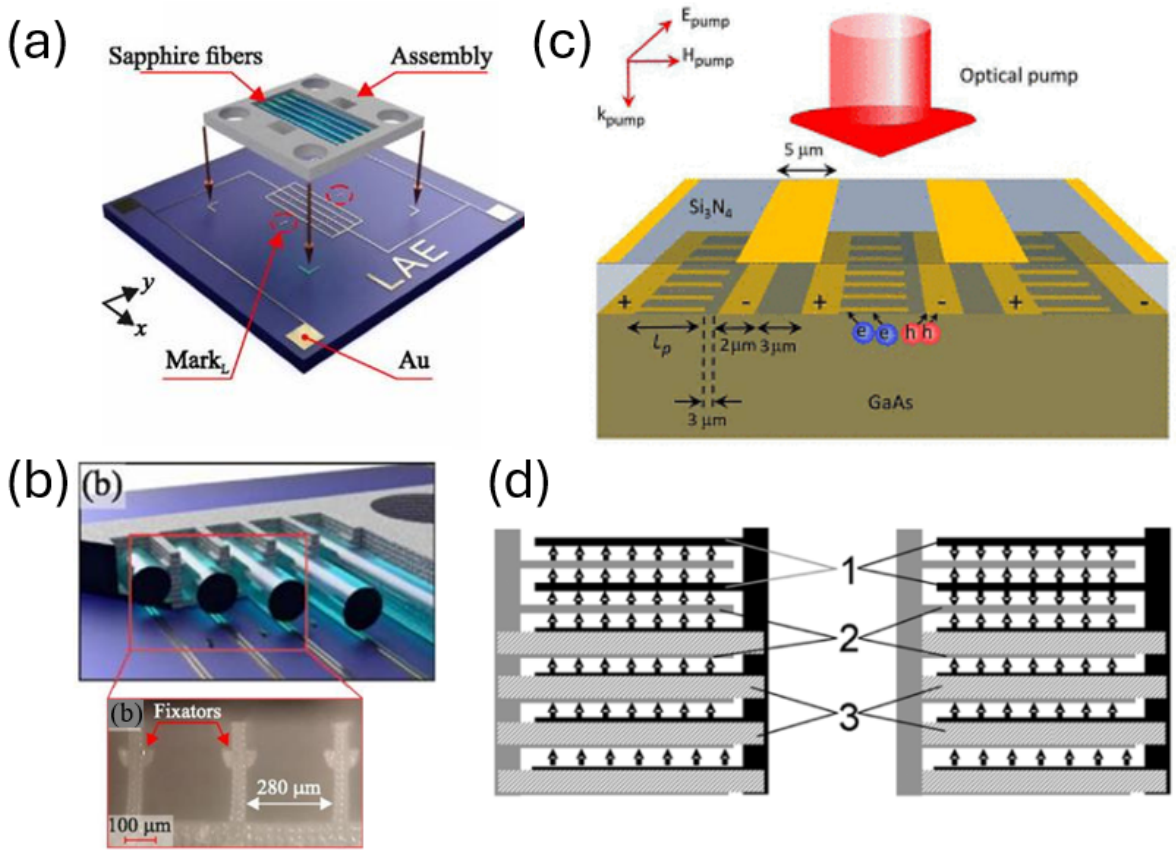

Figure 2.21: (a) A scheme of the THz large-area photoemitter with a sapphire fiber array atop [173]; (b) 3D rendering of the sapphire fibre array and the microscope image of the fixators designed to precisely hold the fibres in place [173]; (c) Schematic diagram of the large-area plasmonic photoconductive emitter fabricated on a SI-GaAs substrate [160]; (d) Layout of the interdigitated PCA design which can be both photodetector and photoemitter. 1 and 2 denote the electrodes, and 3 represents the second metallization layer. The arrows indicate photocurrents for the photocurrent when this design is used as photodetector (left) and photoemitter (right) [174].

From these studies, the feasibility of large-area PCA can be clearly demonstrated. Since the proposed designs and fabrications in this PhD study mainly use SI-GaAs as the substrate, on which large-are PCAs have shown relatively higher radiation power level, this approach is particularly applicable to the objectives of this PhD study. Additionally, because of its simple structure, large-area PCA is relatively easy to fabricate. Moreover, the principle of enhancing THz radiation by large-area excitation is straightforward, just like the old saying goes, 'Less is More'. In this PhD research, increasing PCA performance using large-area electrodes that capable of high-power optical excitation will be chosen as one of the main research subjects.

2.6 Photonic Structures for Radiation Management

2.6.1 Distributed Bragg Reflector

The Distributed Bragg Reflector (DBR) is a multilayer structure composed of two materials with different refractive indices. Each layer has an optical thickness equal to a quarter of the target wavelength. It has variable reflectance over a frequency range and can be tailored, such that at the target frequency, the reflectance reach a maximum. Diagram of a typical DBR consists of $Al_{0.98}Ga_{0.02}As$ and $Al_{0.33}Ga_{0.67}As$ layers is shown in Figure 2.22. Such DBR design has been applied to the research of [175], in which a 200 nm LT-GaAs is grown at the top of the multilayers based on GaAs substrate. The thickness of $Al_{0.98}Ga_{0.02}As$ layers and $Al_{0.33}Ga_{0.67}As$ layers are 71.5 and 64.42 nm, with a 143 nm spacer layer of $Al_{0.85}Ga_{0.15}As$ grown on top of the DBR to couple with the LT-GaAs layer. In this research, the measured THz radiation shows a performance improvement of up to 30%.

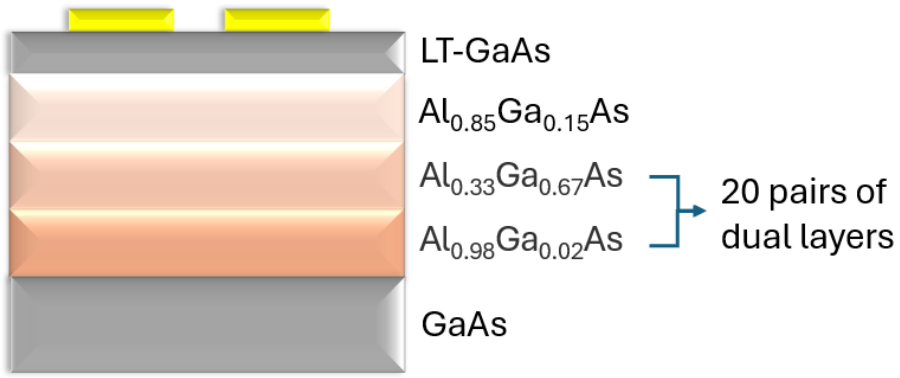

Figure 2.22: Schematic diagram of the DBR coupled to a PCA.

In research of [44], an extremely high enhancement of 5625% of the photocurrent peak compared to a conventional THz PCA has been reported when employing DBR structure and plasmonic gratings. The original PCA in this research shows a photocurrent of 35 μA, and this data has been increased to 1877 μA with the help of DBR stack layers and 500 nm LT-GaAs top layer. Moreover, study in [176] has reported that DBR increases the radiation of PCAs based on both LT-GaAs and LT-InGaAs-InAlAs substrates. The inclusion of DBR results in enhanced THz peak signals by over twice accross the overall operational bandwidth. Figure 2.23 includes the designs and outcomes in the corresponding studies.

The working principle of DBR is that it reflects the unabsorbed incident laser power back into the PCA gap between electrodes, where is the photoconductive region on the substrate. This pump recycling process results in an increase in the performance over a range of laser wavelengths. However, this technology also faces certain challenges. Its bulky structure makes it less widely used than the novel materials and nanostructures mentioned in the previous sections. Furthermore, since the thickness of each DBR layer requires nanometre level precision, molecular beam epitaxy (MBE) technique is usually required in the growth of each layer, which undoubtedly increases difficulty of PCA fabrication. Therefore, In this PhD study, DBR is studied as a reference, yet not fabricated in any of the proposed designs in the following chapters.

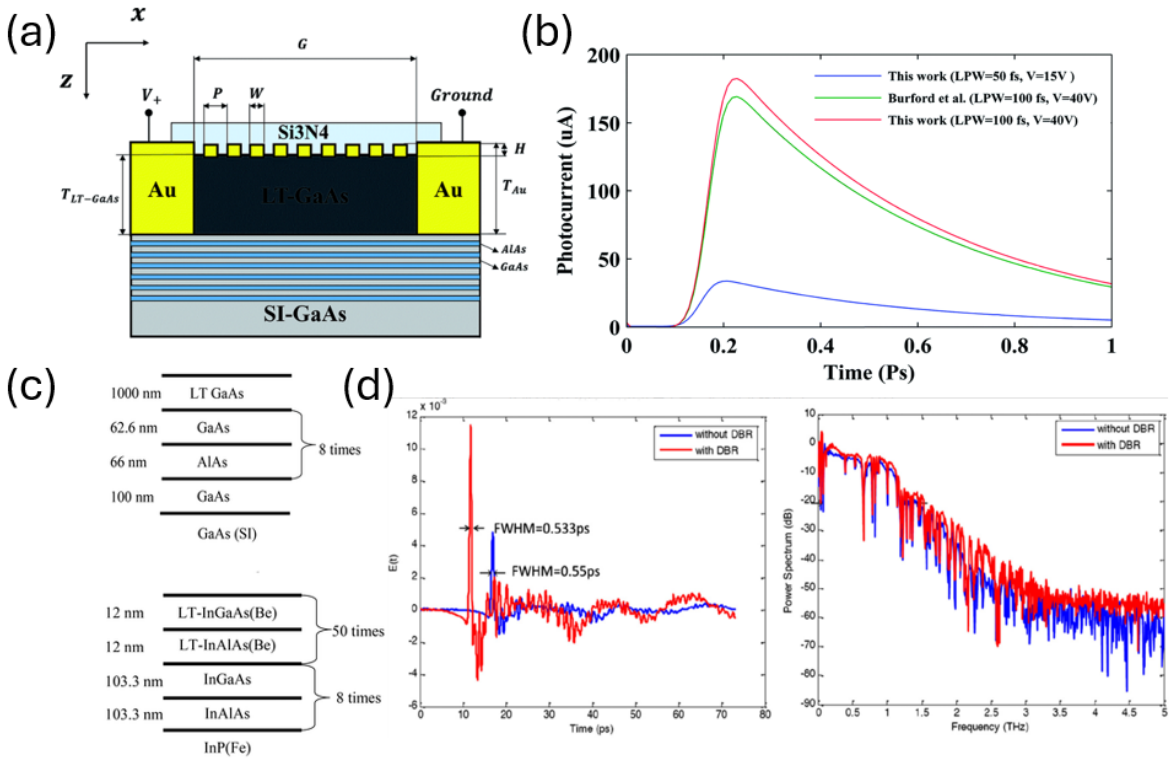

Figure 2.23: (a) Schematic diagram of the PCA with DBR and Si3N4 antireflection coating (ARC) [44], the PCA gap G is 5 μm and the LT-GaAs layer (black) on the DBR is 500 nm thick; (b) The comparison between photocurrent of this work and another published work [44]; (c) Physical structures along with the layer thickness of the DBR-coupled LT-GaAs PCA and LT-InGaAs-InAlAs PCA in [176]; (d) Measured THz radiation and power spectrum with and without DBR [176].

2.6.2 Photonic Crystals

Photonic crystal structure is another new geometric design that is capable of boosting the performance of PCA, and it is suitable for PCA designs with thick substrates [177]. A typical photonic crystal with hexagonal lattice of air holes drilled into the substrate is shown in Figure 2.24.

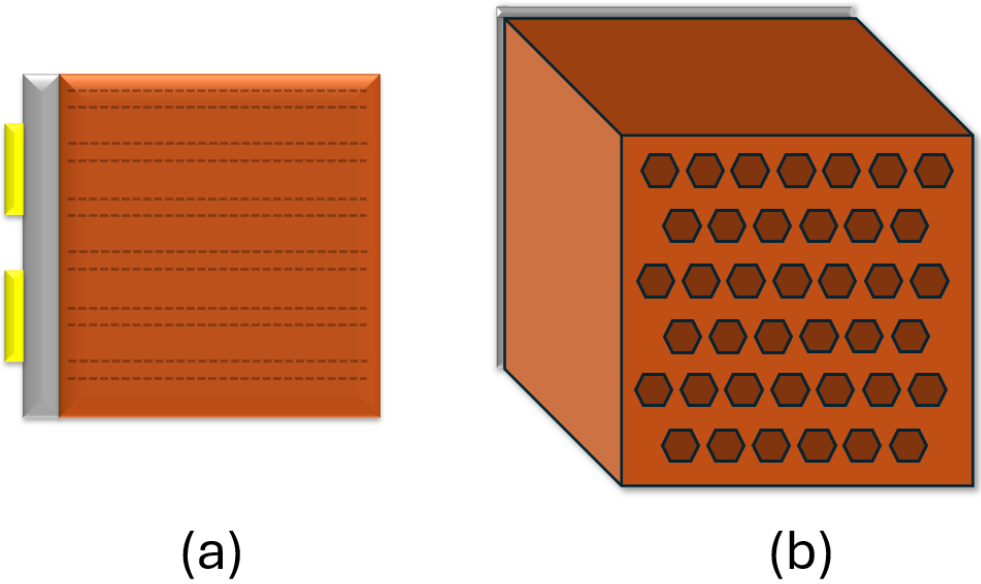

Figure 2.24: (a) Side view and (b) Back view of a photonic crystal at the bottom of a PCA. The array of hexagonal lattice of air holes are distributed in the photonic crystal.

This photonic crystal structure is equivalent to increasing the thickness of the PCA substrate. Such design based on undoped GaAs crystal has been studied in the research of [178], in which it is concluded that the radiated power is mostly directed along the axis of the air holes, keeping the main lobe of radiation pattern toward the z-axis in the overall operational bandwidth, for the defect core region plays a similar role to a waveguide. It is also reported that the trapped power in the substrate can be decreased by the photonic crystal, hence the radiation can be improved because of the reduced power leakage. In this research, the average radiation efficiency is increased by 14% from 0.65 to 1.45 THz. The

research in [179] also proposes a PCA based on photonic crystal substrate with cylindrical air holes, in which the directivity has been increased by 3.3 dBi. Figure 2.25 shows the schematic diagrams of the photonic-crystal-based PCAs along with simulation results in corresponding research.

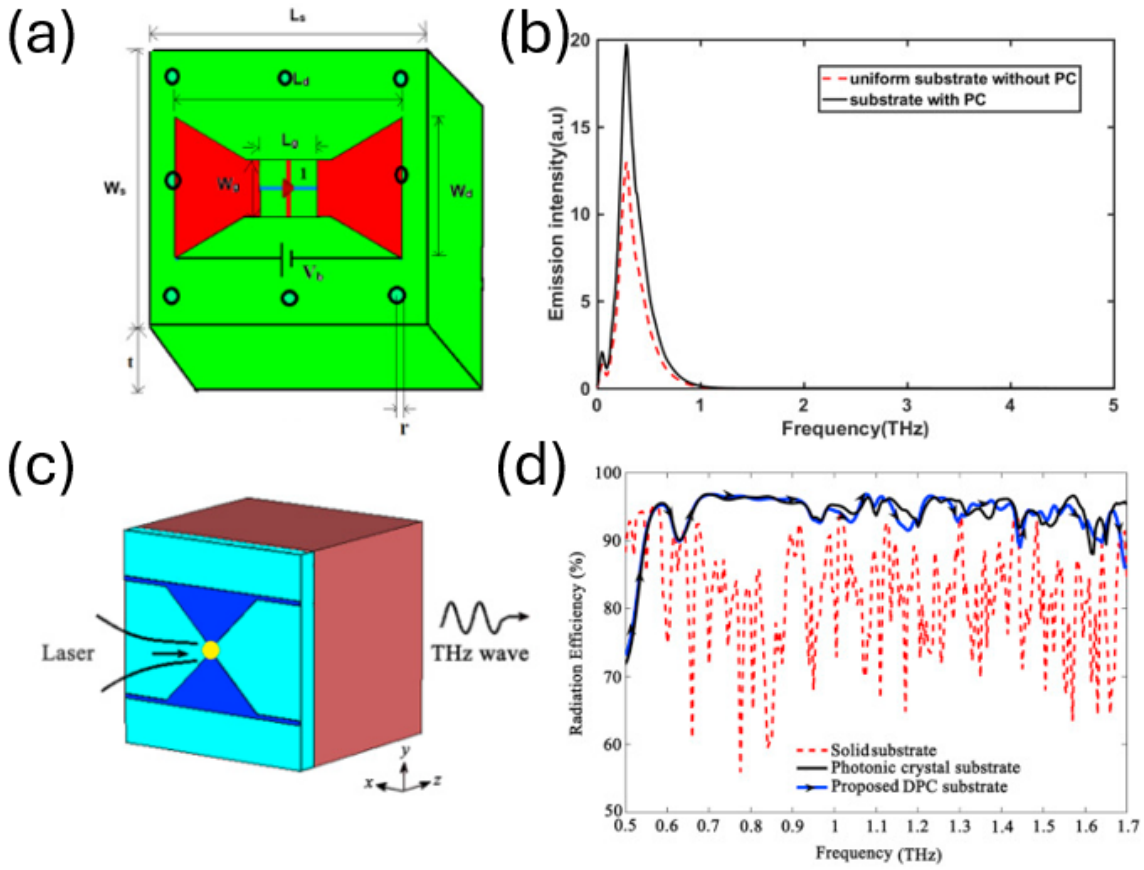

Figure 2.25: (a) A Graphene Bowtie PCA based on a photonic crystal substrate with cylindrical air holes [179] and (b) The emission spectrum of this PCA; (c) Schematic diagram of the THz PCA based on a defective photonic crystal [178] and (d) The simulated radiation efficiency of this structure compared to a PCA based on conventional photonic crystal and a PCA based on normal GaAs substrate [178].

Although this design has some potential, it has many limitations in fabrication, such as drilling holes can be challenging, and the excessive thickness causes inconvenience to measurement. This may explain why relatively few studies have focused on this method, with most remaining at the simulation stage and lacking actual fabrication demonstrations. Therefore, the research on photonic crystal is only used as a reference in this PhD research and has not been applied to the following PCA designs or fabrications.

2.7 Discussion

In this chapter, various methods for enhancing the performance of PCAs have been reviewed. A comprehensive comparison is presented to identify the applicable approaches for implementation in the proposed PCA designs in this PhD research.

As one of the most widely adopted methods for improving THz radiation emission of PCA, Si hyper hemispherical lens has been utilized to this PhD study despite the requirement for careful alignment with the PCA. Research has shown that MoS_2 can enhance THz radiation by increasing the optical absorption of the PCA. Although the fabrication of monolayer MoS_2 is relatively complex, it is still considered as one of the most promising approaches for improving THz radiation in this study. Graphene and GQD also show strong potential in the PCA field. However, the research on properties of graphene shows that it is more suitable for PCA detectors, therefore graphene is not adopted in the PCA designs in this PhD study. The use of GQD in PCAs is still limited, but theoretical studies suggest that GQD could potentially increase carrier density, thereby enhancing the surface current and THz radiation emission of PCAs. Plasmonic concentrators are not employed in this work because of the challenges of achieving high-quality fabrication within overall PCA gap. In contrast, plasmonic contact nanofingers are incorporated into the proposed PCA designs due to their ease of fabrication and the reliable performance enhancement according to literature review. The method of using large-area electrodes is also implemented in this study to enhance PCA performance, as this method has straightforward but solid theoretical proof, and its fabrication and measurement processes are relatively simple. Although photonic crystals and DBRs can also enhance PCA performance, they are not implemented in the proposed PCA designs due to their extremely complicated fabrication procedures.

In summary, the THz PCAs designed in this PhD research incorporate Si hyper hemispherical lens, MoS_2, GQD, plasmonic contact nanofingers, and large-area electrodes as the key enhancement strategies.

2.8 Summary

This chapter conducts a detailed literature review on the physics of THz PCA and methods for enhancing its performance. A PCA converts an optical pulse into THz radiation using a pair of electrodes, a photoconductive substrate, and external bias voltage. A common THz PCA uses III-V compounds as substrate material, such as GaAs and InGaAs. For most of designs, a Si hyper hemispherical lens can be coupled at the bottom PCA to collimate the THz radiation. On the surface, the optical power is absorbed when laser beam is focused at PCA gap, then the excitation and fast recombination of electron-hole pairs occur in the the photoconductive substrate. Photocurrent is generated when carriers accelerated between biased electrodes at the PCA gap. Because of the ultrafast acceleration and recombination of carriers that happened in sub-picosecond time scale, the generated radiation will be located within THz range according to Maxwell Equations. This entire process is the optical-to-THz conversion. To drive the electron-hole effect in the substrate, it is required that the photon energy of the optical pump is higher than the bandgap of the photoconductive material.

After the basic physics of THz PCA, the narrative goes to novel materials, nano structures, and external devices that enhance the performance of PCA. 2D materials such as MoS_2 and graphene have been highlighted, as well as plasmonic concentrators and contact fingers have been put forward. Benefits from these methods include concentrating optical and electric field at PCA gap, boosting local generation and drift fields of photo carriers, thereby improve the optical-to-THz conversion efficiency. Large-area eletrodes that enable higher fluence is also discussed due to the reduced saturation under high-power optical

excitation. Furthermore, several methods using photonic structures like DBR to modulate THz waves radiated by PCA are discussed. These theoretical research has provided a solid base for this PhD study, and has set the direction for the following experimental work, PCA designs and fabrication in the next few chapters.

Chapter 3

GQD-Based THz Spiral PCA for THz Imaging

3.1 The COMSOL-CST Cross-Simulation Method for PCA Excitation Based on Surface Current

Researchers using CST simulations usually rely on discrete ports to excite PCAs in current studies. However, this approach does not align with the surface currents generated when femtosecond lasers irradiate the PCA surface in reality. To enhance the realism and reliability of PCA simulation, a cross-simulation method is proposed in this PhD study. COMSOL is used to simulate the surface current distribution of substrate (GaAs) under optical excitation, and then this current data will be imported to CST so that researchers can use this as the excitation source to drive the photoemitter. This method can more closely approximate the real carrier dynamics, thereby improving the accuracy and reliability of the simulation results. The software used to obtain photocurrent is COMSOL Multiphysics 6.0, and the PCA is modelled in CST Studio Suite 2020. In COMSOL, the simplified PCA structure is built, and a 800 nm Gaussian beam is focused on the GaAs surface. The diameter of beam size is 5 μm. Hole Auger coefficient and electron Auger

coefficient are $7 * 10^{-30} cm^6 \cdot s^{-1}$. Shockley-Read-Hall (SRH) electron lifetime and SRH hole lifetime are $4.8 * 10^{-12} s$. In this example, the pump is set at time = 2 ps, while the pump period is 100 fs. The laser power *Pave* is 10 mW. The detailed parameters of the simulation is listed in Figure 3.1.

E0	sqrt((Pave*8*n0)/(fp*Dx*Dy*Dt))...	1.2501E8 V/m	E-field
Pave	10[mW]	0.01 W	Average Laser Power
fp	80[MHz]	8E7 Hz	Rep Freq of Laser
ad	5[um]	5E-6 m	PCA gap
C_p	7*10^-30[(cm^6)/s]	7E-42 m^6/s	Hole Auger coefficient
C_n	7*10^-30[(cm^6)/s]	7E-42 m^6/s	Electron Auger coefficient
hc	6.63*10^-34[J*s]	6.63E-34 J·s	Plank Constant
Dx	5[um]	5E-6 m	Gaussian dependence on x
Dy	5[um]	5E-6 m	Gaussian dependence on y
Tn	480*10^-14[s]	4.8E-12 s	SRH electron lifetime
Tp	480*10^-14[s]	4.8E-12 s	SRH hole lifetime
n0	377[ohm]	377 Ω	Impedance of free space
c	3*10^8[m/s]	3E8 m/s	Speed of light
Dt	100[fs]	1E-13 s	Pulse period
ni.eff	1.23*10^12[1/m^3]	1.23E12 $1/m^3$	Carrier concentration
gap	5[um]	5E-6 m	
V_p	0[V]	0 V	
V_n	15[V]	15 V	
lda	800[nm]	8E-7 m	
f1	c_const/lda	3.7474E14 1/s	
t0	100[fs]	1E-13 s	Pulse period
t1	2[ps]	2E-12 s	Pulse time

Figure 3.1: The detailed parameters of the COMSOL simulation.

In this PhD study, it is necessary to compare and analyse the proposed PCAs, hence a reference PCA is required as the comparison object. A common but reliable electrode design has been applied to the comparisons and analysis as an invariant. Dipole shaped electrodes are employed because this design has been widely studied and used over the past decade. This design provides reliable performance and make it an appropriate start for the subsequent study. A typical dipole THz PCA based on a 10 μm SI-GaAs substrate is introduced from the research of [180], and this dipole design is used as the reference PCA in this thesis so as to be compared and analyzed with the proposed PCA designs in this PhD study. This reference dipole PCA design is also used as a prototype for illustrative simulations in the narration COMSOL-CST cross-simulation method. In the

COMSOL simulation, the first step is to create a GaAs substrate, and then build up two gold electrodes on the surface. The height of GaAs H is set as 10 μm, while the length L and width W of the GaAs substrate are 60 μm and 15 μm. The thickness of gold electrodes have been set to 100 nm. What is more, it is necessary to surround the GaAs with air in COMSOL. The PCA structure in COMSOL is shown in Figure 3.2.

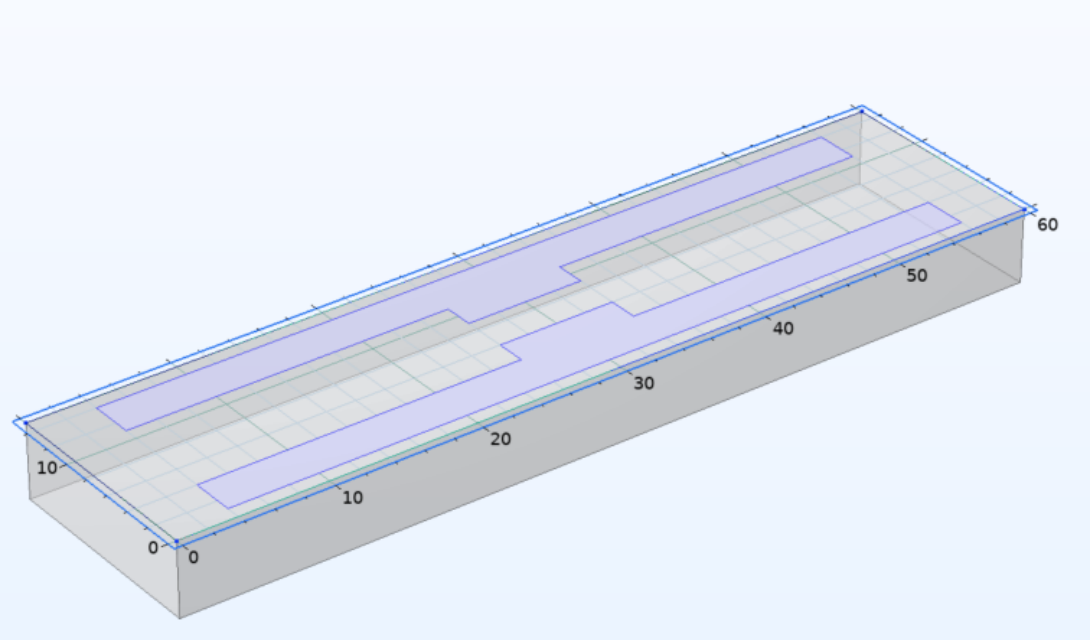

Figure 3.2: The example PCA in COMSOL.

The simulated steady-state electron concentration and hole concentration, and the transient electron concentration and hole concentration are shown in Figure 3.3. The steady-state figures show the electron concentration and hole concentration before the sudden femtosecond laser arrives at PCA gap, and the transient figures are the concentration when GaAs is excited by the laser pulse.

The simulated transient electric potential and electric field on the PCA surface are shown in Figure 3.4.

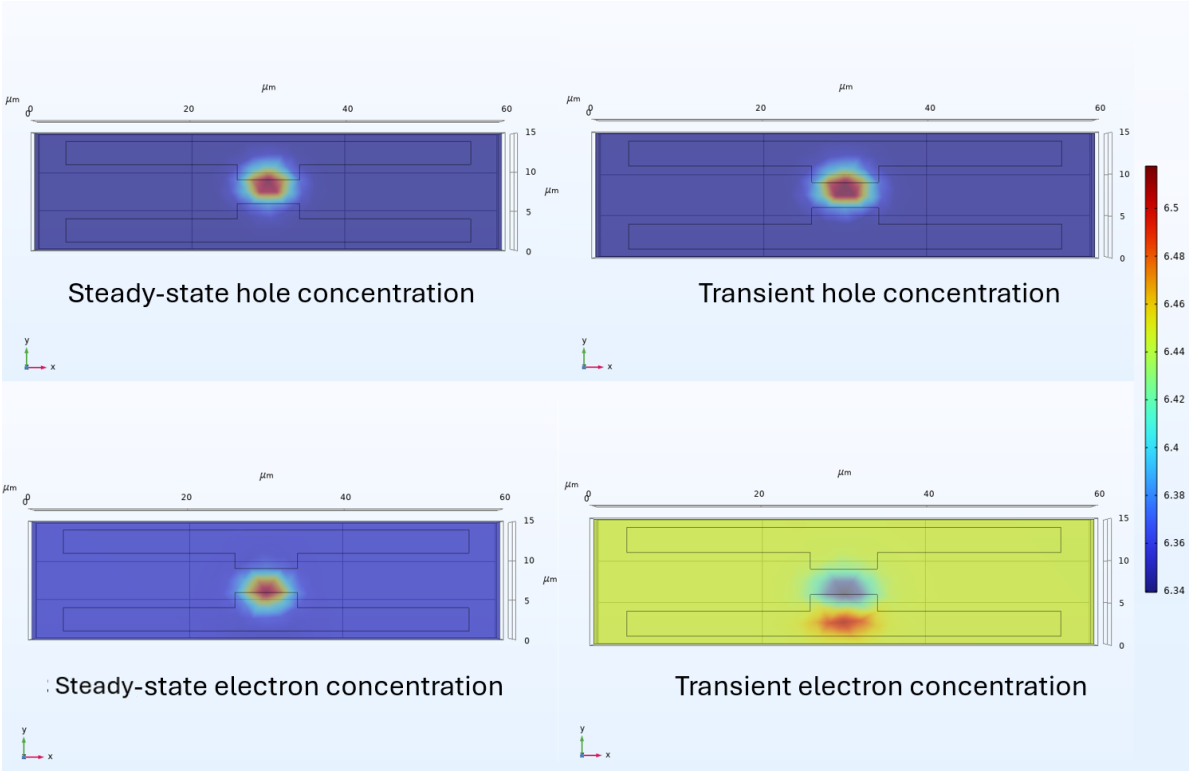

Figure 3.3: The simulated steady-state and transient electron concentration and hole concentration.

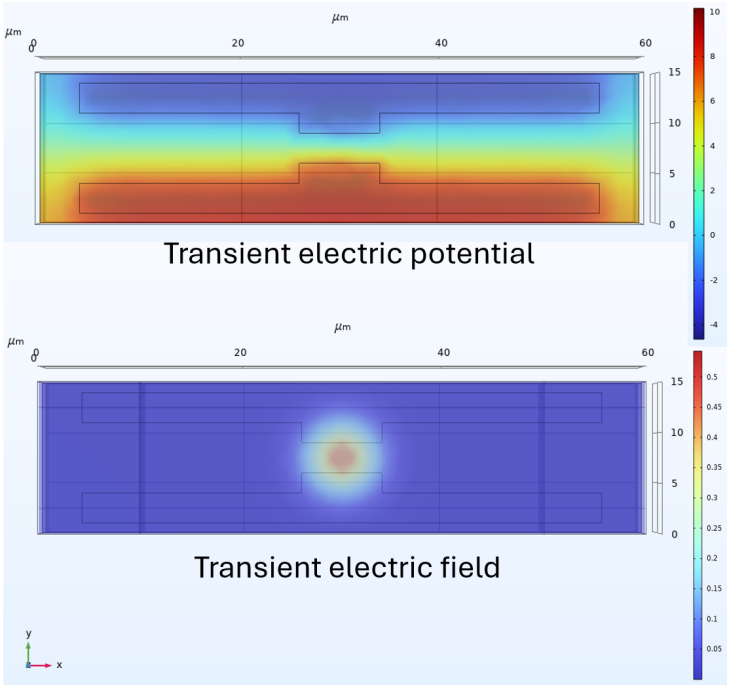

Figure 3.4: The simulated transient electric potential and electric field on the PCA surface.

It can be observed that a large amount of electron-hole pairs are excited with the laser pulse, resulting in the expected surface current between the two electrodes. At the PCA gap, a high concentration of electron-hole pairs are generated. Along with the potential from the positive electrode to the negative electrode, a surface current is generated. The surface current density is shown in Figure 3.5.

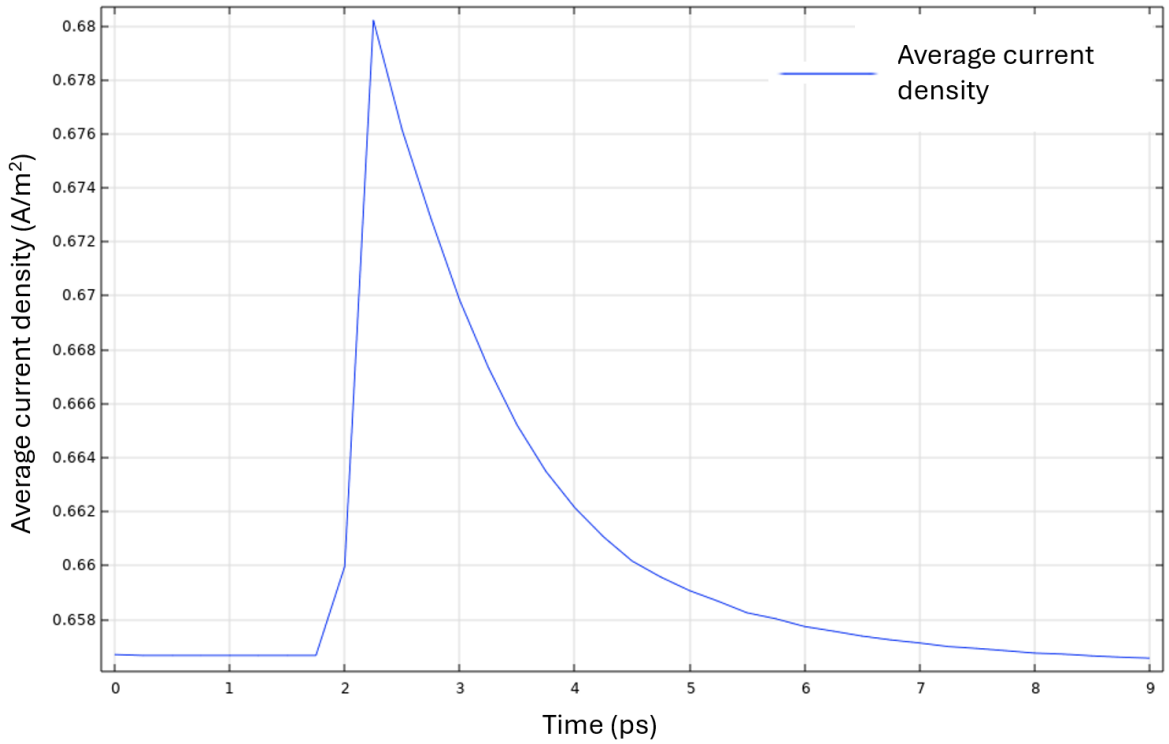

Figure 3.5: The simulated current density of the example PCA.

To verify the reliability of this simulation result, the reference PCA based on a 450 μm-thickness SI-GaAs has been fabricated in James Watt Nanofabrication Centre in University of Glasgow, and this reference PCA has been tested in Queen Mary University of London. Using a Tsunami Ti:Sapphire laser with $f_{rep} = 80MHz$ and 100 μm diameter laser beam, it has been measured that the surface current under 10 mW is 19.9 nA. This surface current has been tested with zero-bias. The reason for using a ≈100 μm laser is that this is the smallest size that the laser source equipped in this laboratory can achieve. In fact, the beam size of the laser source equipped in this lab is 1 mm. The beam is focused by a lens in the PCA measurement, and the theoretical value of the beam spot size after being focused by the lens is 100 μm. The accuracy is not guaranteed, therefore the actual beam spot size may be larger than the theoretical value.

Applying the simulated current density in Figure 3.5 on the same size laser spot, the calculated peak surface current is $I_s = 0.68A/m^2 * \pi r^2 = 0.68A/m^2 * 7.85 * 10^{-9} = 5.3nA$. Although there is a gap between the simulated data and the tested surface current, the two results are close to each other. This discrepancy between the measured surface current and simulation results can be attributed to the difference in laser beam spot sizes which is 100 μm in experiment and 5 μm in simulation, and the difference from the dimensions of the actual substrate and the simulated substrate. Given that the actual beam spot size can be larger than 100 μm, the calculated theoretical current data can be also larger than 5.3 nA, which better matches the measurement result. Considering other possible differences in optical power normalization, and uncertainties in material parameters, the error can be accepted. It can be regarded that the simulation result shows good agreement with the actual measurement.

Overall, it can be concluded that this COMSOL-CST cross-simulation method is not only convenient to create, but also save simulation time. Moreover, the same photocurrent results obtained from COMSOL can be widely applied to multiple CST simulations if the electrodes structure of PCA and the antenna gap remain the same. In addition, compared with directly using the default pulse of discrete port in CST, this simulation method provides a more realistic photocurrent, which can greatly improve the accuracy and reliability of PCA simulation. Therefore, this method is worthy of widely applied in related simulations and studies.

3.2 THz for Security Inspection

At present, the application of THz waves in the field of penetrating imaging for security inspection has attracted extensive attention from researchers. For example, T-5000 imaging developed by ThruVision Company uses 0.05 - 3 THz radiation to detect dangerous items such as bombs and weapons at a distance up to 25 m [181] [182]. In this PhD

research, a PCA is proposed following the objective to design a high-performance THz emitter that suitable for security inspection applications. Referring to [182], the target operational frequency range of the designed PCA is required to cover 0.1 - 3 THz and achieving optimal performance within the 1.5 - 2.5 THz frequency range. To meet this goal, a spiral THz PCA has been designed, simulated, and fabricated. In fabrication, GQD is deposited to PCA gap to investigate the influence on PCA surface current behaviour.

Figure 3.6: THz imaging for security inspection [182]

3.3 THz Spiral PCA Design

The THz spiral PCA consists of two Au electrodes and a SI-GaAs substrate. Based on research in Chapter 2, plasmonic contact nanofingers and Si hyper hemispherical lens have been employed to the PCA to enhance the radiation performance. The geometry of the spiral electrodes is designed by equations:

$$X(t) = atcos(t) \tag{3.1}$$

$$Y(t) = atsin(t) \tag{3.2}$$

in which $t = 0\tilde{}8\pi, a = \pi$. The maximum t is 8π, which means this spiral PCA has four complete circular turns. The PCA gap G is labelled in Figure 3.7. According to the requirements of THz imaging for security inspection, the target frequency is drawn up as $\approx$ 2 THz [181]. The estimated wavelength is calculated by $f = \frac{c}{\lambda}$. The frequency range and the outer circumference of PCA with circular shape is studied in [183], in which the wavelength and the diameter of the outer circumference of the PCA is computed as:

$$D = n\lambda, n = 1.1\tilde{}3.5 \tag{3.3}$$

The wavelength could be defined with the help of D, which is the diameter of the outer circumference. The ratio of the arm-gap G_a between each electrode and arm-width W_a of each electrode is tested in several simulations. According to comprehensive comparisons, the ratio of 3:1 is the most reasonable design. The relationship between W_a and D can be defined as:

$$D = 2 * (\pi * 8\pi * cos 8\pi + \frac{W_a}{2}) \tag{3.4}$$

Based on these studies, the diameter of PCA outer circumference D has been designed to be 160.64 μm, which gives a maximum 146 μm wavelength, and the peak performance is calculated at $\approx$ 2.05 - 2.24 THz. The dimensions of the electrodes and substrate of the proposed spiral PCA are summarized in Table 3.1. In Figure 3.7, the corresponding structural dimensions are indicated except T_a and T_s, which are the thickness of PCA electrodes and substrate, respectively.

Table 3.1: Corresponding values of spiral PCA electrodes and substrate

Dimensions	W_s&L_s	D	G	G_a	W_a	T_a	T_s
Length (μm)	250	160.64	5	7.15	2.72	0.2	10

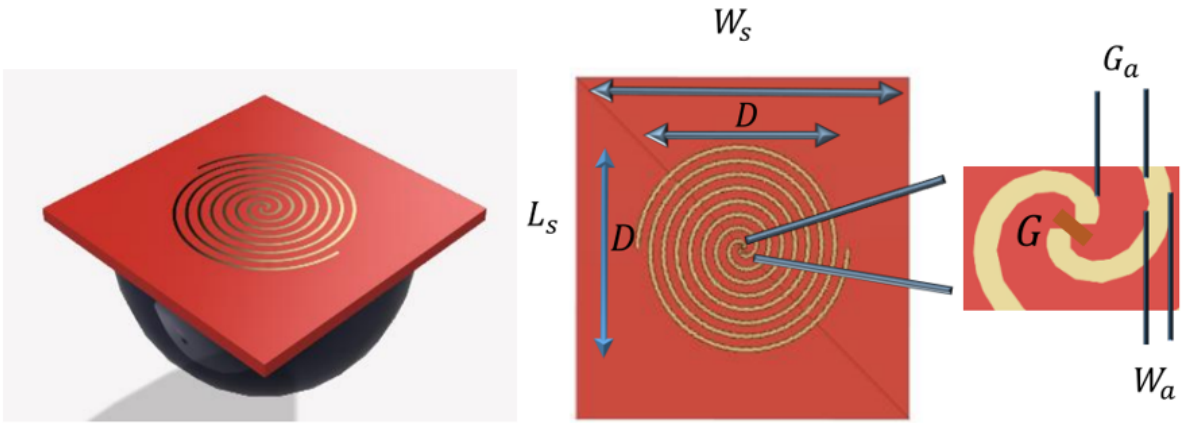

Figure 3.7: The proposed THz spiral PCA made of two gold electrodes on a SI-GaAs substrate and a silicon hyper hemispherical lens.

The dimensions of the Si hyper hemispherical lens are shown in Table 3.2, where T_c is the height of the cylinder part of hyper hemispherical lens, and R_c and R_l are the common radius of Si cylinder part and hemispherical part. The design of the lens follows Equation 2.13, which is introduced in Chapter 2.

Table 3.2: Corresponding values of the Si hyper hemispherical lens

Dimensions	T_c	R_c	R_l
Length (μm)	26.25	125	125

Regarding to the contact nanofingers, the geometric structure is designed as a trapezoidal shape with a top width of 50 nm, a bottom width of 100 nm, and a length of 150 nm. The height of each nanofinger is 50 nm. These nano-fingers are evenly arranged and are connected to the electrode edges within the PCA gap.

3.4 Simulation Results

In order to assess the performance of the THz spiral PCA, the reference PCA from research of [180] mentioned in the previous section has also been simulated in CST as a comparison. Both PCA simulation follows the COMSOL-CST cross-simulation method that proposed in this PhD study. Instead of measuring S11 parameter, the simulation of PCA detects the radiated power. In contrast to conventional THz patch antennas that uses S_{11} parameter to evaluate, the performance of a PCA is determined by its radiated power and directivity. Therefore, it is essential to compare the radiation power spectrum and radiation pattern.

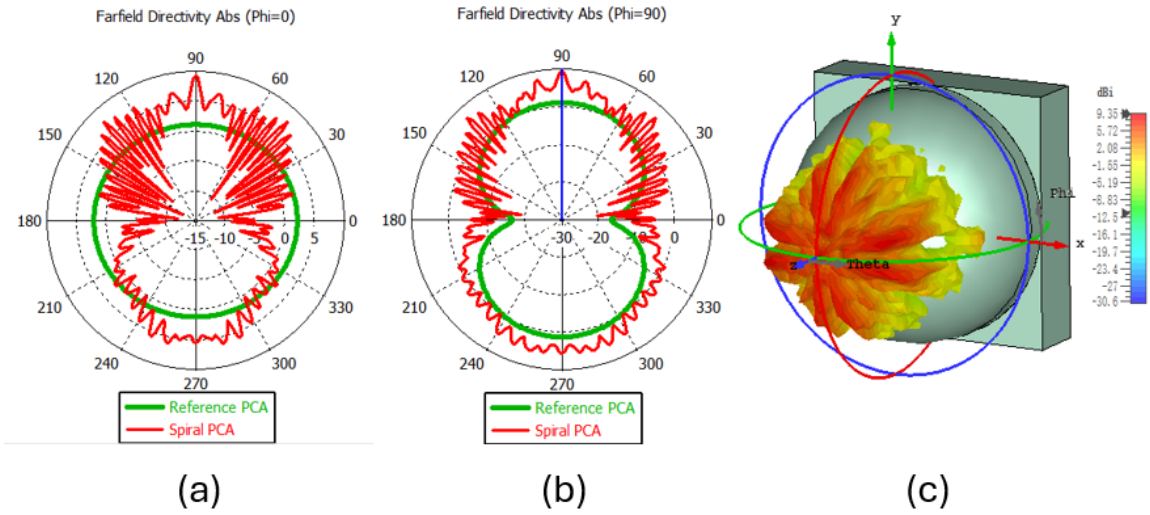

Figure 3.8: The radiation pattern of the THz spiral PCA compared to the reference PCA on (a) E plane and (b) H plane; (c) The 3D farfield radiation pattern of the THz spiral PCA.

Figure 3.8 shows the 1D directivity and 3D radiation pattern, as well as the comparison to the reference PCA. The broadband average directivity of the spiral PCA is 9.35 dBi on both E and H plane, while the peak directivity of 17.6 dBi shows at 2.9 THz. By contrast, the directivity of the reference PCA is 2.04 and 1.08 dBi on E and H plane. The angular width (3 dB) of the spiral PCA is 4.8°, while the front-to-back ratio is 21.1 dB and the side lobe level is -16.5 dB. By comparison, the proposed spiral PCA has higher directivity and gain.

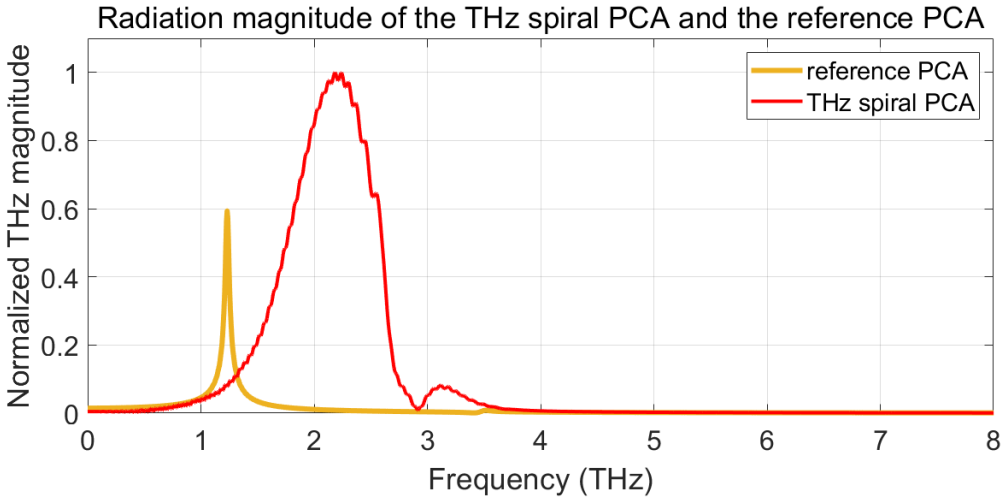

Figure 3.9: Comparison of the radiated E-field magnitude of the THz spiral PCA and the reference PCA.

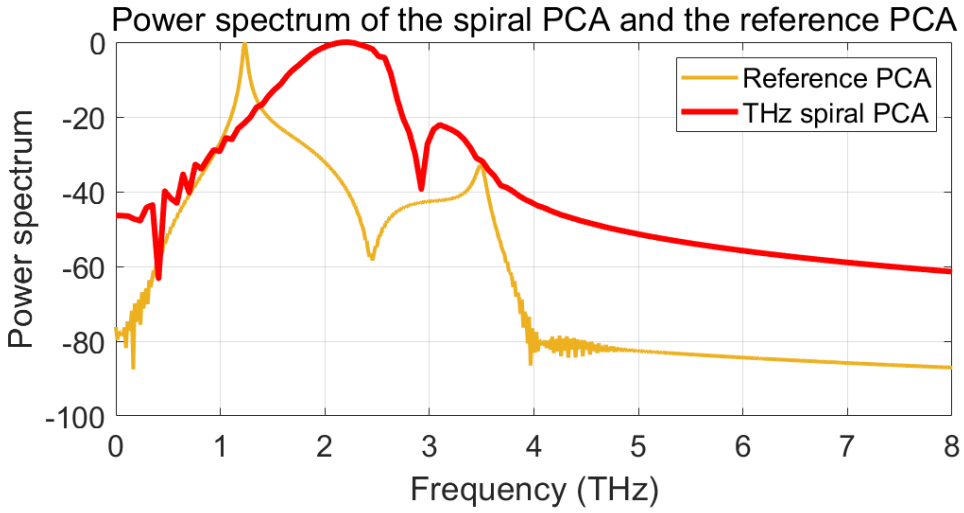

Figure 3.10: Comparison of the power spectrum of the THz spiral PCA and the reference PCA.

Figure 3.9 and Figure 3.10 illustrate the radiated E-field magnitude comparison and the power spectrum comparison between the proposed THz spiral PCA and the reference PCA in [180]. From these figures, it can be observed that the proposed THz spiral PCA emits THz radiation that can cover the frequency range of 1 - 2.9 and 3 - 3.5 THz. Among them, the peak radiation falls within the range of 2 - 2.4 THz, which is in perfect agreement with the result obtained from the previous section. Furthermore, when using the standard that the best operational bandwidth is -3 dB from the peak value, this spiral PCA exhibits excellent performance within the frequency range of 1.5 - 2.6 THz. This result complies with the requirements for the required frequency mentioned earlier in this chapter for THz imaging. This indicates that the proposed THz spiral antenna has good performance and can be adapted to future THz imaging technologies.

Furthermore, a detailed farfield performance comparisons among the proposed spiral PCA and other published PCAs are provided in Table 3.3. It can be concluded that the proposed THz spiral PCA has good performance and is a promising THz emission source for future THz imaging applications.

Table 3.3: Values of radiation performance of the proposed THz spiral PCA compared to other published PCA designs

PCA design	Substrate	Bandwidth (THz)	Directivity (dBi)	3dB Angular width (deg)	Side lobe level (dB)
Proposed spiral PCA	SI-GaAs	1.1	17.6	4.8	-16.5
Ref [179]	Graphene-GaAs	0.7	13.74	45.9	-2.5
Ref [88]	LT-GaAs	0.181	13.3	N/A	-11.2
Ref [184]	LT-GaAs	7.93	7.7 - 11	N/A	N/A
Ref [185]	Quartz	3	18.2	N/A	N/A

3.5 Fabrication of the GQD-Based THz Spiral PCA

The proposed THz spiral PCA has been fabricated in James Watt Nanofabrication Centre (JWNC) in University of Glasgow. E-beam lithography and metal deposition-liftoff methods are used to finalize the fabrication. The process of E-beam lithography, metalisation and liftoff, and the deposition of GQD are introduced in this section. Different from the simulations, the PCA requires two biasing pads for applying voltage, thus two metal pads will be added to both sides of PCA in the fabrication, so as to connect the bias voltage through the conductive gel and wires to the electrodes.

3.5.1 E-beam Lithography

The general fabrication process can be summarized into six parts: cleaning, spinning E-beam resist, E-beam exposure, development, metallisation, and liftoff. Figure 3.11 illustrates the general procedure of a complete E-beam fabrication.

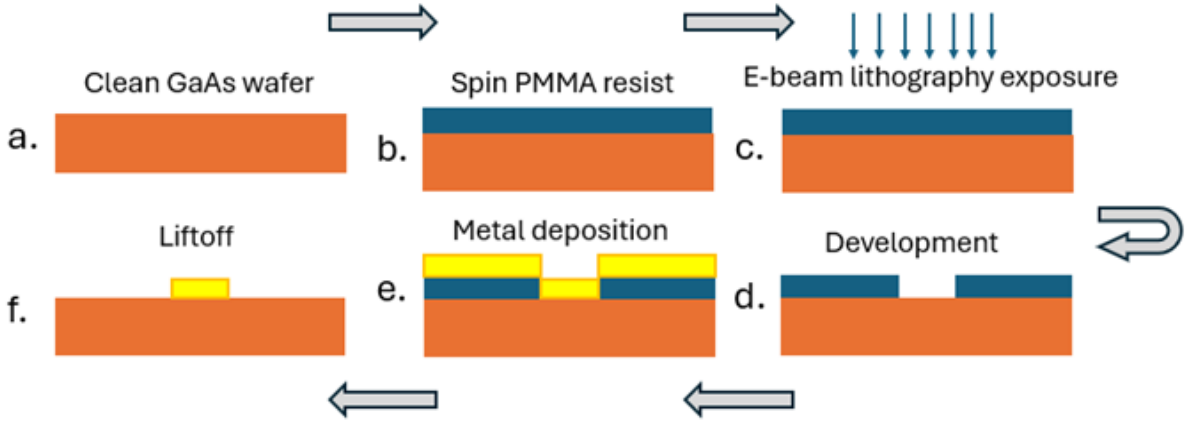

Figure 3.11: General fabrication procedure of E-beam lithography

In JWNC, GaAs samples are cleaned using an ultrasonic bath. The cleaning was carried out sequentially in methanol, acetone, and isopropanol (IPA) solutions, with each ultrasonic bath lasting five minutes. After the cleaning process, the samples were dried and prepared for the subsequent E-beam resist spinning.

3.5.2 Setting PMMA Resist

PMMA has been used as the E-beam resist in the fabrication. Theoretically, the PMMA thickness should be at least three times the target electrode thickness to ensure a successful metal deposition and liftoff. The relationship among the thickness of PMMA resist, spin speed, and PMMA dilution are described as follows:

$$Thickness \propto Dilution^2 / \sqrt{SpinSpeed} \tag{3.5}$$

The total thickness of PMMA layers should be at least three times thicker than the target metal layers. As the PCA electrodes have a thickness of 200 nm, two types of PMMA are selected in this fabrication process, which are 200k-12% PMMA solution in anisole (780 nm) and 950k-2% PMMA solution in ethyl lactate (70 nm), providing a total thickness of 850 nm. The required spinning speed of the selected PMMA solutions are 4000 rpm. Samples with PMMA need dehydration bake at 180 $°C$ for over 30 minutes, or a hotplate with the same temperature can complete the dehydration within 5 minutes.

3.5.3 E-beam Lithography Exposure

The E-beam exposure is operated on a Raith EBPG5200 HS tool. After submitting the edited *.GDS* pattern, the job has to be created using a fracturing Beamer and uploaded to *cjob* where the exposure beams and doses can be settled. The operating beam current I_e of EBPG starts from 1 nA to 180 nA, while the minimum beam spot size at 1 nA can reach 4 nm. The dosage of E-beam is defined from I_e and the beam movement frequency f at which the beam travels between beam spot size grid sites, shown as follows:

$$dose = \frac{I_e}{f^2} \tag{3.6}$$

From this, we know that the lower the beam movement frequency, the longer the staying time at one specific spot, and therefore comes with a higher dosage. Thus, to save operation time, the gap design at PCA centre and the contact fingers should be arranged a small I_e and a small beam spot size, while the biasing pads can be patterned using higher I_e and larger beam spot size.

3.5.4 Sample Development

The exposure process only forms the pattern on the resist, but does not convert them into patterns that can be used for subsequent processes. Development is necessary because it can transform the exposed PMMA into a protective layer with a specific pattern, enabling subsequent etching, deposition, and other steps to precisely form the required electrodes on the substrate with high tip sharpness. The exposed sample needs to be stirred in methyl isobutyl ketone (MIBK) and IPA for 20 seconds each, until the red and green shadows on the pattern edges cannot be seen under microscope. All development needs to be performed at a fixed temperature of 23 $°C$.

3.5.5 Metallisation and Lift-off

The 5/195 nm Ti/Au metal deposition is achieved by Plassy IV and Evap 7 tool. Plassy IV and Evap 7 are two types of machines that can deposit thin metallic films onto substrates under high-vacuum conditions. The thin Ti layer between gold and substrate can improve the attachment of the electrodes. Meanwhile, the deposition of the nanofingers is composed of 5/45 nm Ti/Au bi-layer structure. Because the thickness of electrodes and nanofingers are different, two metallisation processes needs to be carried out separately. To ensure accurate alignment between the two metallisation steps, alignment markers have been incorporated into the cjob design, allowing the E-beam system to precisely register and

pattern subsequent layers at the same coordinates. Given the extremely small feature size, scanning electron microscopy (SEM) has been employed after fabrication to inspect the PCA gap region and verify the precision of the nanofinger fabrication. In metal deposition process, metal atoms will be released from the plassy gun, and will be deposited on the substrate at a speed of less than one nanometres per second (for example, Au deposition speed is ≈ 0.5 nm/s). The metal deposition relies on proper development because an over-developed PMMA resist layer will cause a camber angle on PMMA edge, thus there will be PMMA that 'hide' under the electrodes and cannot be lifted off. Figure 3.12 compares the successful and unsuccessful metallisation and lift-off on a proper developed sample and an over-developed sample.

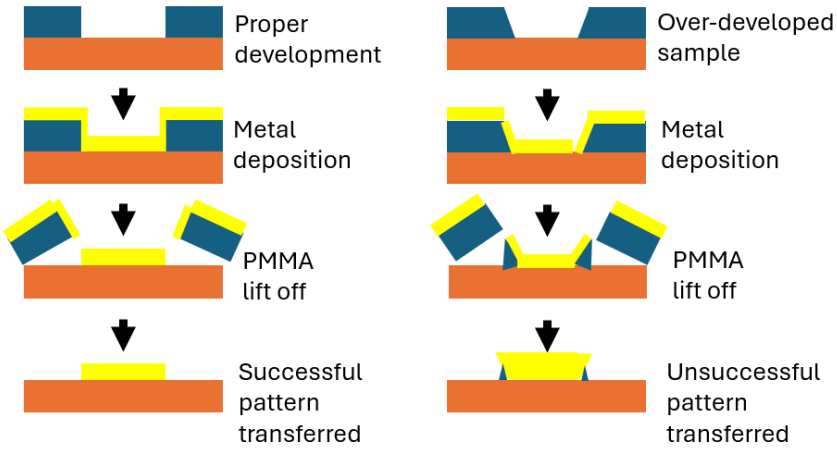

Figure 3.12: Comparison of successful metallisation and unsuccessful metallisation. Over-developing the sample may cause a camber angle on the PMMA edge, which leads to an inverted trapezoidal metal shape, and can prevent PMMA from being completely lifted off.

After the metal deposition, lift-off will be proceed in acetone solution at a temperature of 50 $°C$ for hours. The acetone will solve PMMA and remove the metal on PMMA, thus only the metal deposited within the pattern will be left on the substrate.

3.5.6 Deposition of GQD

The GQD utilized in this PhD study is provided by CD Bioparticles Company. The diameter of each GQD is less than 6 nm. The GQD product is stored in a solution mixed by water and ethylene glycol. During the fabrication, it is necessary to ensure that the PCA surface is clean and free of dust. Therefore, the UltraViolet Ozone Cleaner System (UVOCS) is required to clean the PCA surface and remove potential contamination and increase the adhension. The UVOCS tool utilized in the PCA fabrication is T10*10 OES device in JWNC. Then, the solution containing GQD is dropped onto the antenna surface. The antenna is spun at a low speed (500 rpm) to make the GQD distribution as uniform as possible. Finally, the spiral PCA is placed in a low-temperature oven to evaporate the liquid. The liquid needs to be completely evaporated until the PCA surface is dry, then the GQD is successfully deposited on the PCA surface. Figure 3.13 illustrates the full fabrication progress of the GQD-based THz spiral PCA.

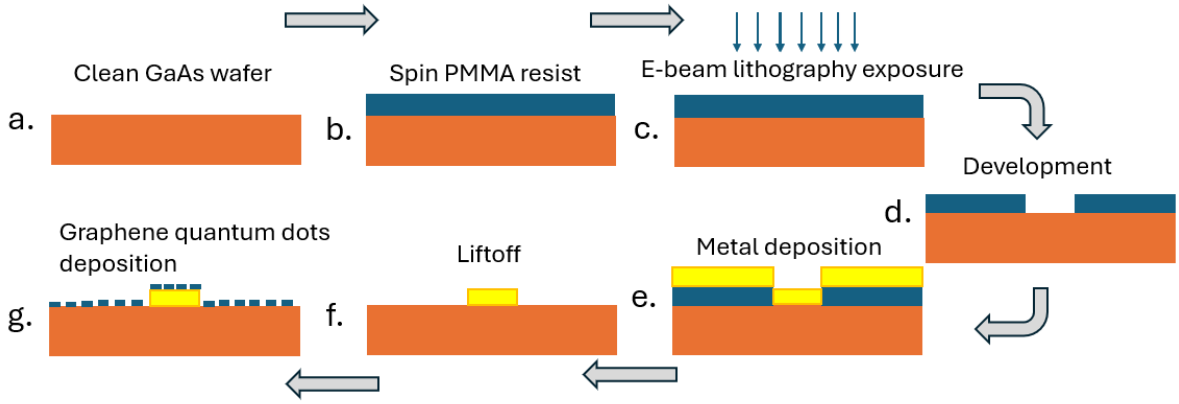

Figure 3.13: Deposition of GQD in PCA fabrication.

The deposition process of GQD is after the electrodes metallisation and liftoff. Obviously, there are GQDs that deposited onto the electrode. However, only GQDs that deposited at the antenna gap will be excited, and the measurement of the surface current is conducted within the antenna gap. Therefore, GQDs that are outside the aiming position will not affect the experimental results.

3.5.7 Connecting bias to spiral PCA using silver conductive gel

To apply bias voltage to the PCA, two biasing pads have been added to both electrodes in the fabrication. Normally, soldering and wire-bonding can be used to attach conductive wires to the biasing pads. However, soldering might be harmful to the electrodes, and wire-bonding has certain limitations due to the fact that it requires an extremely clean environment and an extremely flat surface. Also, the operation is complicated. Therefore, we choose to use the easiest way to attach wires to the biasing pads, which is using conductive gel. The gel used in this PhD study is RS PRO Silver Conductive Lacquer. Figure 3.14 is a picture of connecting the wires to the pads using silver conductive gel. The gel must be dehydrated for a few hours till it becomes solid. During the measurement, the wires are connected to voltage source using a BNC cable thus providing bias voltage to the electrodes.

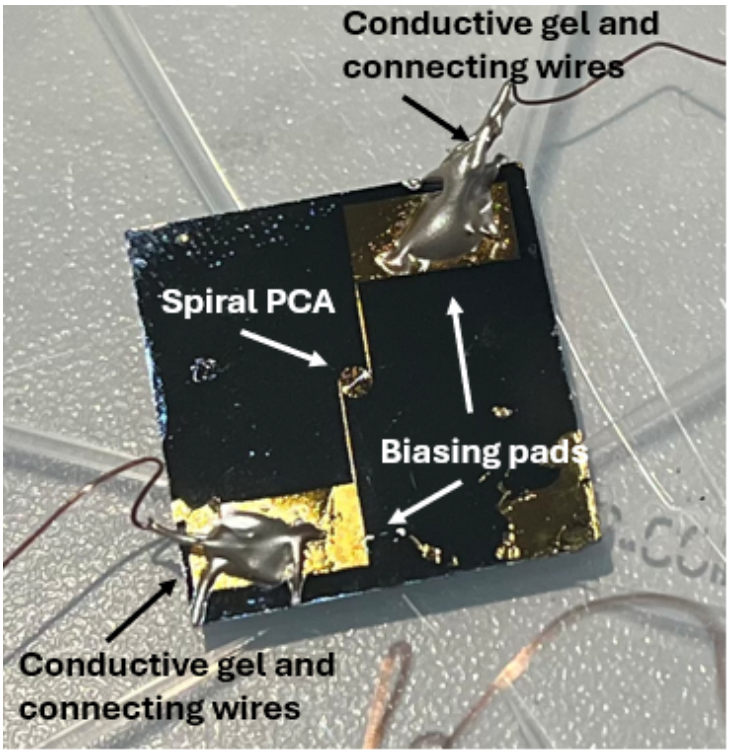

Figure 3.14: Connecting wires to the biasing pads using silver conductive gel.

3.6 Spiral PCA Measurement

3.6.1 Raman Spectroscopy and SEM of the GQD-Based THz Spiral PCA

In this PhD study, Raman Spectroscopy is used to verify the deposition of GQD. SEM is used to examine the fabrication accuracy of the plasmonic contact nanofingers within the PCA gap. It should be noted that in this PhD research, the utilized GQD is small (diameter less than 6 nm), thus they cannot be observed using SEM. In this case, the TEM needs to be used. Since the laboratory conducting the spiral PCA fabrication is not equipped with TEM, and Raman spectroscopy is also capable of verifying GQD deposition, the TEM is not used in this study.

The Raman spectroscopy instrument for the experiment is LabRAM HR from HORIBA company with a Ventus 532 laser system (100 mW, 532 nm). Figure 3.15 is a photo of the Raman spectroscopy instrument in the chemistry lab of the University of Glasgow. For the experimental set-up, a 10 mW laser power has been operated on the range from 50 to 1000 cm^{-1} for a integration time of 10 seconds.

Figure 3.16 presents the Raman spectrum acquired from the PCA gap of the GQD-based THz spiral PCA. The standard Raman shift peaks of GQD are at 1349 and 1593 cm^{-1}, respectively [186]. The D band at $\approx$ 1375 cm^{-1} and the G band at $\approx$ 1593 cm^{-1} indicate that the GQD has been deposited to the PCA surface successfully. The extra peak at around 1615 cm^{-1} can be attributed to lattice disorder of the GQD product, or impurities that contains in the GQD solution and deposited onto the PCA surface together with GQD. A minor peak at x$\approx$1520 is observed and can be attributed to contamination on the PCA surface. It should be noticed that in order to test the surface current of THz spiral PCA before and after depositing GQD, the PCA has been exposed in the air and

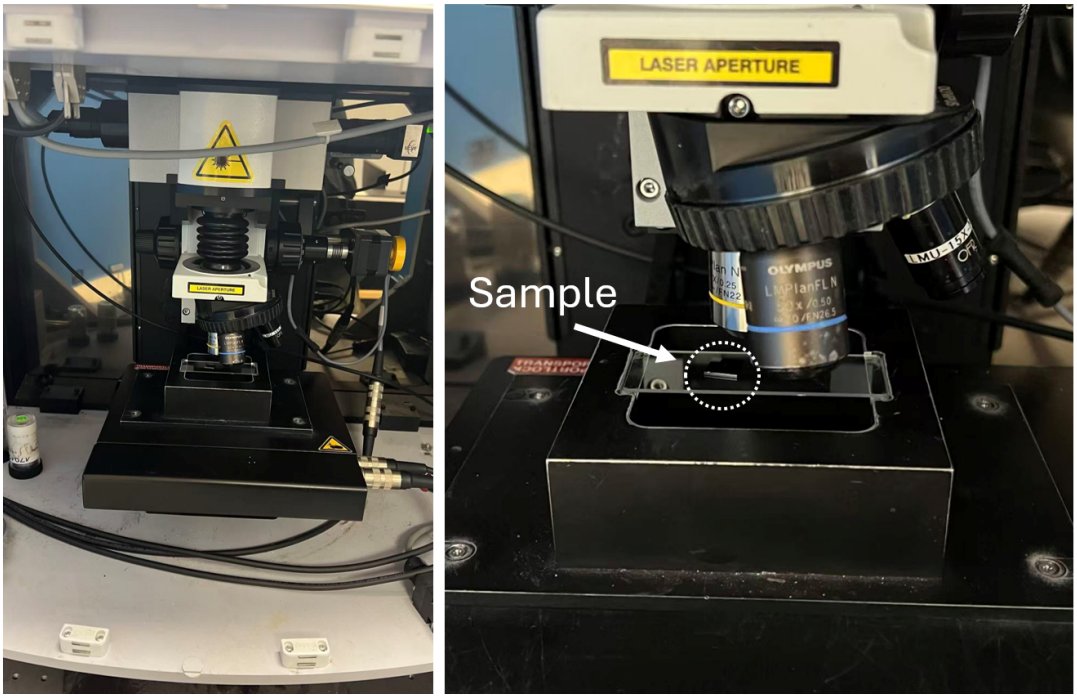

Figure 3.15: A photo of the Raman spectroscopy instrument in the University of Glasgow.

inevitably touched by hands. The deposition of GQD is completed on the same PCA sample after the first surface current measurement, thus there could be contamination remains on the surface even after UVOCS, such as organic residues from human hands. Therefore, this minor peak is regarded as noise.

The Raman spectroscopy figure clearly shows the matched D and G band, indicating the successful deposition of GQD.

The SEM facilities in JWNC are SU8230 and SU8240 tools provided by Hitachi. A photo of the SU8240 instrument is shown in Figure 3.17.

The SEM image of the fabricated spiral PCA in Figure 3.18 clearly shows the well-defined spiral electrode structure with the precisely patterned nano-fingers embedded within the gap. A zoomed figure of the contact nanofingers is shown in Figure 3.19. The SEM figures confirm that the spiral geometry and the contact fingers have been successfully fabricated.

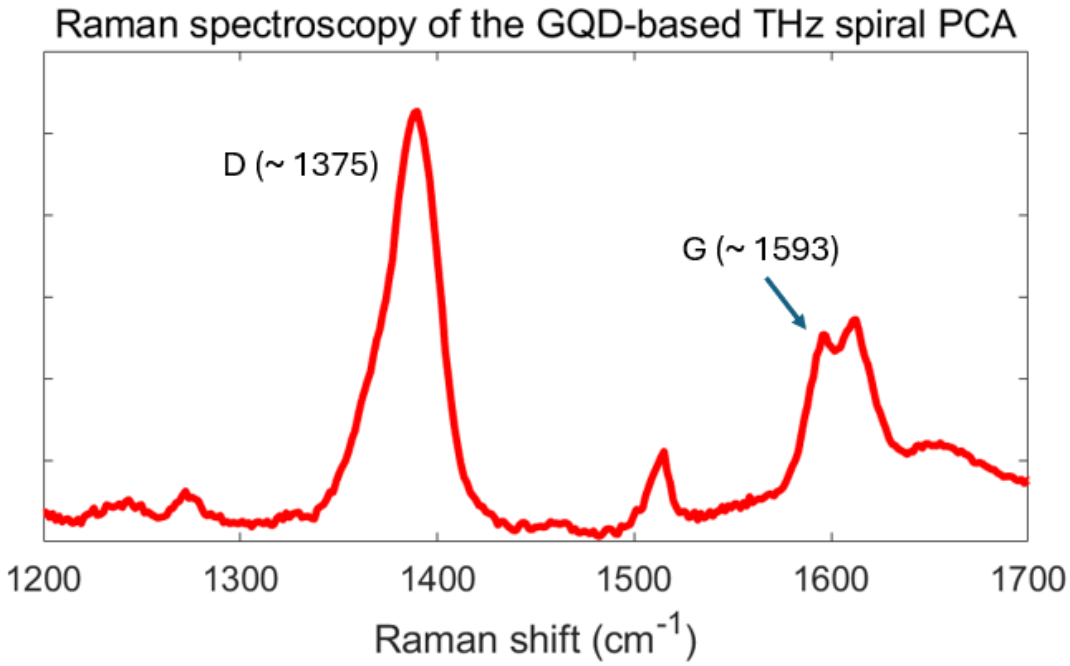

Figure 3.16: The Raman spectroscopy of the GQD-based THz spiral PCA. The peaks at x≈1375 and x≈1593 indicate that GQD is successfully transferred to the PCA surface. The peak at x≈1615 can be the lattice disorder. A weak peak at x≈1520 could be attributed to contamination and is regarded as noise.

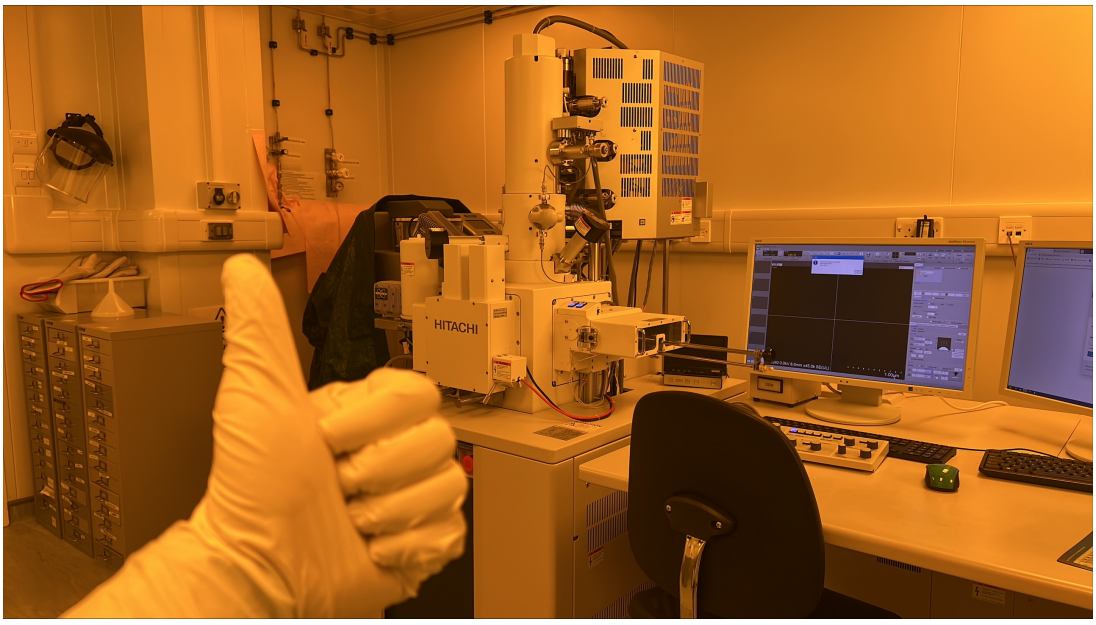

Figure 3.17: A photo of the SEM-SU8240 in JWNC.

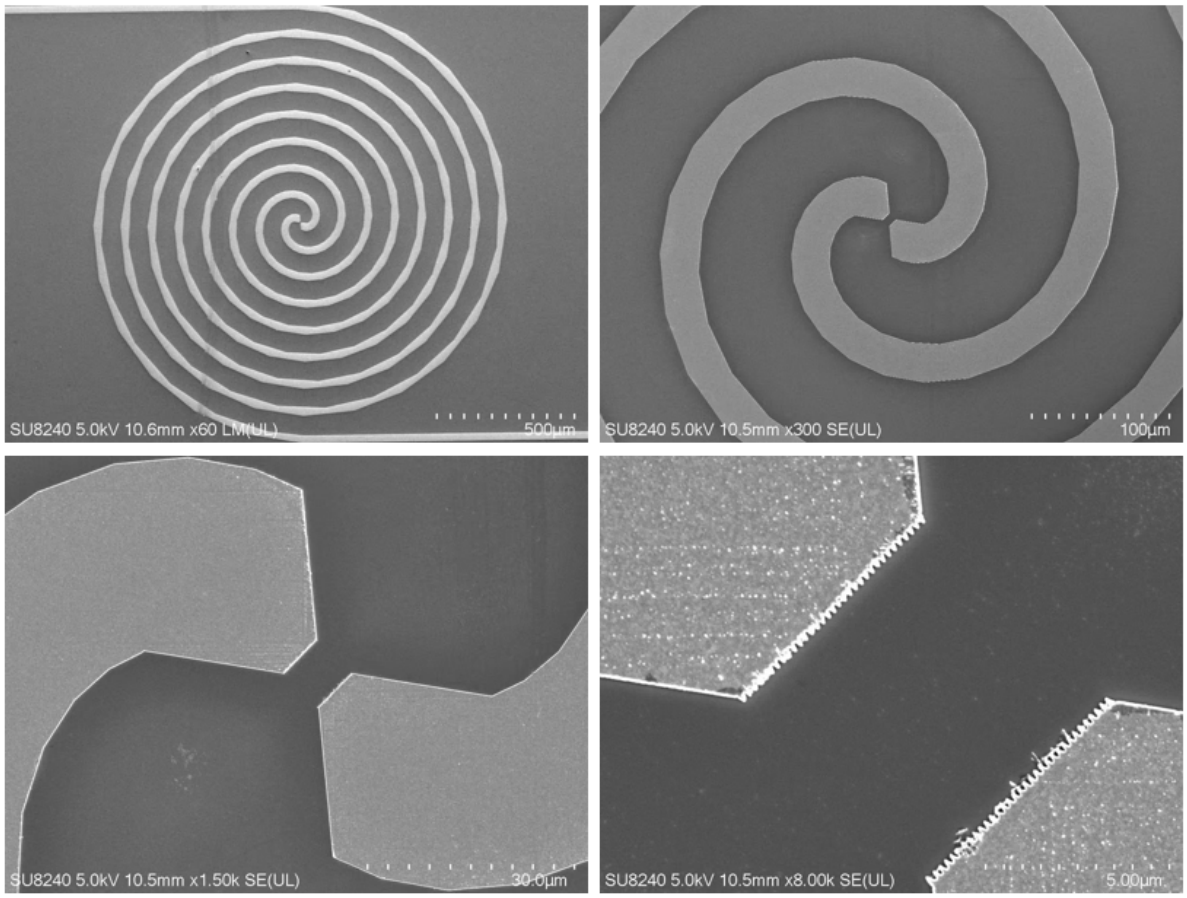

Figure 3.18: The fabricated THz spiral PCA under SEM. The contact nanofingers are successfully fabricated within PCA gap. The two lines extending out from the electrodes are used for connection with the biasing pads.

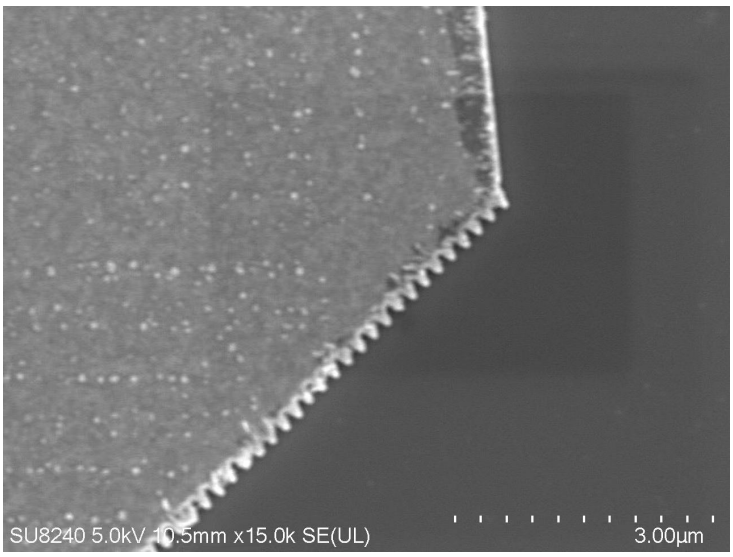

Figure 3.19: The zoomed SEM image of the fabricated plasmonic contact nanofingers within the gap of the THz spiral PCA.

Based on the Raman spectroscopy and SEM images, it can be concluded that the fabrication of the proposed THz spiral PCA is successful. Therefore, the experimental results from the subsequent PCA measurements is reliable and convincing.

3.6.2 Surface Current Measurement

The measurement of the GQD-based THz spiral PCA has been proceeded in Quen Mary University of London. The THz-TDS system in the THz lab of QMUL uses Tsunami oscillator laser, with a beam spot size of $\approx$ 100 μm and f_{rep} of 80 MHz. The laser power range is up to 250 mW. For PCAs with 5 μm gap, considering that high fluence could cause damage to the PCA electrodes and GQD, the laser power used in the experiments is limited to 20 mW. The device that used to detect the surface current is Keithley-2450 provided by Farnell Company, shown in Figure 3.20. During the measurement, bias voltage is applied by a DC voltage source, while the Keithley device records the surface current between electrodes, from which the recorded data can be extracted after the measurement is completed.

Figure 3.20: A picture of the Keithley-2450 source measurement unit. The surface current of the fabricated GQD-based THz spiral PCA is detected by such device.

The surface current data of the GQD-based spiral PCA is shown in Figure 3.21, using an excitation optical power from 5 mW to 20 mW.

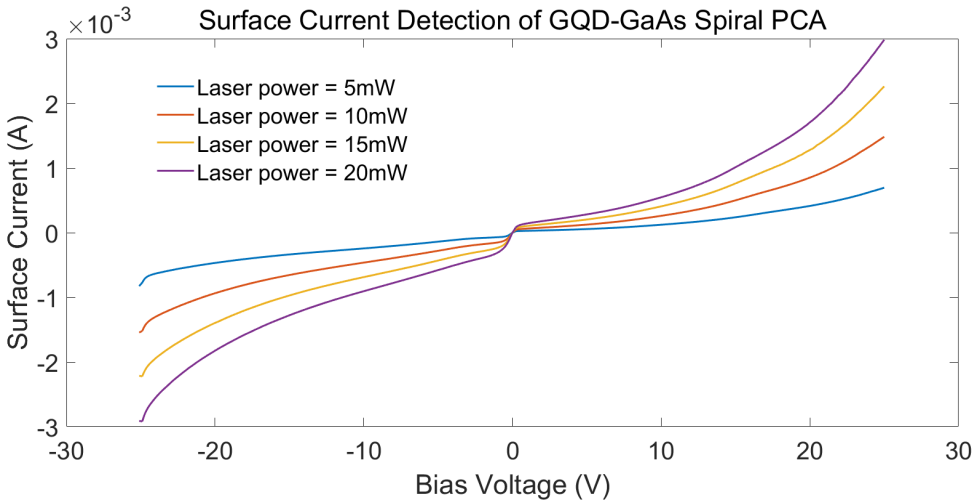

Figure 3.21: Surface Current Detection of GQD-Based Spiral PCA with laser power of 5, 10, 15, and 20mW.

Figure 3.22, 3.23, 3.24 and 3.25 show the comparison of the measured surface current of the THz spiral PCA before and after deposition of GQD. It can be easily observed that, under the same laser power conditions, if the bias voltage is low, the surface current of GQD-based spiral PCA is lower than that of non-GQD spiral PCA. However, as the bias voltage increases, the surface current of the GQD-based spiral PCA gradually exhibits a stronger increasing rate, eventually exceeding the non-GQD PCA. From the figures, it can be concluded that with higher the bias voltage, it comes to higher increasing effect in surface current. The reason of this phenomenon can be the resistance changing of GQD as the temperature rises, because the increasing bias voltage does lead to higher temperature on the PCA surface, as well as the Fermi level of GQD reaches a high level and the carrier losses will be reduced. This situation shows agreement to the study of GQD in Chapter 2. It should be noted that the two surface current measurements have been conducted on the same spiral PCA sample, one measurement is conducted before GQD deposition, and the other is carried out after depositing GQD. Therefore, it can be concluded that GQD is the main reason of the difference in surface current.

The experimental results of this section show that GQD can enhance the surface current of PCA, and as the laser power and bias voltage increase, the enhancement effect of GQD on the PCA surface current also increases. The finding that GQD can enhance the surface current is consistent with the conclusion drawn in Chapter 2 that GQD can

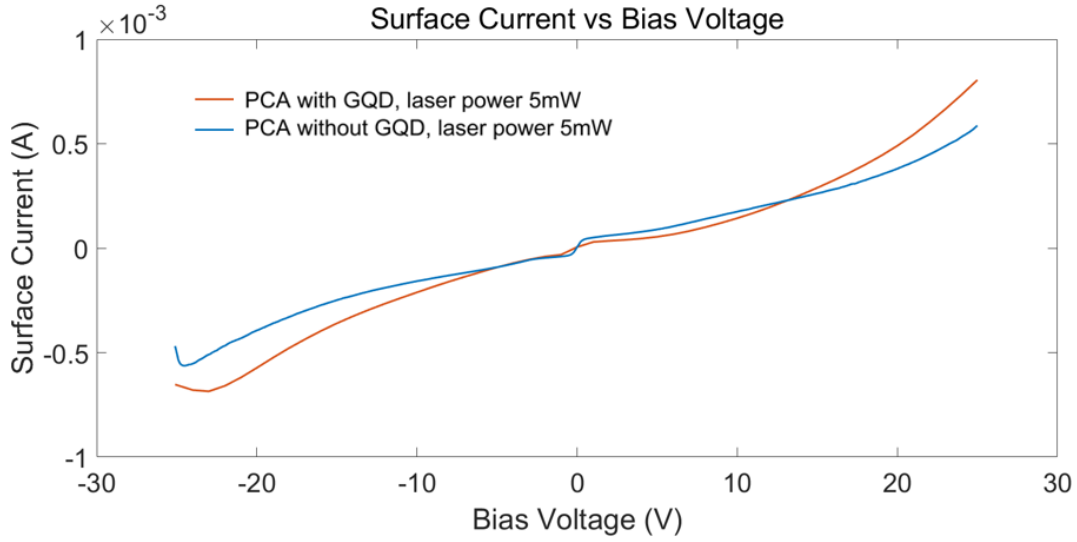

Figure 3.22: Surface current comparison of the THz spiral PCA before and after GQD deposition. The laser power is 5 mW. The red line is the GQD-based PCA, while the blue line is the non-GQD PCA.

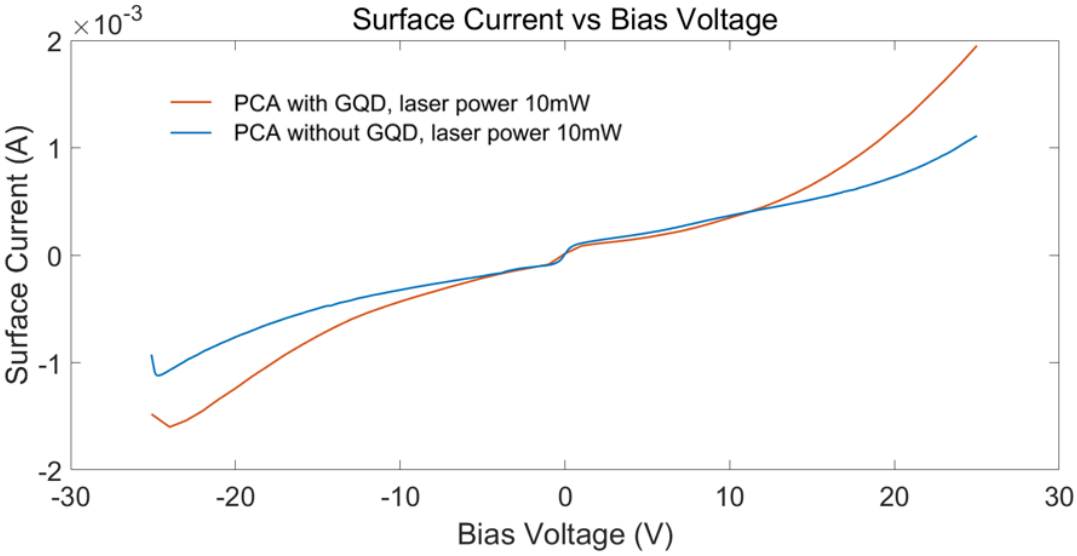

Figure 3.23: Surface current comparison of the THz spiral PCA before and after GQD deposition. The laser power is 10 mW. The red line is the GQD-based PCA, while the blue line is the non-GQD PCA.

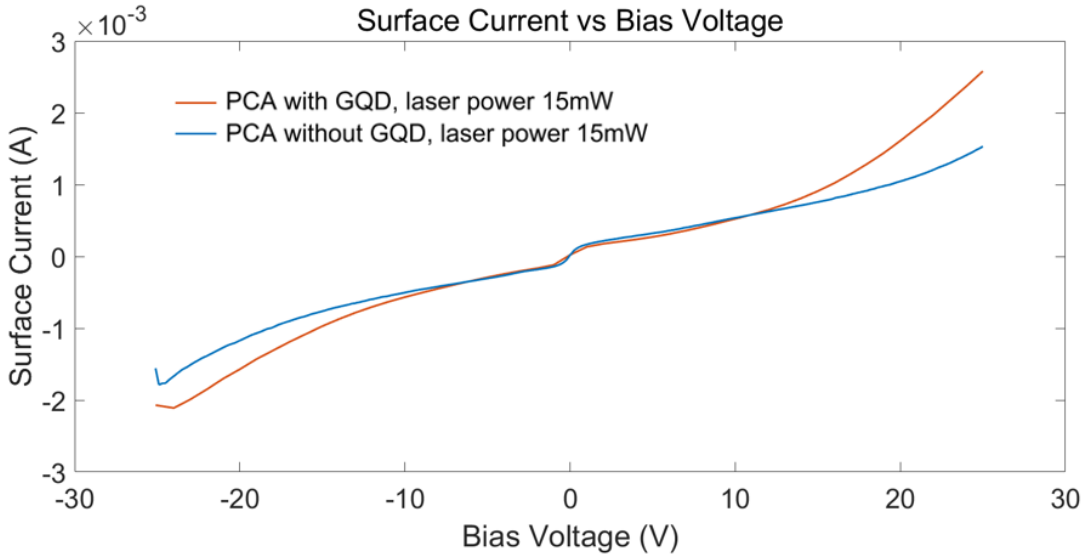

Figure 3.24: Surface current comparison of the THz spiral PCA before and after GQD deposition. The laser power is 15 mW. The red line is the GQD-based PCA, while the blue line is the non-GQD PCA.

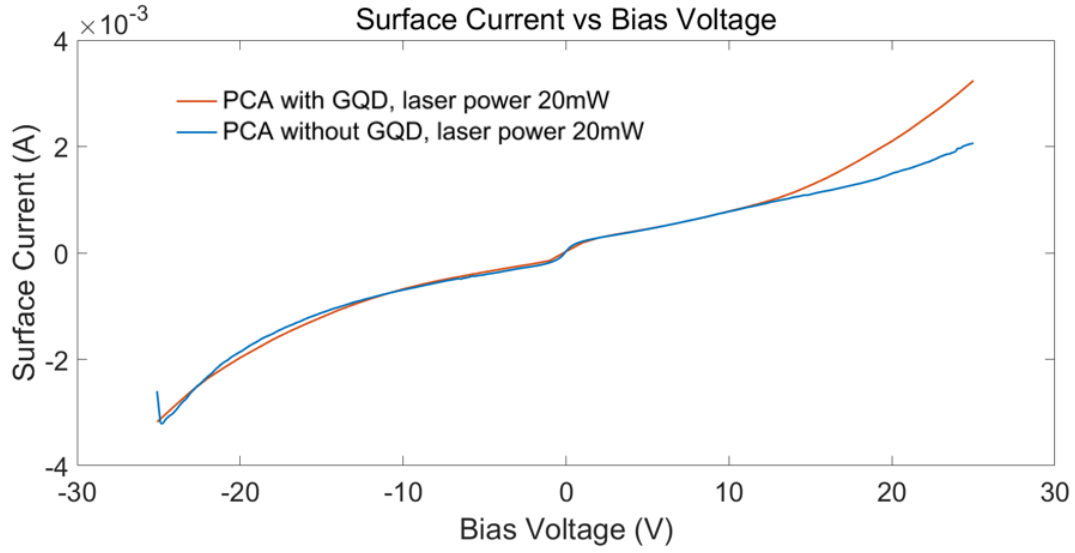

Figure 3.25: Surface current comparison of the THz spiral PCA before and after GQD deposition. The laser power is 20 mW. The red line is the GQD-based PCA, while the blue line is the non-GQD PCA.

increase carrier density. This experiment has made contributions to GQD-based THz PCAs and other related THz technologies. The experimental result in this chapter also provides key information for other researchers, and can serve as a reference in the future research field of GQD. Additionally, since the results reveal that GQD exhibits higher carrier density enhancement under increased bias voltage and laser power, it is believed that GQD is particularly well suited for integration into large-area PCAs. As discussed in the literature review in Chapter 2, higher excitation power and bias voltage can be utilized to large-area PCAs, which can also maximize the benefits from GQD thus further enhance the THz emission.

However, due to the fact that the laser beam spot size used in the experiments does not match the PCA gap size, the THz radiation measurement has not yet been completed. This measurement will be completed in the future. As for the experimental plan, either a 5um-sized laser beam should be conducted in the measurement, or a PCA mount needs to be made, with a shelding lid on the front side. There should be a 5 μm small hole on the lid, and this small aperture needs to be perfectly aligned with the PCA gap inside the mount. In this way, regardless of the beam size of the laser, only a 5-μm-sized beam will be able to penetrate the lid and reach the PCA gap. A more detailed measurement plan will be presented in the Future Work section in the final chapter.

3.7 Summary

In this chapter, a THz spiral PCA for THz imaging has been designed, and GQD is used to enhance the performance of this PCA. In order to make the simulation results more accurate, a simulation method based on COMSOL-CST was proposed and elaborated in detail. This method uses COMSOL to simulate the surface current, and uses the surface current data as the excitation signal for the antenna simulation in CST. A reference PCA was used as an example. In COMSOL, the surface current was simulated, and this reference

PCA was fabricated and used for surface current measurement. The measurement results show that, taking into account various factors, although there is a slight error, it can still be concluded that the theoretical value and the actual value of the surface current are consistent. This demonstrates the accuracy of the COMSOL-CST simulation method, so this approach is worthy of being referred to and used by researchers in related fields. The design, simulation and fabrication of the spiral PCA are all elaborately described. On the premise of achieving good simulation results, the spiral PCA has been successfully fabricated and the first surface current measurement is conducted. Then, GQD is deposited on its surface, and the second surface current measurement is carried out afterwards. The measurement results show that GQD can increase the surface current, and as the laser power and bias voltage increase, the enhancement effect of GQD on the surface current also increases. This result is in line with the theoretical findings that GQD can increase the carrier density. It provides reference information for researchers studying GQD and contributes to the field of PCA enhancement.

Chapter 4

THz Photoemitter Based on Inter-Combined Tai-Chi Electrodes and MoS2-GaAs Structure for Skin Cancer Detection

A major challenge in cancer diagnosis in its early stage is the asymptomatic nature, as the absence of symptoms will cause serious consequences in treatment. Cancers usually have more water than healthy human tissues, thus THz detection can be used to distinguish cancer cells as THz waves are highly sensitive to water. Numerous studies have demonstrated that THz technology is feasible on detection of cancer tissues, such as skin cancer [187], cervical cancer [16], liver cancer [188], breast cancer [189], stomach cancer [190], colon cancer [191], etc. As a promising THz emitter, THz PCA will become one of the cornerstones in the future medical field and relevant THz applications if it can meet the requirements of cancer detection. In this chapter, a novel PCA design based on ancient oriental totem Tai-Chi and MoS_2-GaAs structure has been proposed, simulated, and fabricated. Measurement of the surface current is completed to verify the enhancement effect introduced by the MoS_2 monolayers. The results show that this PCA can work at a wide band within THz frequency range from 0.3 to 1.7 THz, and its peak performance lies between 1 and 1.5 THz, which is suitable for skin cancer detection (the absorption in the tumor area are higher compared to normal tissues within 0.1 - 4 THz [192]).

4.1 Permitivity of Human Skin

The PCA design becomes more complicated because of the absorption to THz radiation of the human skin. Human skin is a complex, anisotropic and heterogeneous medium, where small parts like blood vessels are distributed in different depth [193]. Considering its complexity, it is challenging to accurately describe human skin in simulations, mainly due to the shape and function, and most importantly because of the absence of the dielectric constant measurements at high frequency [194]. That is the reason why most latest research simulates the human skin only applying the most essential parts, which are the three layers of epidermis, dermis, and hypodermis, shown in Figure 4.1 [195].

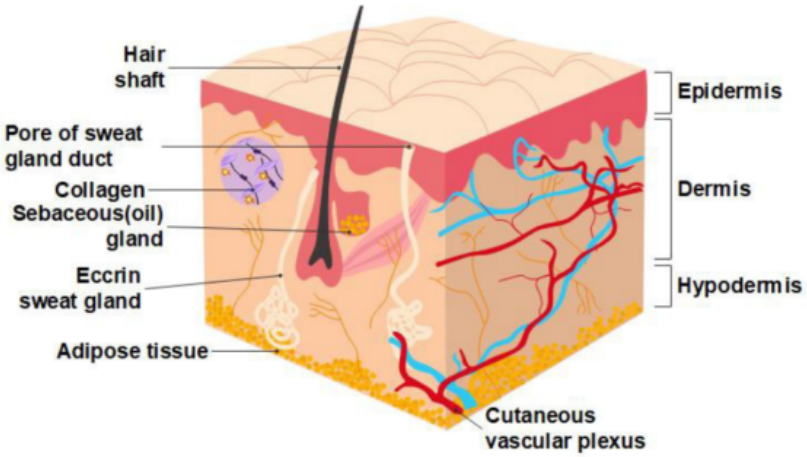

Figure 4.1: Illustration of human skin. [195]

The thickness of epidermis and dermis are 0.05 - 1.5 mm and 1.5 - 4 mm, which varies from person to person [196]. There is no typical value for hypodermis [196]. Most skin cancers (such as basal cell carcinoma and squamous cell carcinoma) originate in the epidermis at an early stage, and it is only in the later stages that they penetrate deeper layers of the skin (the dermis). The Tai-Chi PCA designed in this study is specifically for detecting the asymptomatic skin cancer at its early stage, thus its detection depth targets to cover the entire epidermis layer. Of course, if possible, it would be better if the radiation from the designed THz PCA can cover the dermis layer as well. The human skin model created in this PhD study contains the first two layers without hypodermis. The epidermis has two

layers, one is the actual living epidermis layer, and the other one consists of only dead cells. The stratum corneum covers on the outer surface of epidermis. Under epidermis layer, it is the dermis that supports the epidermis layer. The permittivity of the human skin tissues can be obtained by Equation [197]:

$$\varepsilon'(\omega) = \varepsilon_\infty + \frac{\varepsilon_s - \varepsilon}{1+(\omega\tau_1)^2} + \frac{\varepsilon - \varepsilon_\infty}{1+\omega\tau_2)^2} \tag{4.1}$$

$$\varepsilon''(\omega) = \frac{(\varepsilon_s - \varepsilon)(\omega\tau_1)}{1+(\omega\tau_1)^2} + \frac{(\varepsilon - \varepsilon_\infty)(\omega\tau_2)}{1+(\omega\tau_2)^2} \tag{4.2}$$

where ε_s is the static dielectric constant, ε is an intermediate frequency limit, and ε_∞ is the limiting value at high frequency [198]. Parameter of human skin values are listed in Table 4.1.

Table 4.1: Parameter of human skin

Reference	**Model**	ε_s	ε	ε_∞	τ_1 (ps)	τ_2 (ps)
Ref [199]	Epidermis	58.0	3.6	3.0	10.0	0.20
Ref [200]	Dermis	60.0	3.6	3.0	9.4	0.18

Using Equation 4.1 and 4.2 and the values listed in Table 4.1, the permittivity of human skin for THz frequency range can be calculated. Figure 4.2 shows the real and imaginary part of the dielectric constant of the human skin model, describing how THz waves behave throughout the stratum corneum/epidermis/dermis layers. Figure 4.3 shows the created model of human skin in CST. In simulation, the proposed PCA is placed on the top of human skin, while a probe is positioned beneath dermis.

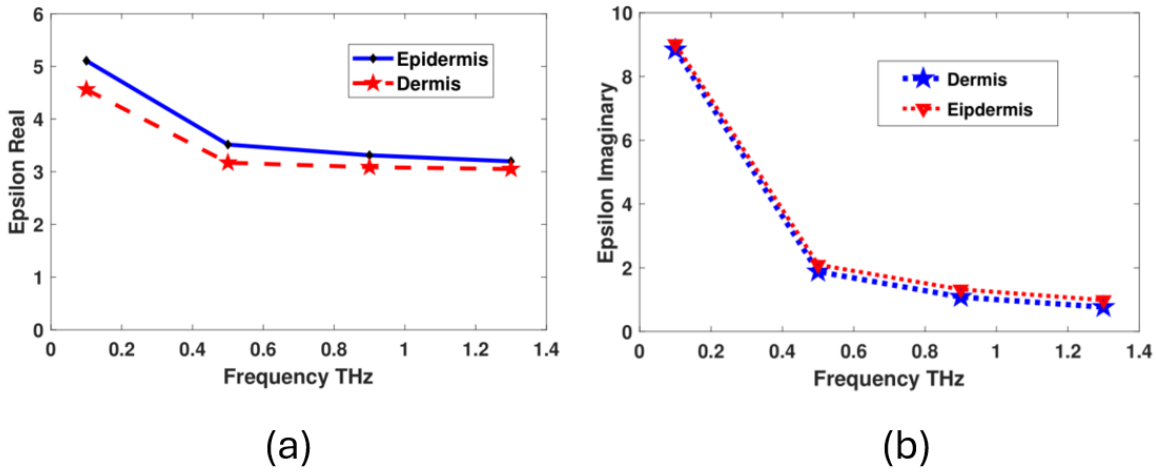

Figure 4.2: (a) Real part and (b) Imaginary part of permittivity of human skin.

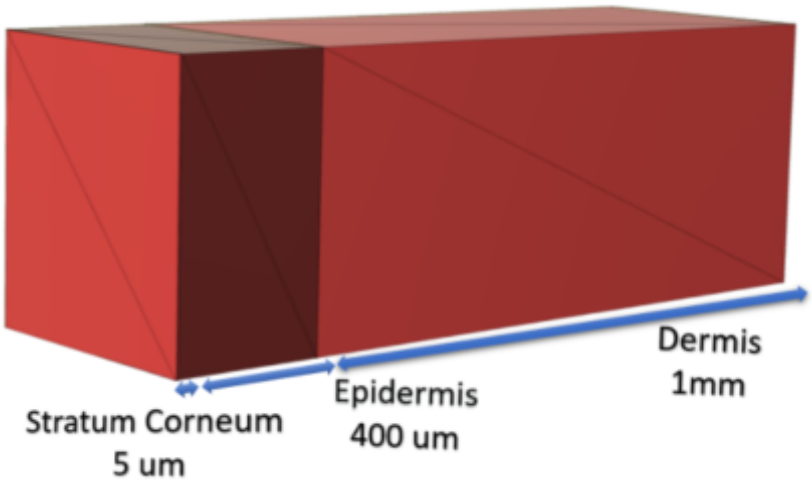

Figure 4.3: Simulation of human skin in CST. This human skin model consist of stratum corneum layer, epidermis, and dermis.

4.2 Employing MoS_2 to Simulation

In COMSOL, the corresponding material 'MoS2 (Molybdenum disulfide) (Islam et al. 2021: monolayer (1L) film; n,k 0.190-1.70 um)' can be easily accessed for the simulation. However in CST Studio 2020, MoS_2 needs to be created by the user. As the real and imaginary parts of the complex dielectric constant of MoS_2 follow Drude model, the MoS_2 layer is modeled using the Drude model function along the frequency from 0.1 THz to 3 THz in CST. The dielectric function of MoS2 can be described as [201]:

$$\varepsilon(\omega) = [n(\omega) - i\kappa(\omega)]^2 = \varepsilon_\infty + \frac{\omega_p^2}{\omega_D^2 - \omega^2 - i\Gamma\omega} \tag{4.3}$$

In Equation 4.3, ε_∞, ω_D, ω_p, and Γ represent the high-frequency dielectric constant, resonant frequency, oscillator strength, and damping constant of the mode, respectively. In the simulation, the patterned monolayer MoS_2 flakes are constructed as squared patches between two electrodes, which is introduced in the following section.

4.3 THz PCA based on Tai-Chi Electrodes and MoS2-GaAs Structure

4.3.1 Target PCA Operating Band for Skin Cancer Detection

In biological tissues, water molecules are the main reason of THz radiation absorption. As mentioned earlier, the THz waves between 0.1 and 4 THz exhibit a high absorption rate in the tumor area compared to healthy tissues, making itself a promising tool in cancer detection. Therefore, the working frequency of the designed THz PCA needs to be within

this frequency range. Meanwhile, the wider the frequency band, the better it can meet the requirements for cancer detection. To achieve this goal, the proposed Tai-Chi PCA is designed with an optimized structure targeting at a wideband emission from 0.3 to 2 THz.

4.3.2 PCA Design

The proposed PCA is formed from a SI-GaAs substrate and Tai-Chi shaped 5/195 nm Ti/Au electrodes. The Tai-Chi geometric structure and contact fingers at PCA gap are introduced because the local E-field will be strengthened by inter-combined structures. Figure 4.4 illustrates the structure of the proposed PCA structure and the plasmonic contact fingers. The overall structure is based on the ancient oriental totem Tai-Chi shown in Figure 4.5, which was first mentioned in The Book of Changes.

The electrodes consist of one outer circle and two smaller inner half-circles. The frequency range and the outer circumstance of circular-shaped PCA is studied in Equation **??**. To meet the frequency requirement mentioned earlier, D is determined to be 900 μm. The dimensions of the PCA in simulations are detailed in Table 4.2. The PCA gap size that not presented in Figure 4.4 is $G = 5$ μm.

Table 4.2: Corresponding values of electrodes and substrate dimensions of the proposed Tai-Chi PCA

Dimensions	R_1	R_2	r_1	r_2	G_1	G_2
Values (μm)	450	400	200	150	10	100
Dimensions	h (height of electrodes)		L (length of substrate)		H (height of substrate)	
Values (μm)	0.2		2000		450	

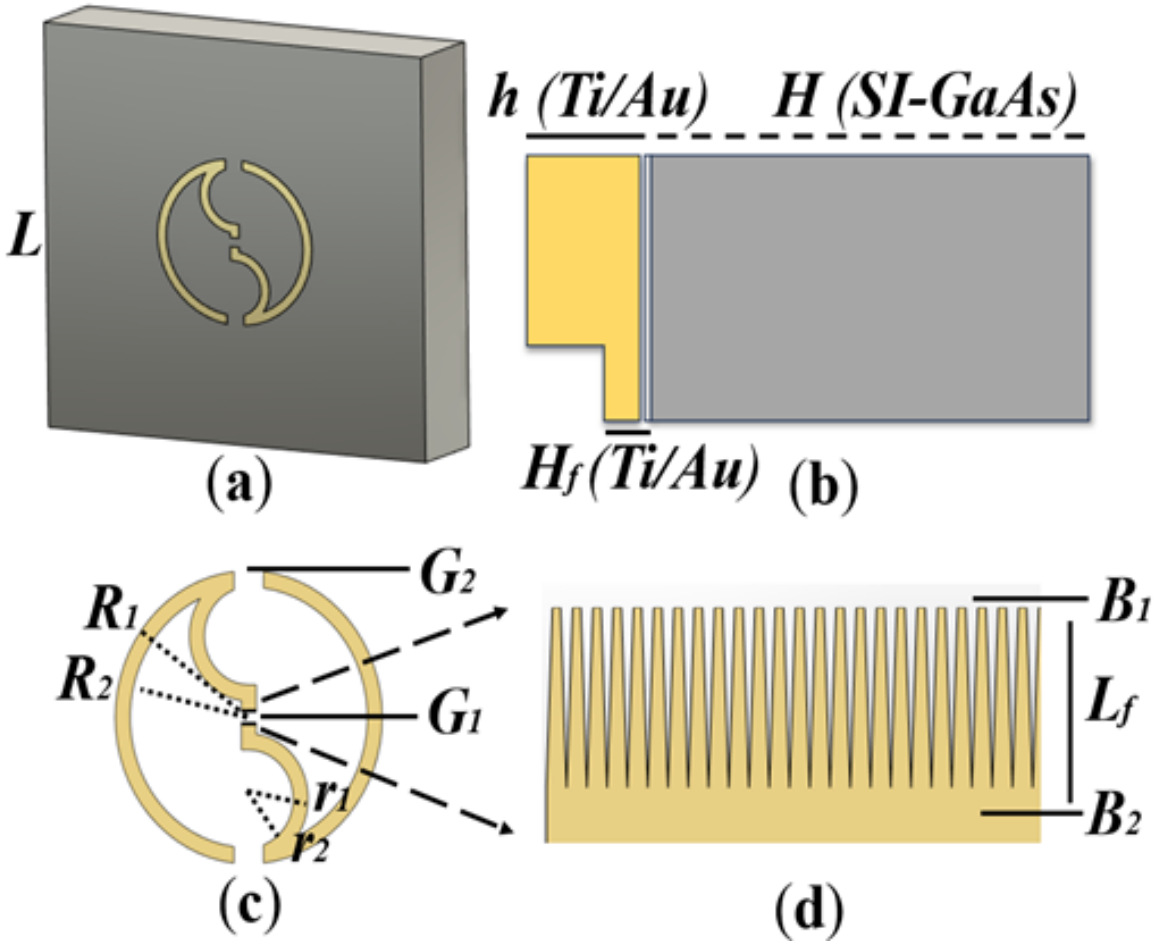

Figure 4.4: (a) Proposed Tai-Chi PCA made of two gold electrodes based on an SI-GaAs substrate; (b) Side view and the height information of electrodes, contact fingers, and substrate part of the proposed PCA; (c) Front view of the electrodes and the dimension information; (d) Zoomed view of the contact fingers and the dimension information.

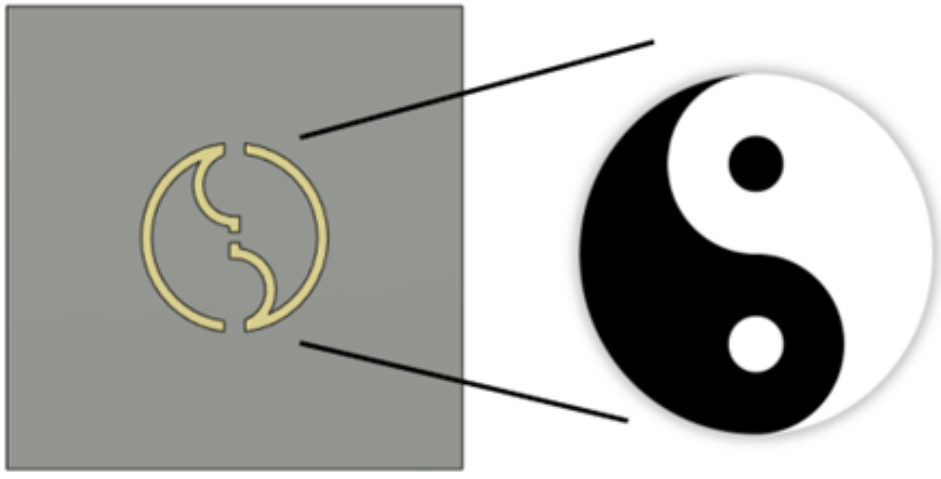

Figure 4.5: The comparison between the proposed Tai-Chi PCA and the traditional pattern of the Tai-Chi totem

The simulated dimensions of the contact fingers and MoS_2 monolayers are listed in Table 4.3. The thickness of monolayer MoS_2 is $\approx$ 0.646 - 0.78 nm, therefore the patterned MoS_2 monolayer flakes in the simulation are set to be 0.78 nm. The creation of MoS_2 in CST follows Drude Model and has been discussed in previous section, the dielectric function of MoS_2 is defined by Equation 4.3.

Table 4.3: Corresponding values of the contact fingers

Dimensions	B_1 (finger upper base)	B_2 (finger lower base)	L_f (length of fingers)	H_f (height of fingers)	L_m (MoS_2 side length)	H_m (MoS_2 height)
Values (μm)	0.2	0.2	1	0.05	0.1	0.00078

Due to the inter-combined Tai-Chi structure, the plasmonic contact fingers, and the MoS_2 monolayers, the laser absorption efficiency can enhanced, The electron oscillations that are excited by the optical pump will significantly boost the E-field near the PCA gap, leading to higher radiation performance. The simulation results will be discussed in the next section.

4.4 Simulation Results and Discussion

4.4.1 Results and Comparisons of the MoS_2-GaAs Tai-Chi PCA

The simulation results of the proposed MoS_2-GaAs Tai-Chi PCA have been compared to the reference PCA in Chapter 3, using a field probe positioned at the same distance from the PCA gap. The farfield radiation pattern is shown in Figure 4.6.

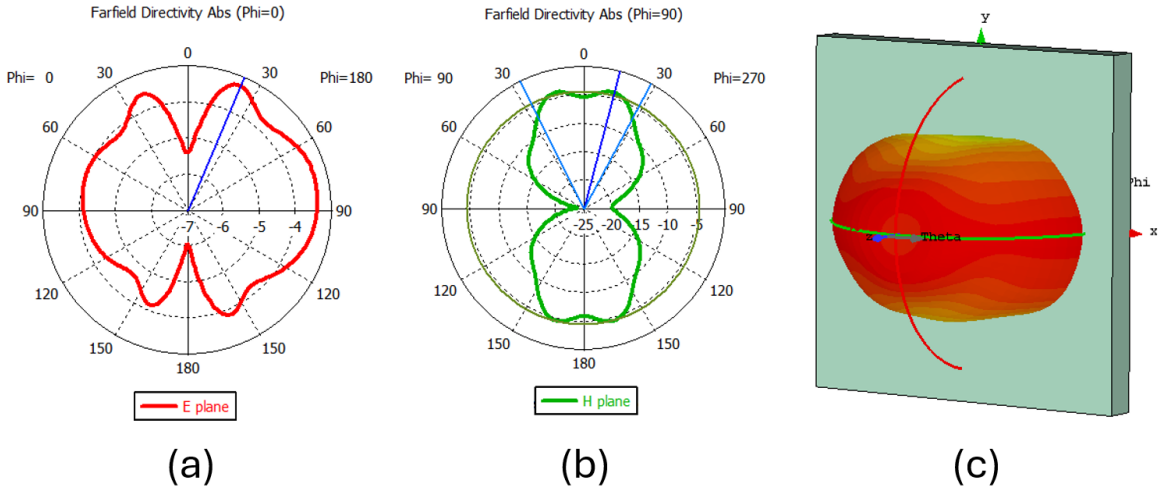

Figure 4.6: The farfield radiation pattern of the proposed MoS_2-GaAs Tai-Chi PCA on (a) E plane and (b) H plane. (c) 3D farfield radiation pattern of the MoS_2-GaAs Tai-Chi PCA.

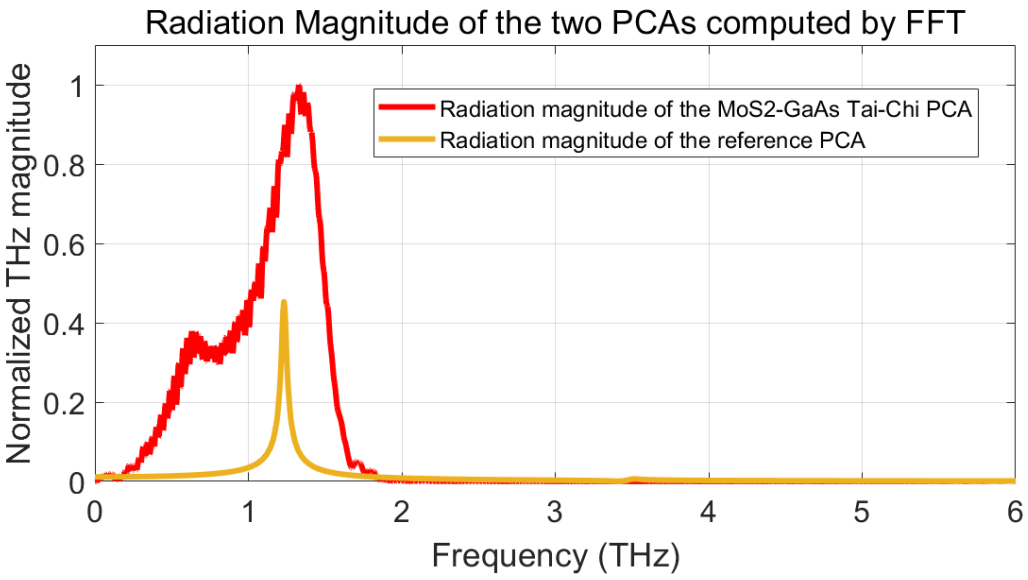

Figure 4.7: Comparison of the simulated radiation magnitude. The red line is the simulated radiation magnitude of the proposed MoS_2-GaAs Tai-Chi PCA, and the orange line represents the radiation magnitude of the reference PCA in Chapter 3. The detecting probe is positioned at the same distance from PCA.

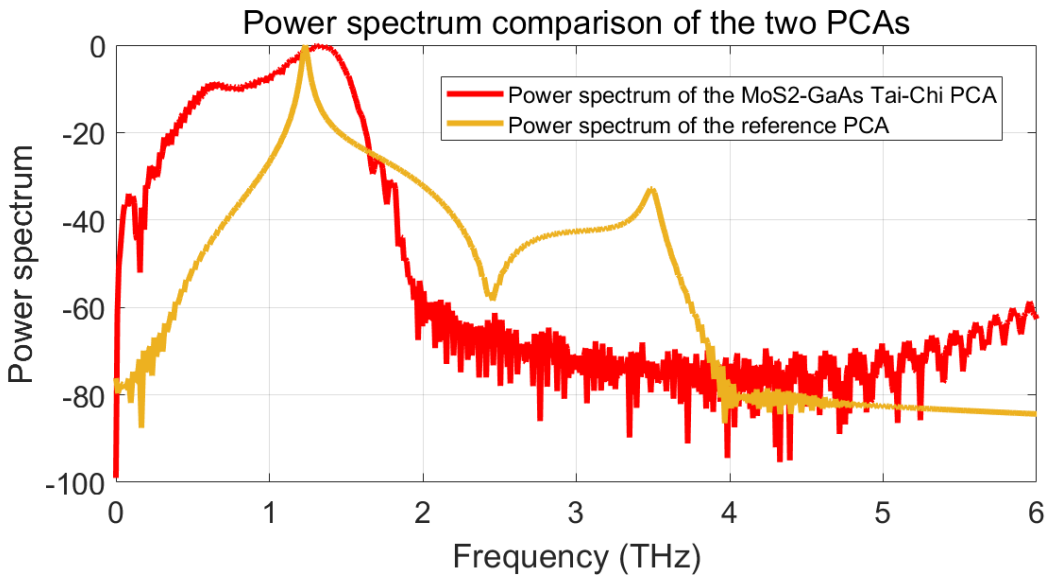

Figure 4.8: Comparison of the simulated power spectrum. The red line is the simulated power spectrum of the proposed MoS_2-GaAs Tai-Chi PCA, and the orange line represents the power spectrum of the reference PCA in Chapter 3. The detecting probe is positioned at the same distance from PCA.

Figure 4.7 is the comparison of the radiation magnitude. The detecting probe is positioned at 0.5 mm from the back side of both PCAs. It can be observed that the radiation of the proposed Tai-Chi PCA outclasses the reference PCA. Moreover, the wide band from 0.3 to 1.7 THz is also a great advantage of the proposed Tai-Chi PCA, as the reference PCA only shows good radiation between 1.1 and 1.3 THz. According to the -3 dB standard, the proposed Tai-Chi PCA obtains stable performance within the frequency range of 1 - 1.5 THz. The Figure 4.8 is the comparison of the power spectrum of the two PCAs, and we can come to the same conclusion that the performance of the Tai-Chi PCA exceeds the reference PCA to a large extent. These comparisons indicate that the integration of the MoS_2-GaAs structure combined with the novel Tai-Chi electrodes and contact nanofingers effectively enhance both the radiation intensity and the operational bandwidth.

To compare the optical-to-THz conversion enhancement from MoS_2 and contact fingers, The radiation performance and E-field distribution of the proposed MoS_2-GaAs Tai-Chi PCA have been compared to the non-MoS_2 simulation results and other published works. Table 4.4 lists the radiation performance of the proposed Tai-Chi PCA and three other

published PCAs. All data used in the table is the peak value in the corresponding research. Their bandwidth, E-field strength and directivity varies due to different substrate materials. By comparison, it can be noticed that the proposed work obtains a wide band THz radiation, and the directivity is also higher.

Table 4.4: Values of radiation performance of the proposed MoS_2-GaAs Tai-Chi PCA compared to other published PCA designs

PCA design	Substrate	Bandwidth (THz)	Directivity (dBi)	3dB Angular width (deg)	Side lobe level (dB)
Proposed Tai-Chi PCA	MoS_2-GaAs	1.4	21.3	26.0	-2.8
Ref [179]	Graphene-GaAs	0.7	13.74	45.9	-2.5
Ref [88]	LT-GaAs	0.181	13.3	N/A	-11.2
Ref [184]	LT-GaAs	7.93	7.7 - 11	N/A	N/A
Ref [185]	Quartz	3	18.2	N/A	N/A

Figure 4.9 (a), (b) and (c) compare the E-field distribution of the proposed Tai-Chi PCA with MoS_2 and contact fingers, the Tai-Chi PCA with only contact fingers but no MoS_2, and the Tai-Chi PCA with plane antenna gap. It is obvious that the performance of these three is ranked from high to low. This is because the MoS_2 and contact fingers both increase the radiation power by improving the electric density at the PCA gap.

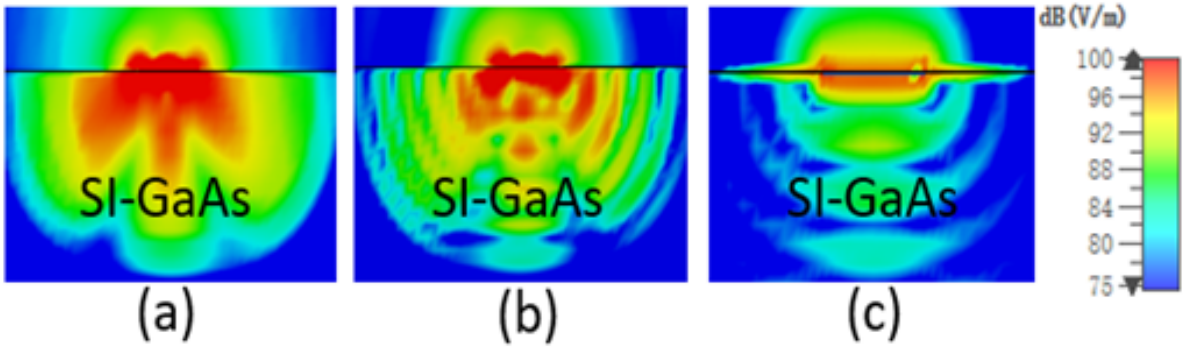

Figure 4.9: Simulated E-field distribution in the proposed Tai-Chi PCA (a) with MoS_2 and contact nanofingers; (b) with contact nanofingers but without MoS_2; (c) without MoS_2 or contact nanofingers.

By comparisons, a conclusion can be made that the proposed MoS_2-GaAs Tai-Chi PCA not only has broad bandwidth, but also obtains high radiation performance.

4.4.2 Results of the Proposed PCA on Human Skin

A model of human skin has been created in CST to examine how they affect the PCA ability to operate. The positioning of the model and the PCA is shown in Figure 4.10. This human skin model is composed of two main layers, and there is a sub-layer combined to the epidermis layer on the top (stratum corneum), as discussed in the previous section. To fulfill the aims that detecting early-stage skin cancer in epidermis, a probe has been placed at the junction of the epidermis layer and the dermis layer. Another field probe is located at the bottom of dermis layer, evaluating the operation ability of the MoS_2-GaAs Tai-Chi PCA penetrating the human skin. We deliberately set the position of the human skin model at a distance of 95 μm from the bottom of the Tai-Chi PCA. Thus, the epidermis-dermis boundary is exactly 0.5 mm from the bottom of the PCA. This ensures that the distance from the probe to the PCA back side is the same as that in the reference PCA simulation.

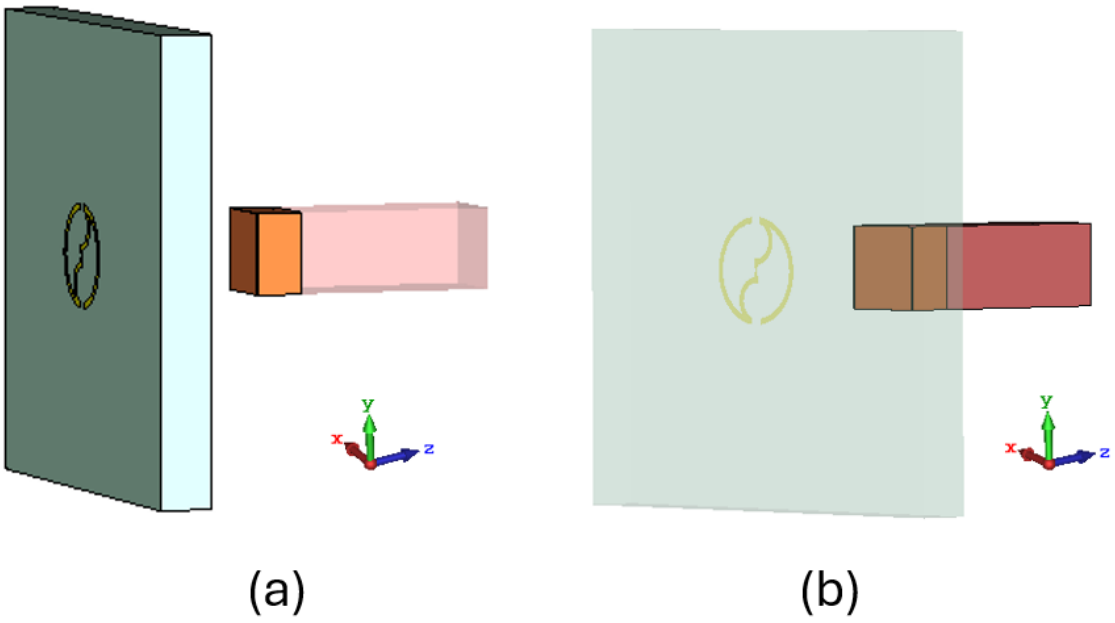

Figure 4.10: (a) CST model of the proposed MoS_2-GaAs Tai-Chi PCA on human skin; (b) A transparent view of the Tai-Chi PCA with the developed human skin model positioned at the back side.

Figure 4.11 and 4.12 indicates the comparison between the radiation magnitude and E-field density of the three scenarios: the operational performance of proposed PCA in the air, at the epidermis-dermis boundary, and beneath the dermis. Regarding to these figures, the radiation at both the epidermis layer and the dermis layer have been reduced at different levels. The results show that the peak value of THz radiation detected at the epidermis-dermis boundary is reduced by approximately 50% at 1 THz, while the THz radiation detected at the end of the dermis layer is only 10% of the original intensity. In time domain, the peak value of the E-field on the epidermis-dermis boundary and the bottom of the dermis layer are also reduced to approximately 50% and 10% compared to the data in air.

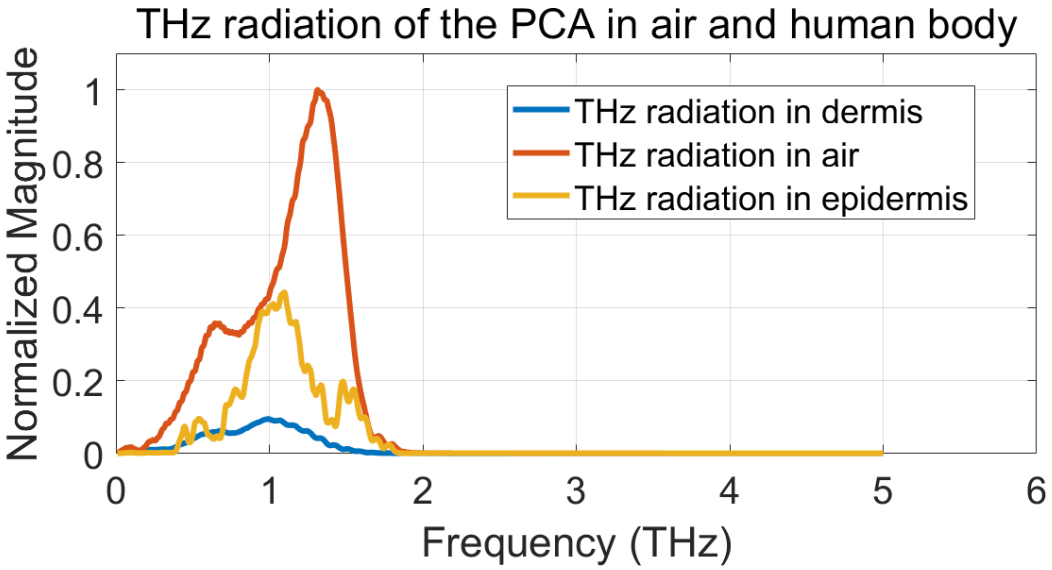

Figure 4.11: The experimental THz radiation magnitude from the proposed MoS_2-GaAs Tai-Chi PCA. The red line is the radiation detected in air, the distance between probe and the bottom of PCA is the same as the probe for epidermis. The orange line represents the radiation detected at the epidermis-dermis boundary, and the blue line represents the radiation detected at the bottom of the dermis layer.

These simulation results appear to have decreased significantly compared to the original results. However, this does not mean that the proposed MoS_2-GaAs Tai-Chi PCA cannot be used for detecting skin cancer. Compared with the reference PCA in Chapter 3, the THz waves emitted by the proposed Tai-Chi PCA still have considerable intensity at these two positions. The comparison results are shown in Figure 4.13 and Figure 4.14. It indicates that the proposed MoS_2-GaAs Tai-Chi PCA has a comparable performance at the epidermis-dermis boundary. The bandwidth is still higher than the reference PCA

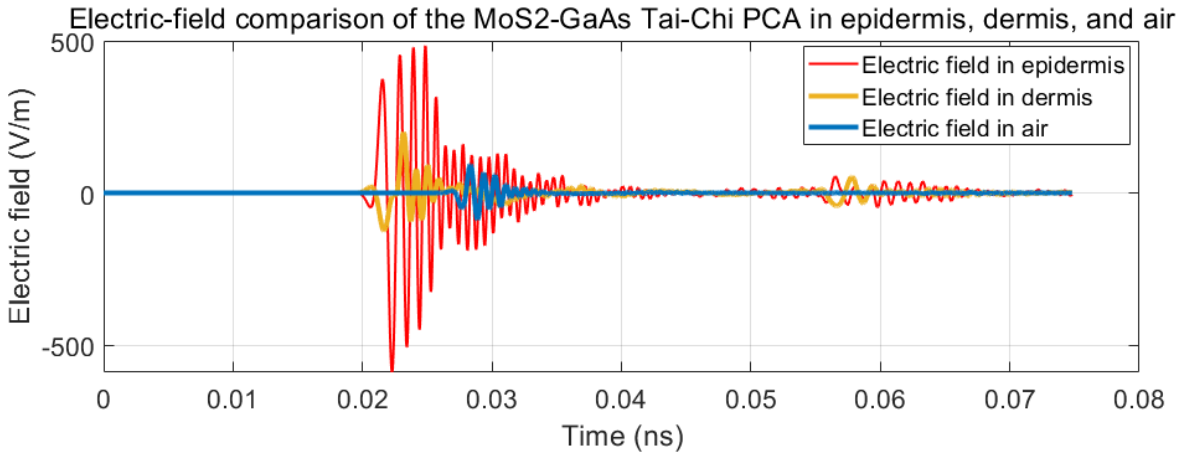

Figure 4.12: The experimental electric-field comparison. The red line is the E-field detected in air, the distance between probe and the bottom of PCA is the same as the probe for epidermis. The orange line represents the E-field detected at the epidermis-dermis boundary, and the blue line represents the E-field detected at the bottom of the dermis layer.

in Chapter 3. The peak E-field of the proposed PCA is also considerable compared to that of the reference PCA in the air. In fact, the THz signals detected at the bottom of the dermis layer can still be regarded as gaining a good performance due to its visible intensity from Figure 4.11, 4.14 and 4.13.

By comparison, we expect the proposed MoS_2-GaAs Tai-Chi PCA to be able to work at a distance of up to 1 mm inside human skin, even deeper. This region conatins the epidermis layer and the dermis layer, where pigment cells lie. Since most of early-stage skin cancers occur in the epidermis layer, the proposed Tai-Chi PCA should be highly effective for detecting such skin cancers.

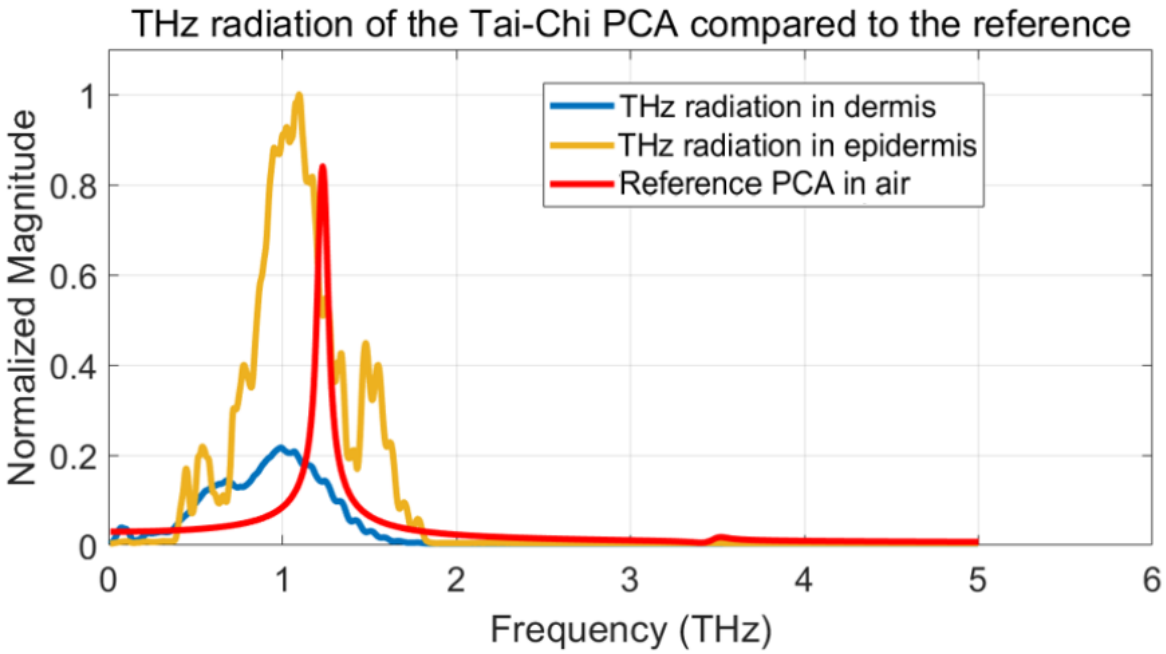

Figure 4.13: The experimental THz radiation magnitude from the proposed MoS_2-GaAs Tai-Chi PCA compared to the reference PCA in Chapter 3. The red line is the radiation detected from the reference PCA in air (the same data to Figure 4.7. The orange line represents the radiation of Tai-Chi PCA that detected at the epidermis-dermis boundary, and the blue line represents the radiation detected at the bottom of the dermis layer.

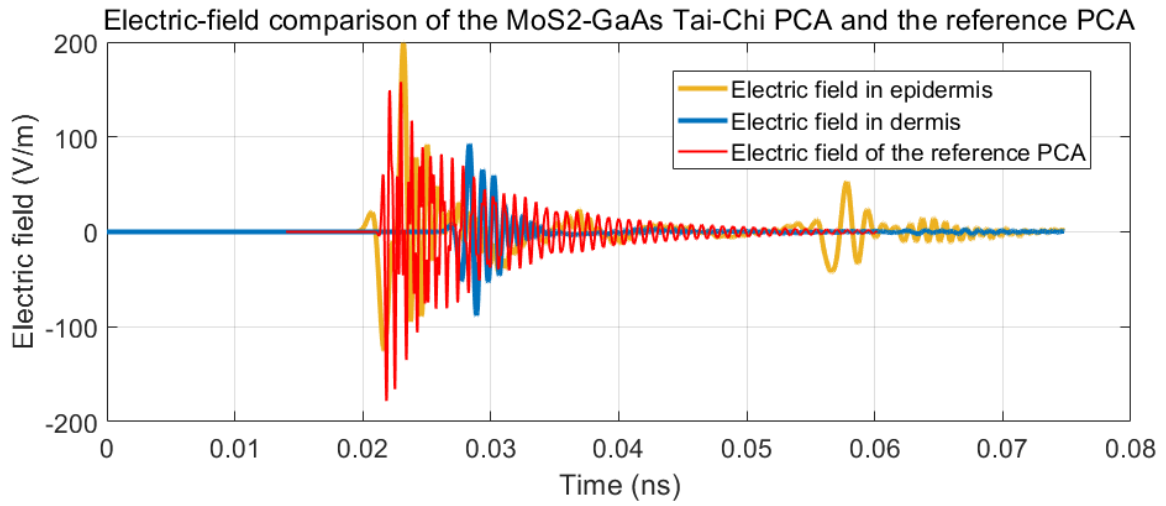

Figure 4.14: The experimental electric field respect in time domain. The red line is the E-field of the reference PCA radiates in air. The orange line represents the E-field of Tai-Chi PCA that detected at the epidermis-dermis boundary, and the blue line represents the E-field detected at the bottom of the dermis layer.

4.5 Fabrication of the MoS_2-GaAs Tai-Chi PCA

The proposed Tai-Chi PCA has been fabricated in James Watt Nanofabrication Centre (JWNC) in University of Glasgow. The process of E-beam lithography, metalisation and liftoff have been introduced in Chapter 3, and the deposition of MoS_2 monolayers is introduced in this section. The silver conductive gel is used to connect the bias voltage to the PCA.

4.5.1 Deposition of Monolayer MoS2 on SI-GaAs

In E-beam lithography process, the deposition of MoS_2 should be completed before spinning PMMA. Figure 4.16 shows the new E-beam lithography steps with MoS_2 deposition. As discussed in Chapter 2, patterned MoS_2 monolayers will be utilized in the PCA instead of a complete monolayer that covers the whole substrate. To deposit small MoS_2 flakes, MoS_2 crystal provided by Graphene Supermarket has been purchased, and monolayer MoS_2 has been obtained from the bulk crystal using the tape exfoliation method. During the deposition, the tape with MoS_2 monolayer needs to be perfectly attached to the GaAs surface. The tape loses its stickiness when heated, therefore the sample with tape needs to be placed on a hotplate for a few seconds. Once the tape changed color, the MoS_2 has been successfully transferred onto the substrate surface. Figure 4.15 is a picture of operating this process. The MoS_2 on the substrate is actually not a complete layer, but to make the illustration clearer, the MoS_2 in Figure 4.16 has been painted in a crystal layer form.

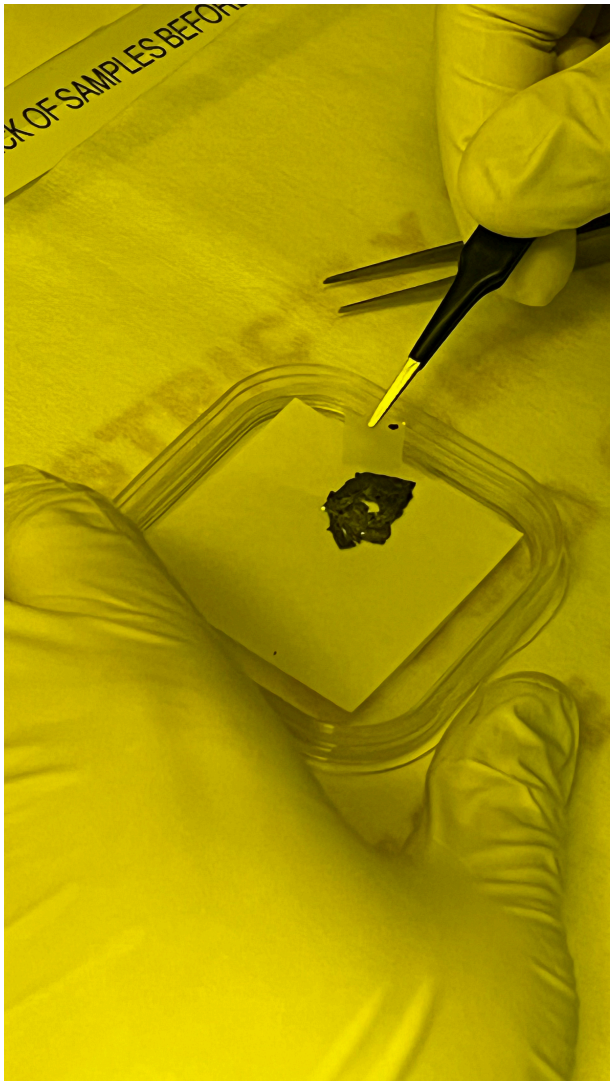

Figure 4.15: Using tapes to obtain MoS_2 monolayer from the bulk crystal

The MoS_2 deposition needs to be completed before E-beam lithography so that only the MoS_2 flakes at the PCA gap will be able to be exposed to the laser. The MoS_2 flakes outside the PCA gap region is covered by the metal electrodes, which can prevent unnecessary laser absorption that could interfere the PCA operation. Since the thickness of the MoS_2 monolayer is extremely thin, even if there are flakes beneath the electrodes, their effect on the THz emission can be ignored. The MoS_2 deposition along with the E-beam lithography process can be shown in Figure 4.16.

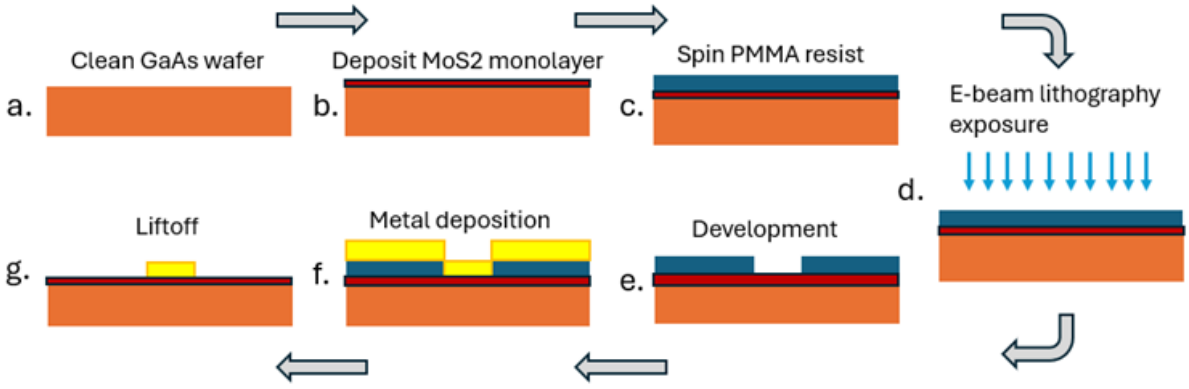

Figure 4.16: Deposition of MoS_2 in PCA fabrication.

After depositing MoS_2 to the surface of SI-GaAs, the subsequent fabrication steps such as E-beam lithography and metallisation and liftoff are proceeded in JWNC. The progress of the PCA fabrication has been introduced in the previous chapter. Figure 4.17 shows a clear zoomed-in microscope image, revealing the distribution of small monolayer MoS_2 flakes on the PCA gap. The magnification of optical microscope is limited, thus the clearer images from SEM will be presented in the next section.

4.5.2 Connecting bias to Tai-Chi PCA using silver conductive gel

To apply bias voltage to the PCA, two biasing pads have been added to both electrodes in the fabrication. Figure 4.18 is a picture of connecting the wires to the pads using silver conductive gel.

Figure 4.17: Microscope image of the Tai-Chi PCA with MoS_2 monolayer flakes on the surface and within the PCA gap.

Figure 4.18: Connecting wires to the biasing pads of Tai-Chi PCA using silver conductive gel.

A successfully fabricated Tai-Chi PCA sample connected to BNC cable that provides bias voltage, and the Tai-Chi PCA mounted on a holder connected to bias voltage, are shown in Figure 4.19 and Figure 4.20.

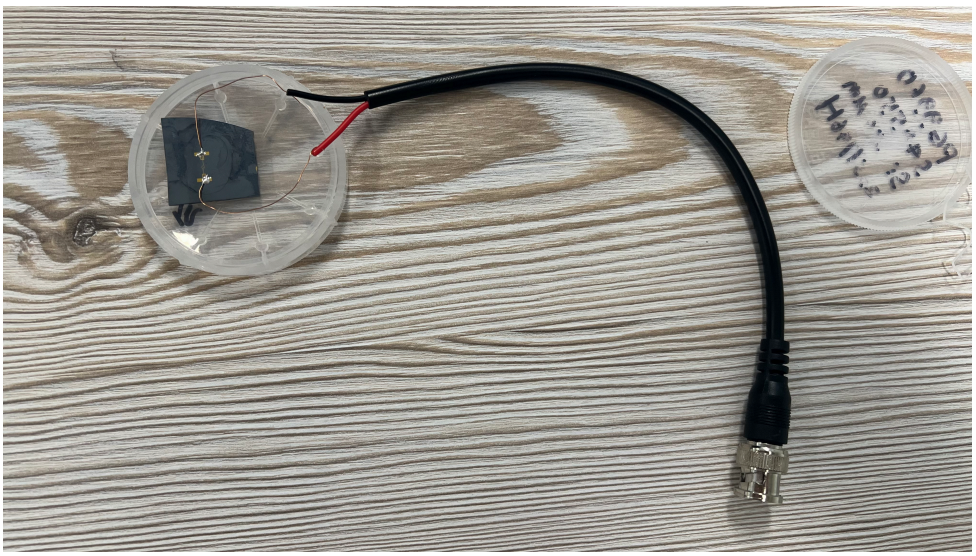

Figure 4.19: A successfully fabricated Tai-Chi PCA has been connected to BNC cable for applying bias voltage.

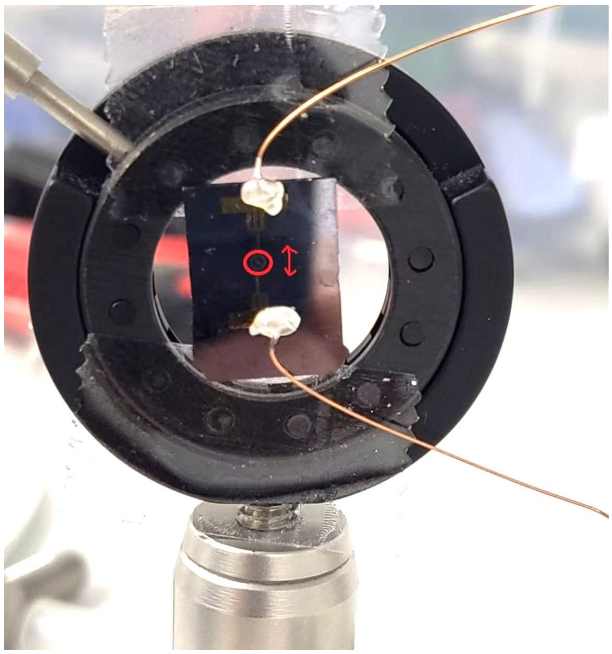

Figure 4.20: The mounted Tai-Chi PCA connected to bias voltage.

SEM figures of the fabricated Tai-Chi PCA and the contact fingers are shown in Figure 4.21.

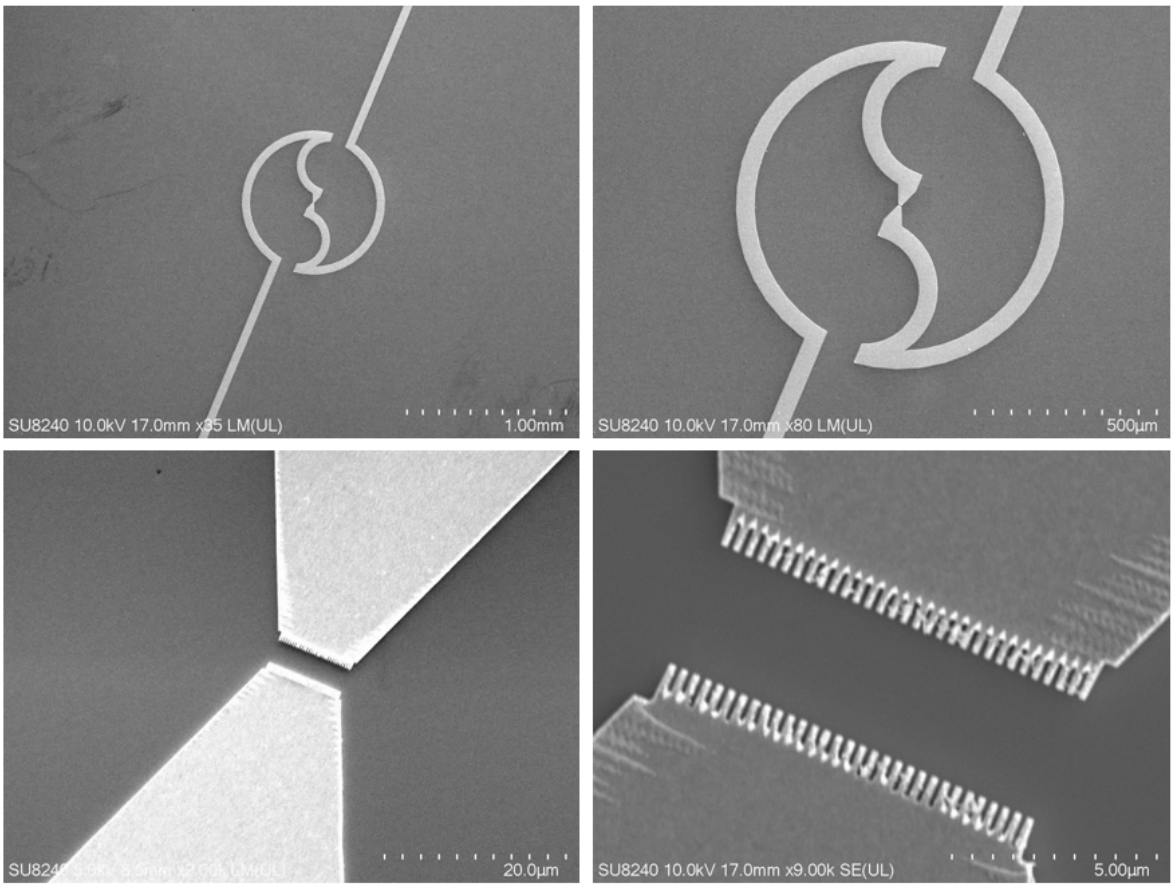

Figure 4.21: The fabricated Tai-Chi PCA under SEM. The contact nanofingers are successfully fabricated at PCA gap, and the two lines extending out from the electrodes are used for connection with the biasing pads.

4.6 Tai-Chi PCA Measurement

In this section, a series of experiments have been accomplished, such as SEM observation and Raman Spectroscopy on the substrate to detect the existence of MoS_2, and surface current measurement at the PCA gap.

4.6.1 Raman Spectroscopy and SEM of the MoS2-GaAs Tai-Chi PCA

Raman spectroscopy and SEM have been employed to verify the MoS_2 transfer.

Figure 4.22 shows the Raman spectroscopy of the fabricated MoS_2-GaAs Tai-Chi PCA. The two peaks at approximately 386 and 406 cm^{-1} are E^1_2g and A_{1g} of MoS_2, representing in-plane vibrations and out-of-plane vibrations. The difference of these two modes can be used as a reliable identification for monolayer MoS_2, in which the shift between the two peaks is commonly 18 - 20 cm^{-1} [202]. In Figure 4.22, the distance between two peaks is $\Delta = E^1_{2g} - A_{1g} \approx 20cm^{-1}$. The lower peaks in Figure 4.22 at x $\approx$ 292 and $\approx$ 450 are GaAs and 2LA(M) of MoS_2.

Figure 4.23 shows the SEM diagram of the Tai-Chi PCA with MoS_2 within the PCA gap. The deposited MoS_2 is clearly visible between the two electrodes, confirming that the transfer process is fulfilled. Although there are MoS_2 flakes on the surrounding areas, they will not influence the PCA performance because the laser beam with a proper spot size will be focused within the gap, and the surface current measurement only evaluate the current behaviour within PCA gap.

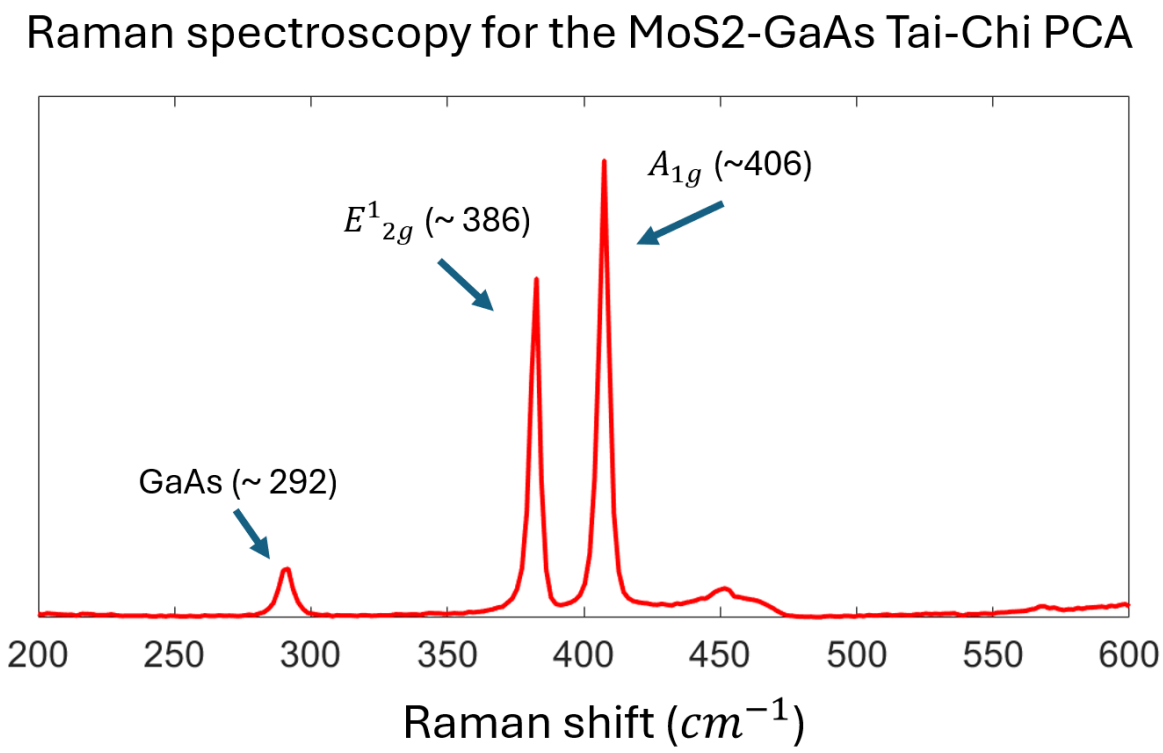

Figure 4.22: The Raman spectroscopy of the MoS_2-GaAs Tai-Chi PCA. The peaks at x=382 and x=410 indicate that MoS_2 is successfully transferred to the PCA surface.

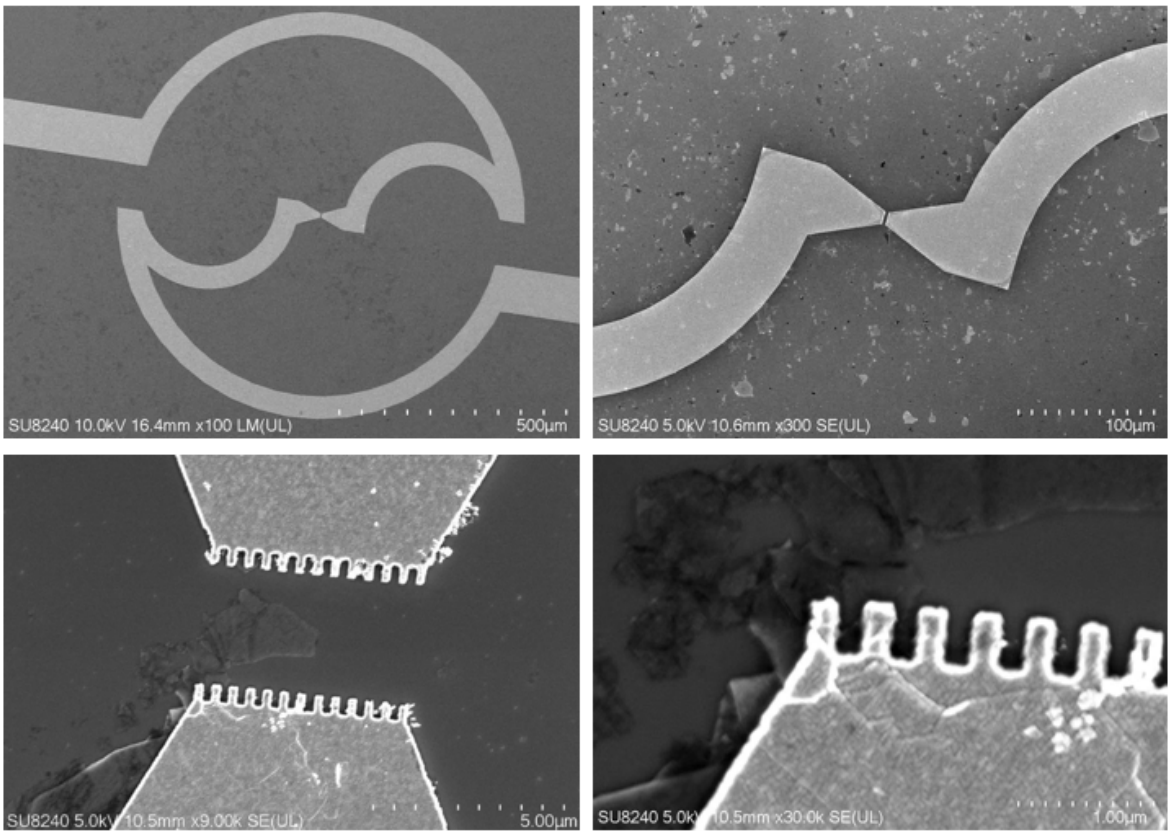

Figure 4.23: MoS_2 monolayers within the PCA gap under SEM.

Through Raman spectroscopy and SEM, it can be confirmed that patterned monolayer MoS_2 flakes have been deposited to the PCA within the gap between electrodes as expected. The MoS_2-GaAs Tai-Chi PCA is successfully fabricated.

4.6.2 Surface Current Measurement and Comparison

The surface current measurement at PCA gap has been proceeded with various bias voltage in order to explore comprehensive characterization of the PCA performance. The experimental setup has been introduced in the surface current measurement section in Chapter 3. Firstly, the surface current under zero bias is tested and given in Table 4.5. In this measurement, only the laser has been applied and no bias voltage was present. Therefore, the surface current obtained was entirely dependent on the movement of carriers.

Table 4.5: Surface current detection at the Tai-Chi PCA gap with zero-bias

Laser power (mW)	5	10	15	20
Surface current of Tai-Chi PCA without MoS_2 (μA)	1.56	4.48	5.45	7.39
Surface current of Tai-Chi PCA with MoS_2 (μA)	2.01	6.70	10.81	18.30

The laser employed in this experiment is from an Tsunami Ti:Sapphire Oscillator in Queen Mary University of London. The surface current of Tai-Chi PCA without MoS_2 is 1.56, 4.48, 5.45, and 7.39 μA under 5, 10, 15, and 20 mW laser. By contrast, the surface current of Tai-Chi PCA with MoS_2 under 5-20 mW laser is 2.01, 6.70, 10.81, 18.30 μA, respectively. It can be observed that the small patterned MoS_2 monolayer flakes significantly enhances the surface current within the antenna gap. This result indicates that the carrier activity

in the GaAs substrate is improved by the presence of MoS_2, which is consistent with the research in Chapter 2 and can confirm the contribution that MoS_2 monolayers enhance the laser absorption, leading to a boosted PCA performance by improving optical-to-THz conversion efficiency.

After applying bias voltage, significant changes in the surface current have been tracked and recorded. Figure 4.24 shows the surface current of the MoS_2-GaAs Tai-Chi PCA with a laser power from 5 to 20 mW under a bias voltage between -25 V and 25 V.

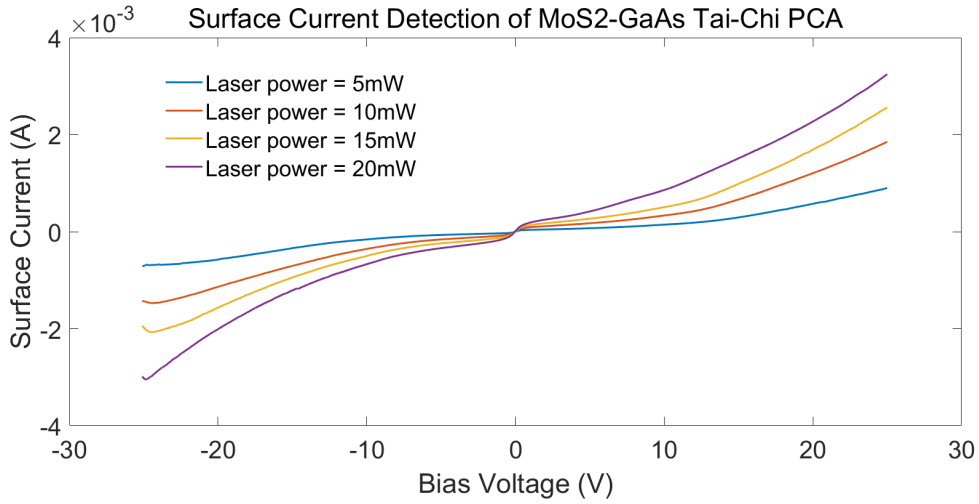

Figure 4.24: Surface current detection of MoS_2-GaAs Tai-Chi PCA with laser power between 5 and 20mW.

In Figure 4.25, it shows the comparison of the MoS_2-GaAs structure and non-MoS_2 Tai-Chi PCA with a laser power of 5 mW. The comparison of the MoS_2-GaAs structure and non-MoS_2 Tai-Chi PCA with a laser power of 10 mW is illustrated in Figure 4.26. Moreover, Figure 4.27 shows the comparison of the MoS_2-GaAs structure and non-MoS_2 Tai-Chi PCA with a laser power of 15 mW. The comparison between the two samples with a 20 mW laser is shown in Figure 4.28.

In these figures, the blue lines represent the surface current detected at the antenna gap of Tai-Chi PCA without MoS_2, and the orange lines represent the surface current on a Tai-Chi PCA with same electrodes and contact fingers but has a MoS_2-GaAs substrate. The bias voltage applied to the two PCAs are from -25 V to 25 V.

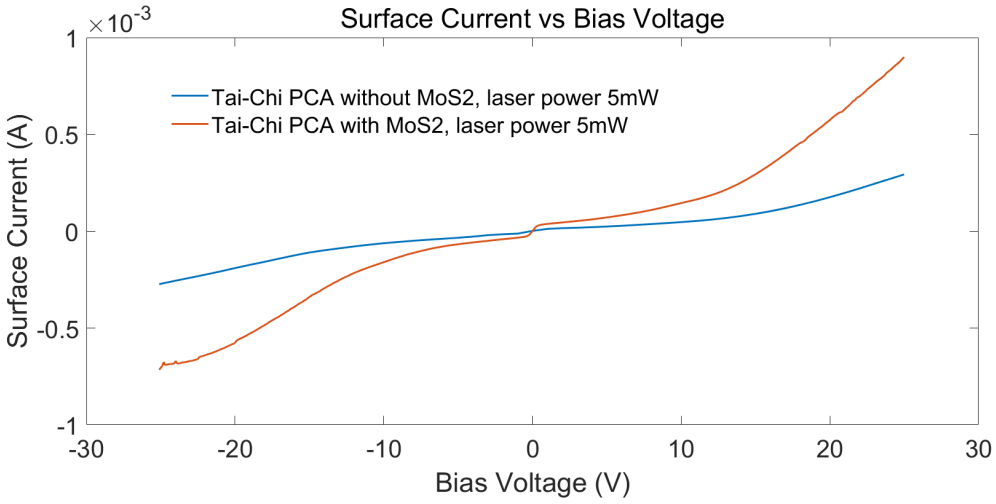

Figure 4.25: Comparisons of Tai-Chi PCA with/without MoS_2 under 5mW laser power.

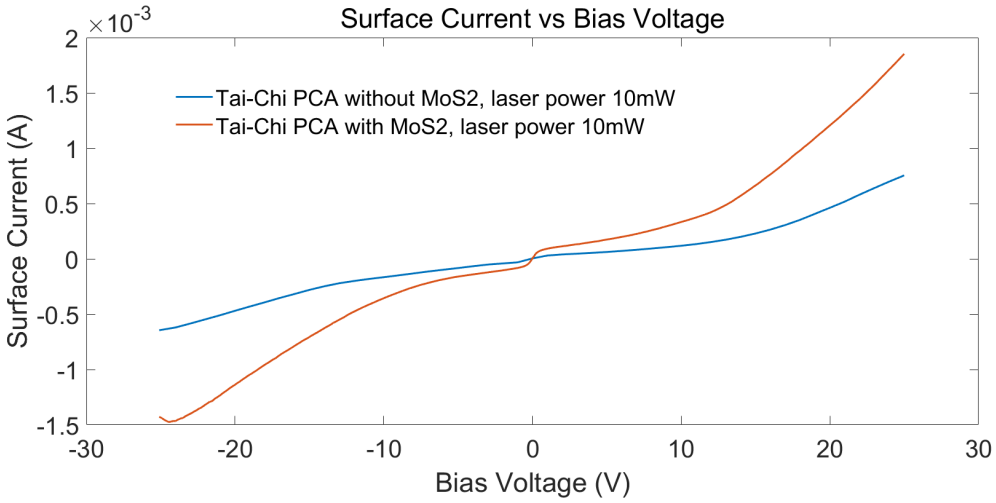

Figure 4.26: Comparisons of Tai-Chi PCA with/without MoS_2 under 10mW laser power.

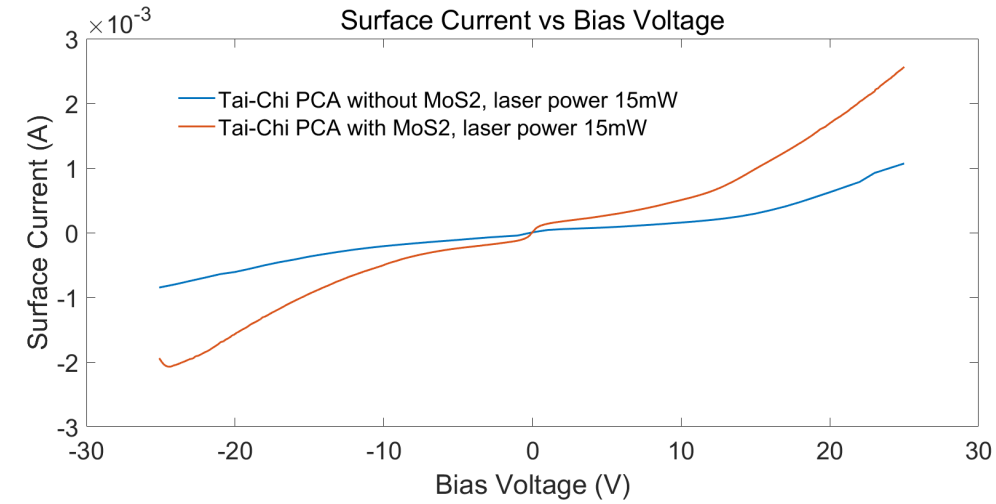

Figure 4.27: Comparisons of Tai-Chi PCA with/without MoS_2 under 15mW laser power.

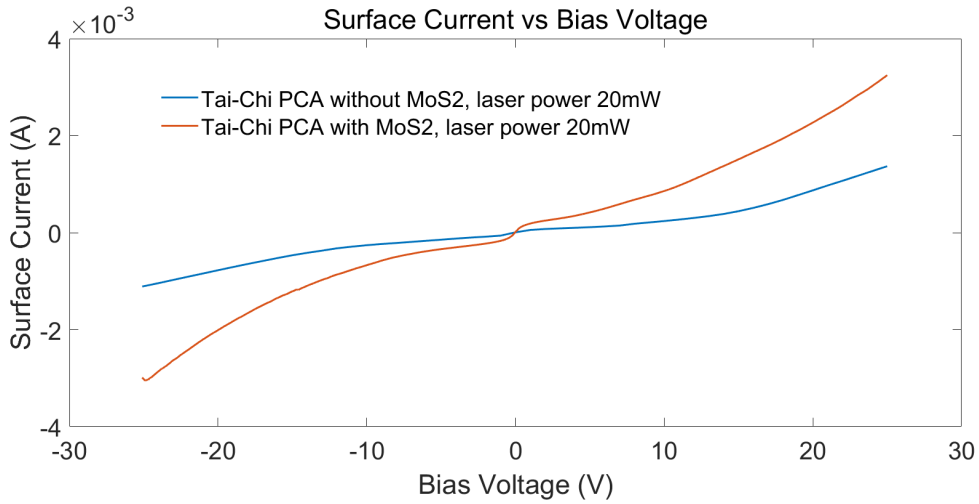

Figure 4.28: Comparisons of Tai-Chi PCA with/without MoS_2 under 20mW laser power.

These figures provide an obvious contrast of the surface current trend. Under different laser excitation, the MoS2-GaAs Tai-Chi PCA exhibits a larger surface current than the Tai-Chi PCA without MoS2, and the enhancement effect of the surface current becomes larger with the increase of the bias voltage. It has been detected that under 25 V bias voltage, the surface current at the gap of MoS_2-GaAs sample is 0.90 mA, 1.85 mA, 2.56 mA, and 3.25 mA, while the data of non-MoS_2 sample is 0.29 mA, 0.75 mA, 1.07 mA, and 1.37 mA. The laser power applied to these data is 5, 10, 15, 20 mW, respectively. Apart from the presence or absence of MoS_2, the two samples in the experiment are exactly the same. Both PCA samples have the same nanofingers and the same Tai-Chi electrodes, and the size and thickness of the SI-GaAs substrates are also the same. Through the experimental results, the enhancement of the surface current by MoS_2 has been successfully demonstrated. This confirms that the incorporation of MoS_2 has a significant positive effect on improving the performance of THz PCA.

Unfortunately, if we aim to obtain proper THz radiation, the size of the laser beam must not exceed the antenna gap. Otherwise, the detected THz radiation will be largely interfered with by noise, because the laser beam will cover non-gap area and cause unwanted radiation. In the progress of this PhD study, a suitable laser with 5 μm beam spot size has not yet been accessed, thus The THz radiation signals obtained from the MoS_2-GaAs based Tai-Chi PCA are chaotic. In future research, we plan to design and

fabricate an appropriate antenna mount with a lid that can cover the front side of PCA, leaving a 5 μm aperture precisely aligned with the PCA gap. This will ensure that only a 5 μm wide laser beam can pass through the lid and be focused at the antenna gap. Using this method, we can detect the proper THz signals from the proposed MoS_2-GaAs Tai-Chi PCA.

4.7 Summary

A Tai-Chi PCA based on MoS_2-GaAs and contact nanofingers is presented, simulated, fabricated and tested in this chapter. MoS_2-GaAs structure and plasmonic contact nanofingers enhance the optical-to-THz conversion efficiency, resulting in a high performance by the proposed work. Simulation results of the proposed PCA show that THz radiation power has been increased compared to reference PCA. The simulation on human skin shows that the PCA performs well at a depth of $\approx$ 0.4 - 1 mm from the human skin surface, indicating a good prospective of this design on skin cancer detection applications. The fabrication of the proposed PCA is completed in JWNC in the University of Glasgow, and corresponding measurements have been proceeded in Queen Mary University of London. Raman spectroscopy and SEM have been used in verifying the successful fabrication MoS_2-GaAs structure. Surface current measurement at the PCA gap shows that a higher current is achieved by the MoS_2-GaAs Tai-Chi PCA compared to the same PCA without MoS_2. It can be summarized that MoS_2 has enabled a promising direction on enhancement of THz PCA performance, putting itself as a valuable material in the research of optical-RF/MW antenna engineering. Moreover, we believe that this MoS_2-GaAs based Tai-Chi PCA can be regarded as a potential candidate for the future cancer detection and relative medical diagnoses conducted in the epidermis layer and the dermis layer.

Chapter 5

Large-Area Interdigitated PCA Design for Ultra-Wideband THz Emission

This chapter introduces a large-area THz PCA. Simulations and fabrication for this PCA has been conducted, and the PCA measurement has been proceeded using THz-TDS. Different the PCA designs in Chapter 4, this large-area THz PCA utilizes higher laser power pulse and larger laser beam spot to enhance the intensity of THz radiation.

5.1 Design of Large-Area Interdigitated PCA

Back to Chapter 2, Equation 2.1 determines the relationship between fluence, PCA gap area, and the incident laser power. For conventional PCAs with a gap of 5 - 10 μm, the laser power is too high, the fluence can exceed the limit (normally hundreds of $\mu J/cm^2$), resulting in a risk of damaging the PCA electrodes. Interdigitated PCAs extend the conventional PCA concept by spreading the PCA gap into numerous finger pairs and enable a much more powerful laser to excite the device on a larger area. Hence, the larger illuminated area provides the necessary condition for high laser beam spot size on the gap

area. While maintaining the fluence at a level that would not cause overheat of the PCA, higher laser power and larger excitation area allow the antenna to generate a increased photocurrent. Based on this, two large-area interdigitated PCAs are designed, fabricated and tested in this PhD study.

5.1.1 100 μm Interdigitated PCA Excited by Oscillator Laser

In order to verify the effect of large-area PCA on the enhancement of THz radiation, an interdigitated PCA using the same materials as the reference PCA has been designed in this section, and the gap between each parallel microstrips (sub-electrodes) is the same as the gap size of the reference PCA, which is 5 μm. The effective excitation length of each parallel microstrip is 100 μm, as shown in Figure 5.1. To distinguish this PCA design from another large-area PCA proposed in the next section, this PCA is referred to as the 100 μm interdigitated PCA. The excitation area size of the 100 μm interdigitated PCA fits the laser spot size of the THz laboratory at Queen Mary University of London. Therefore, this PCA is tested in QMUL. The fabrication and measurement of the 100 μm interdigitated PCA will be presented in the following sections. The dimensions of the electrodes have been illustrated in Figure 5.1, and the corresponding substrate is a 2 cm * 2 cm * 450 μm SI-GaAs chip.

5.1.2 Simulation Results of the 100 μm Interdigitated PCA

The simulation results of the interdigitated PCA is compared to the reference PCA mentioned in Chapter 3. In order to verify that the difference of the THz radiation performance between these two PCAs merely stems from the change in electrodes, the thickness and material of the substrate, as well as the thickness and material of the electrodes, remain unchanged in both simulation.

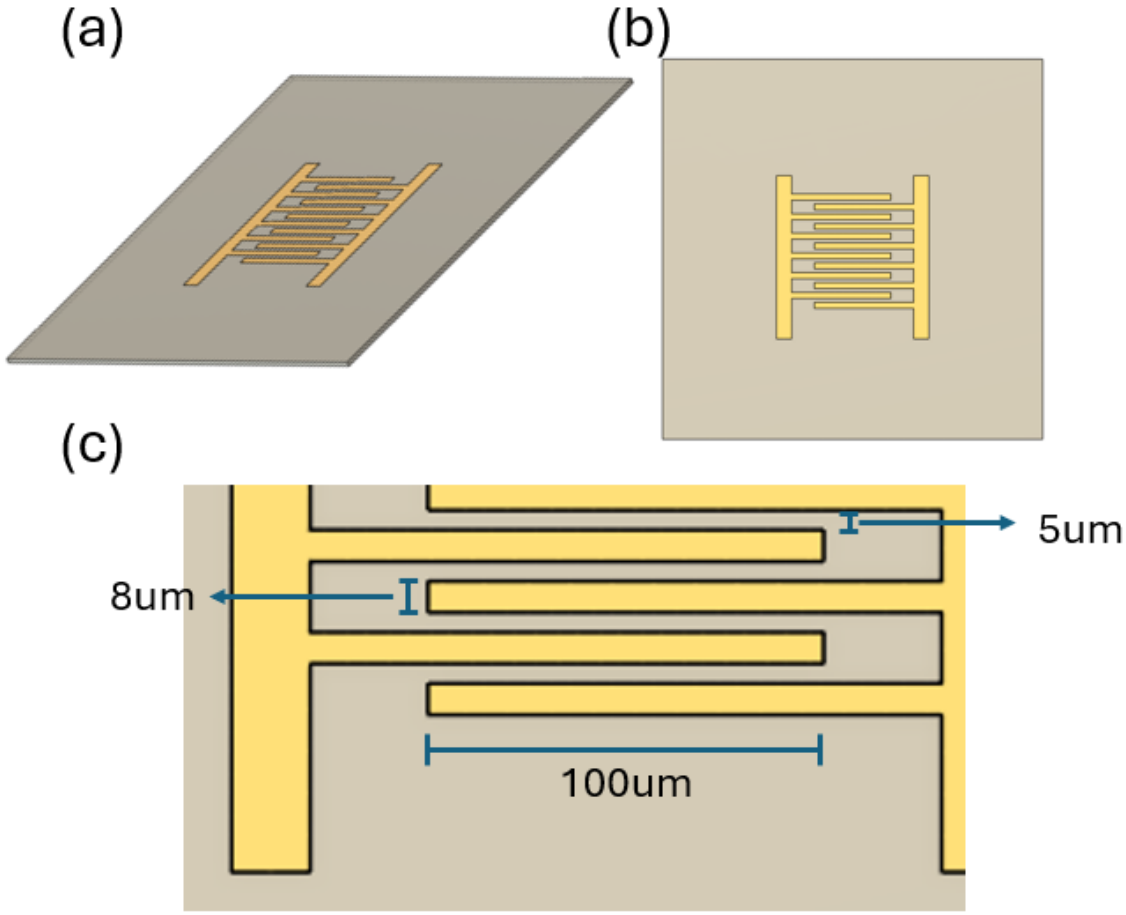

Figure 5.1: (a) Overall view and (b) Front view of the interdigitated PCA. (c) The dimensions of the sub-electrodes.

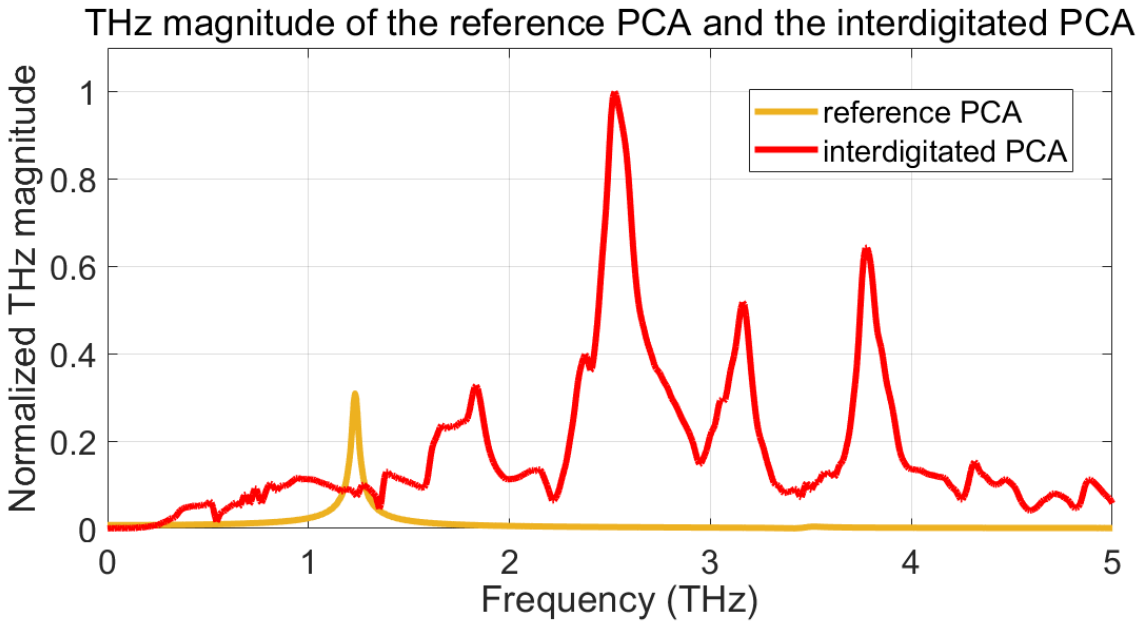

Figure 5.2: Magnitude of the radiated signal from the reference PCA (orange) and the interdigitated PCA (red).

Figure 5.2 shows the THz radiation magnitude of the interdigitated PCA and the reference PCA. It can be seen that the interdigitated electrodes have significantly enhanced the intensity of THz radiation. Furthermore, it can be observed that the bandwidth of the generated THz radiation has also increased. The frequency range of the reference PCA is between 1.1 - 1.4 THz, while the interdigitated electrodes have shown high radiation performance in the 1 - 4 THz frequency range.

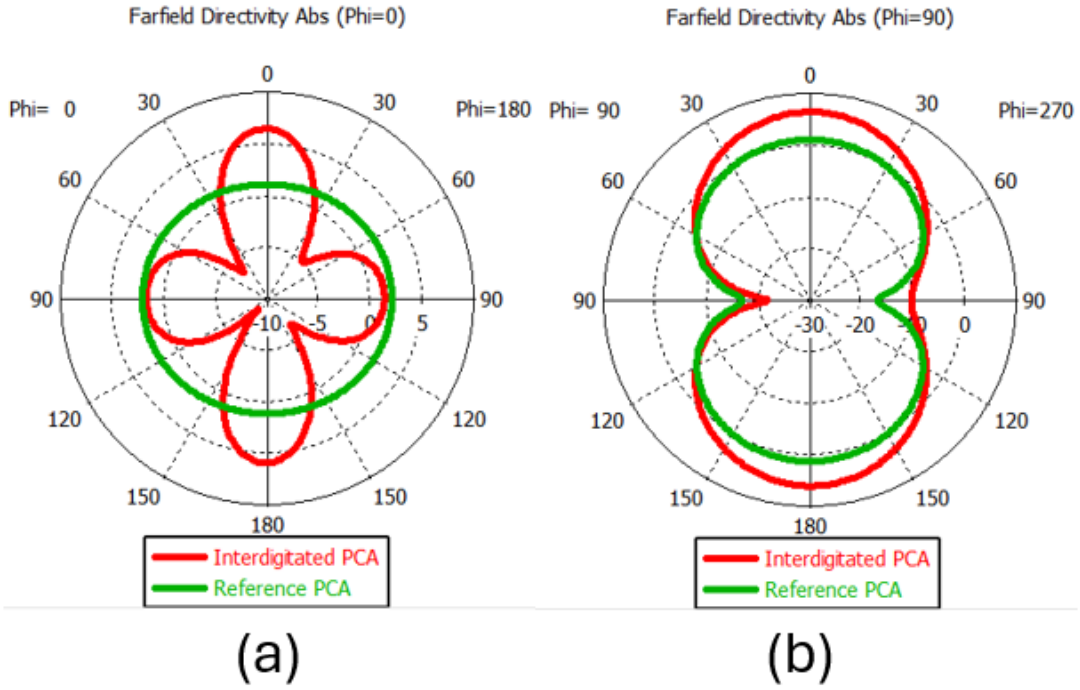

Figure 5.3: Comparison between the directivity of the reference PCA and the interdigitated PCA on (a) E plane and (b) H plane.

Figure 5.3 is the comparison figure of the farfield radiation pattern of the interdigitated PCA and the reference PCA. On E plane, the directivity of the interdigitated PCA is 6.42 dBi. On H plane, the 6.42 dBi data is the same. The angular width (3 dB) data on E and H plane is 35.7° and 60.6°, while the side lobe level is -0.6 dB. Compared to the results of the reference PCA (2.04 dBi on E plane and 1.08 dBi on H plane), the directivity is also increased to a large extent.

The E-field distribition is shown in Figure 5.4. It can be observed that the electric field is evenly distributed among the various sub-electrodes and radiates out from the back of the PCA. Due to the difference in PCA size, the E-field distribution figure is not compared with that of the reference PCA.

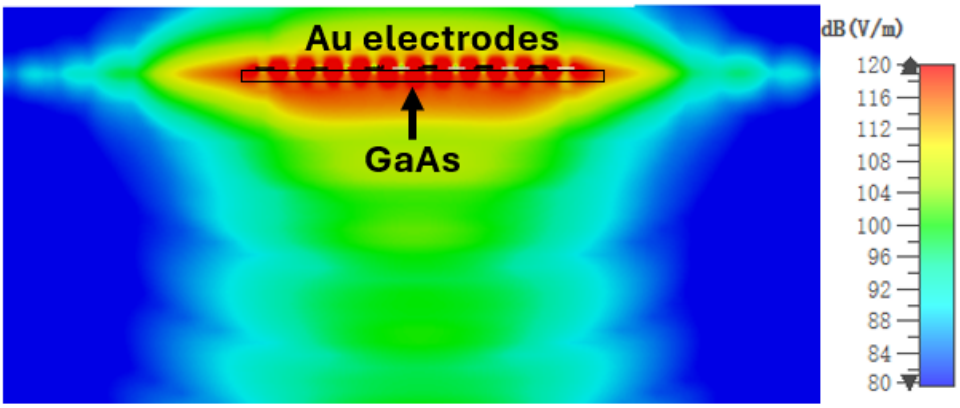

Figure 5.4: E-field distribution of the interdigitated PCA.

The simulation results show that by increasing the size of electrodes, the THz radiation of PCA can be enhanced, thereby improving the antenna performance. Another advantage of this method is that it is simple in theory and convenient in fabrication. Therefore, it has been selected as one of the methods for improving PCA performance in this PhD research.

5.2 2 mm Interdigitated PCA Excited by Amplifier Laser

In the literature review of this thesis, two types of excitation sources for THz PCAs are mentioned, which are amplifier laser and oscillator laser. Since the gap size of most PCAs is 5 - 50 μm, the amplifier laser is not applicable because it provides an excessive fluence which could easily damage the small electrodes. Therefore, all the PCAs mentioned in the previous chapters are applicable to oscillator excitation. However, in order to further

enhance THz radiation, a large-area PCA that can be excited by an amplifier laser has been proposed in this PhD research. Since the effective excitation length of each parallel microstrip is 2 mm, this PCA will be referred to as 2 mm interdigitated PCA. Figure 5.5 shows the overall view of the proposed 2 mm interdigitated PCA and the corresponding dimensions of the sub-electrodes.

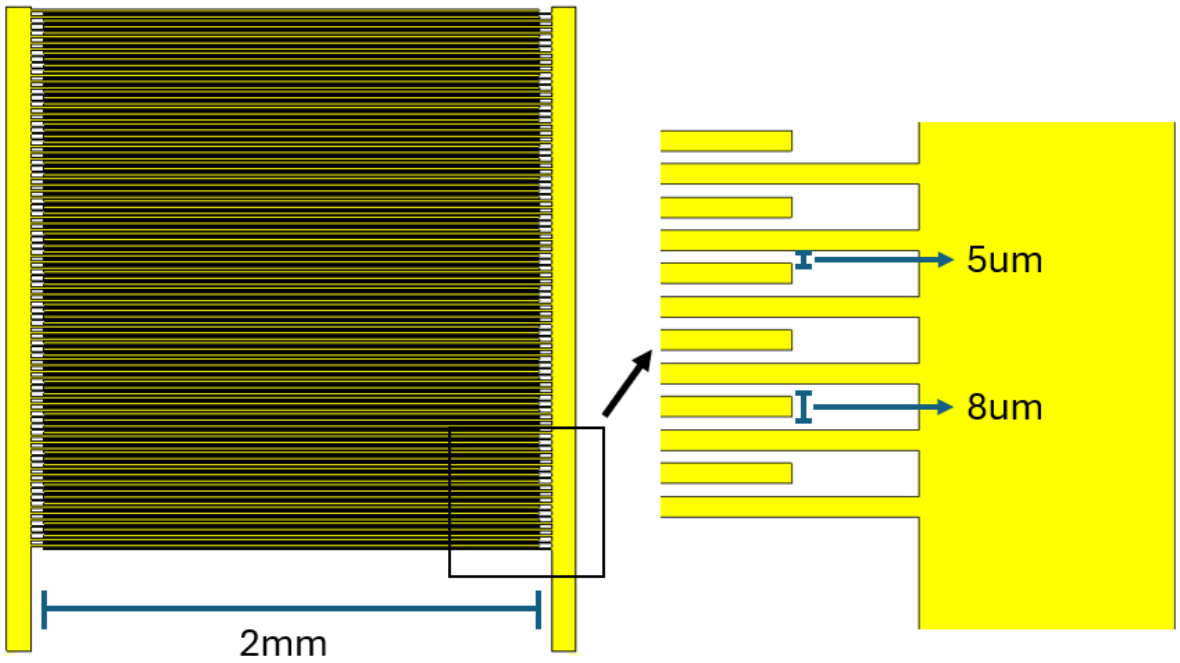

Figure 5.5: Overall view of the 2 mm interdigitated PCA and the dimensions of the sub-electrodes.

The simulation and fabrication of the 2 mm interdigitated PCA have been presented in the following sections, while not yet been tested by the time of the completion of this thesis, because the measurement of such a large PCA requires a high-power amplifier laser to excite. The measurement of the 2 mm interdigitated PCA is expected to be conducted at the University of Manchester using the 1 kHz amplifier laser system with a beam spot size of 3 mm.

5.3 Interdigitated PCA Fabrication

The fabrication of the 100 μm and 2 mm interdigitated PCAs are proceeded in JWNC in the University of Glasgow. Figure 5.6 shows the fabricated 100 μm interdigitated PCA under microscope. The two side strips is designed for connecting the PCA electrodes to bias voltage using silver conductive gel and wires. The silver conductive gel method has been introduced in previous chapters.

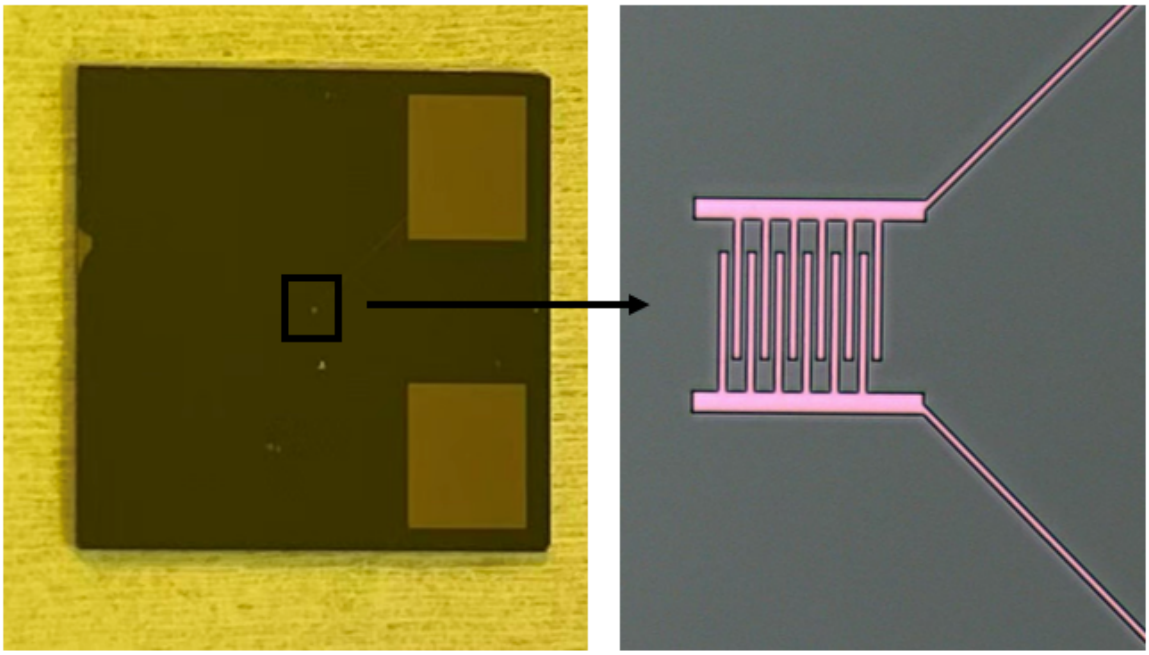

Figure 5.6: The 100 μm interdigitated PCA under microscope.

E-beam lithography process has been illustrated in Figure 3.11. 10/200 nm Ti/Au electrodes are deposited onto the SI-GaAs using Evap7 tool in JWNC. SEM pictures of the 100 μm interdigitated PCA is shown in Figure 5.7.

The fabricated 2 mm interdigitated PCA is shown in Figure 5.8 and Figure 5.9.

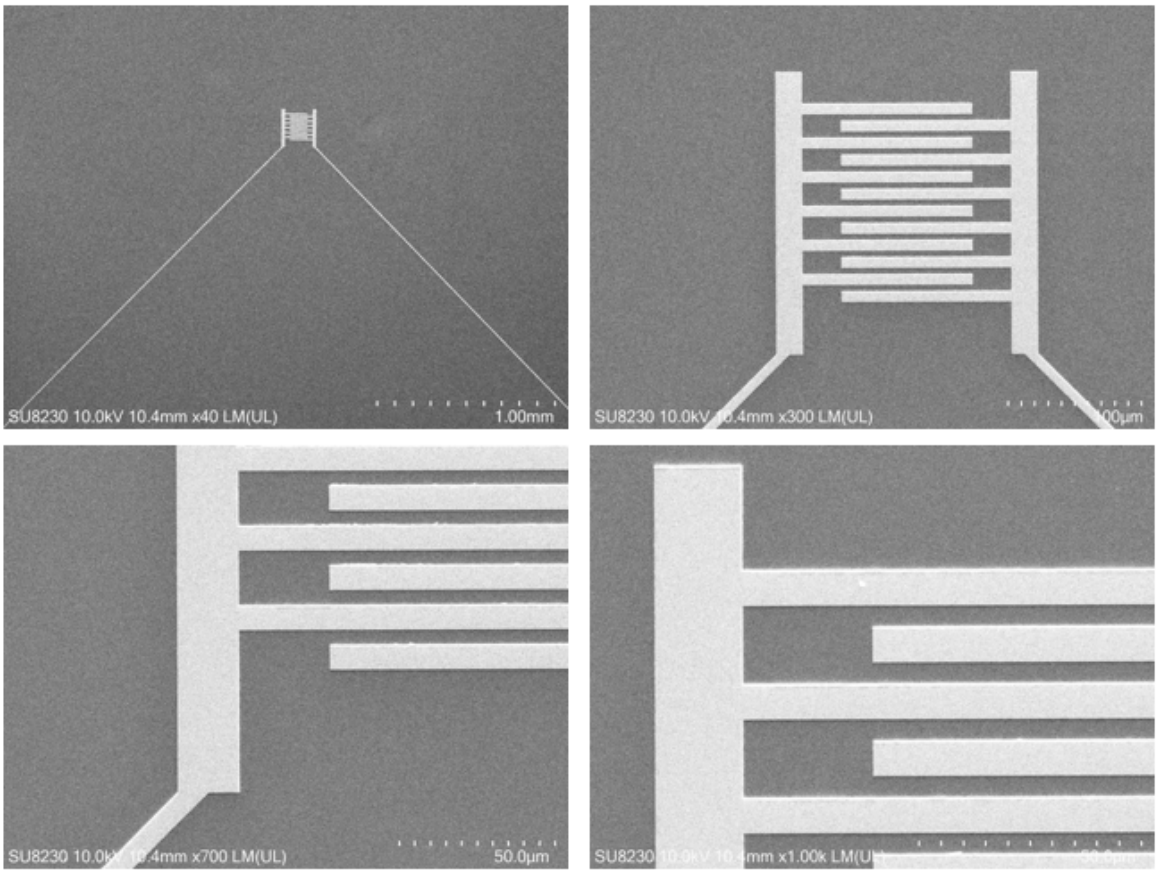

Figure 5.7: SEM pictures of the 100 μm interdigitated PCA.

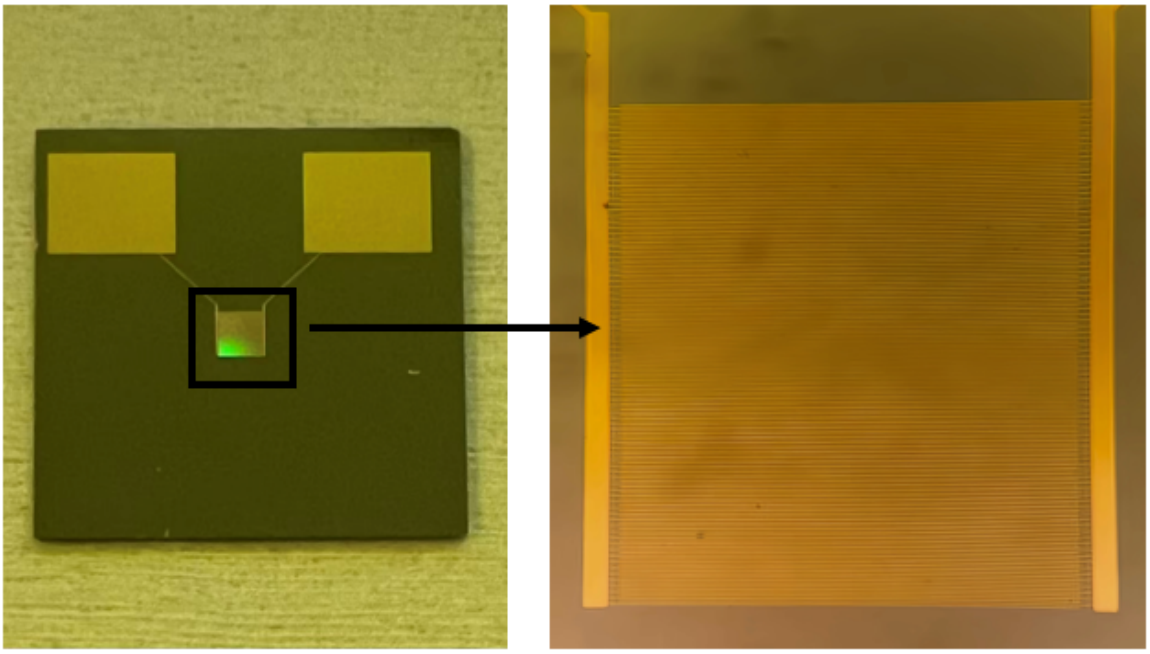

Figure 5.8: The 2 mm interdigitated PCA under microscope.

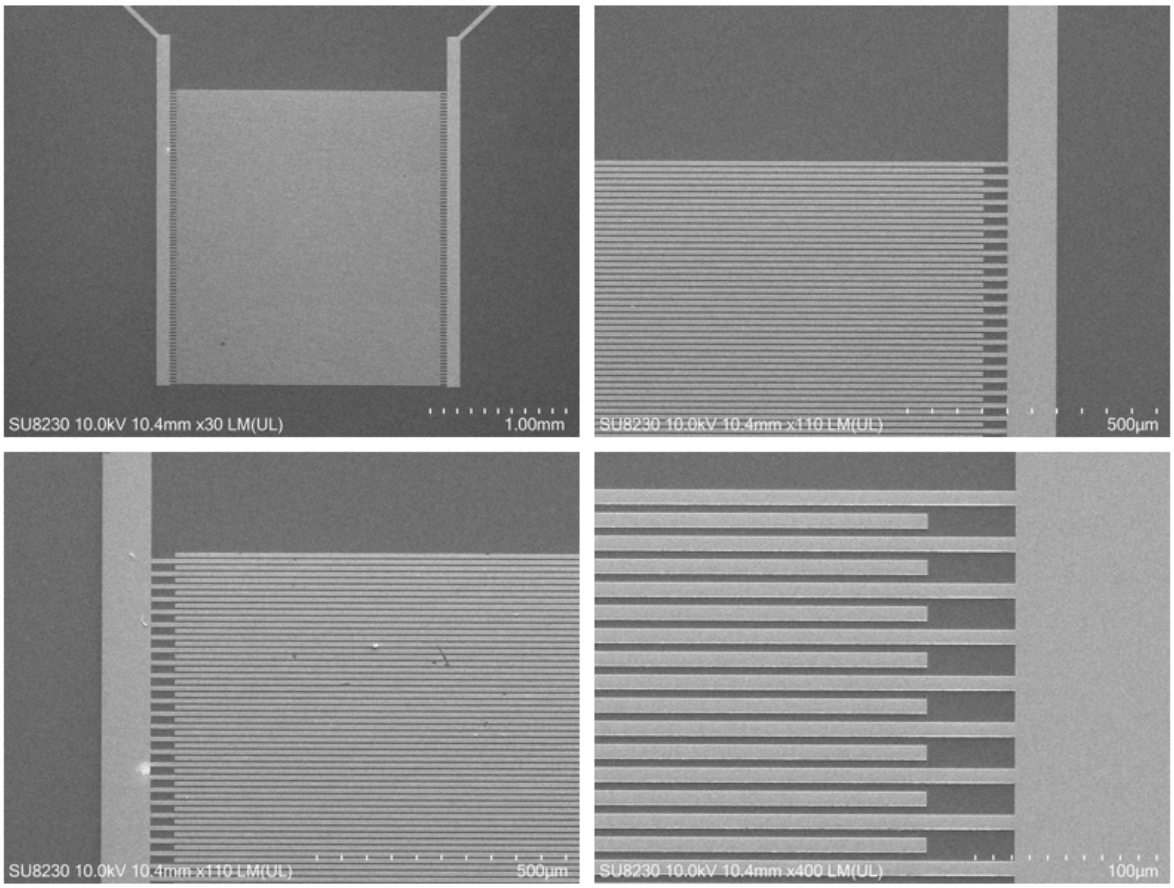

Figure 5.9: SEM pictures of the 2 mm interdigitated PCA

5.4 Measurement of the 100 μm Interdigitated PCA

The measurement of the 100 μm interdigitated PCA is completed in the THz-TDS system in QMUL. A schematic diagram of the measurement system is shown in Figure 5.10. The principle of the PCA measurement using a TDS has been introduced in Chapter 2.

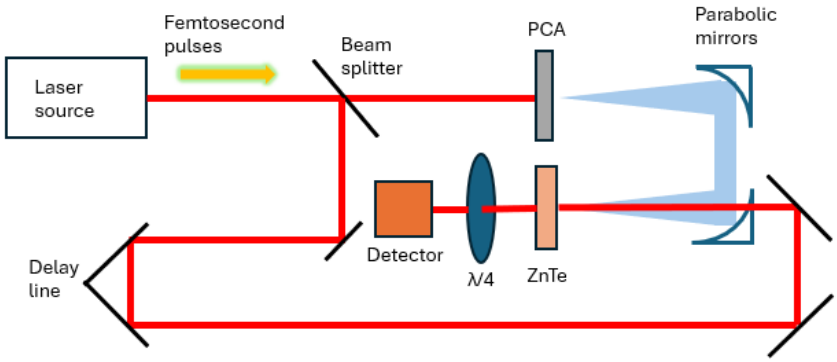

Figure 5.10: A schematic diagram of the THz-TDS system measuring the THz radiation emission from a photoemitter.

The 100 μm interdigitated PCA has been tested in QMUL using a 80 MHz, 200 mW oscillator laser beam. The beam spot size is adjusted to $\approx$ 100 μm to illuminate the entire active area of the PCA. The bias voltage applied to the PCA is 30 V. The radiated THz signal is detected by a ZnTe receiver. The radiated THz signal in time domain and the power spectrum are shown in Figure 5.11 (a) and (b). From the power spectrum figure, it can be observed that it is not until 3 THz that significant attenuation of the radiated THz signal occurs. After 4.2 THz, the radiation power shows a certain increase. Since the results of the ZnTe receiver in THz-TDS system are not accurate in the frequency bands over 3 THz [160], it cannot be regarded that the proposed 100 μm interdigitated PCA still generates efficient THz radiation after 4.2 THz. However, the operational frequency band of this antenna can cover 0.2 - 3 THz. Therefore, it can be concluded that the design of this 100 μm interdigitated PCA for ultra-wideband THz emission is successful.

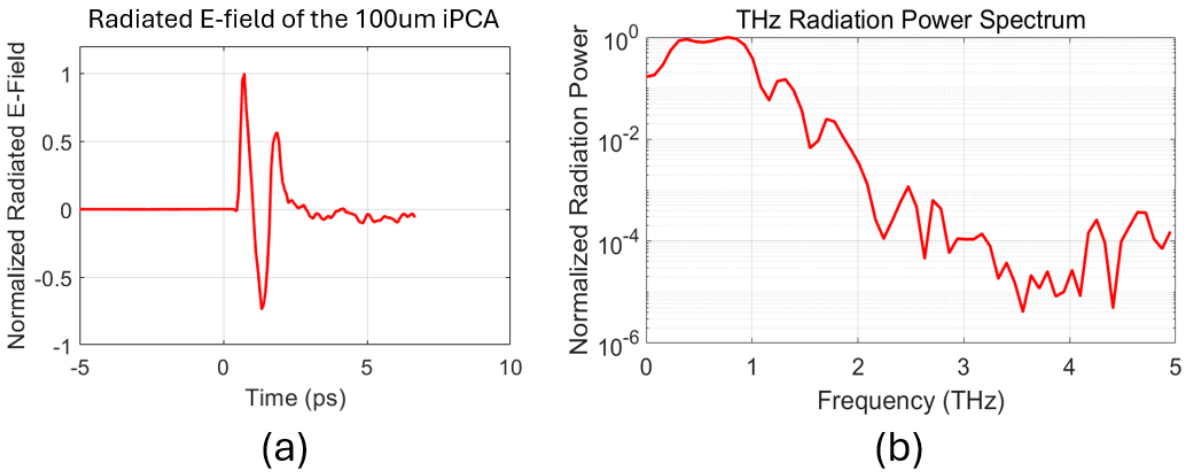

Figure 5.11: (a)Normalized radiated electric field in the time domain and (b)Radiated power spectrum in the frequency domain for the 100 μm interdigitated PCA. The laser pulse power is 200 mW and the bias voltage applied to the proposed PCA is 30 V.

The fluence under 200 mW oscillator laser can be calculated by Equation 2.1, which is 31.8 $\mu J/cm^2$. This fluence value has not reached the maximum value that an interdigitated PCA operates. Since the maximum power that the laser in the experimental system can achieve is 200 mW, it can be regarded that the proposed 100 μm interdigitated PCA can provide higher performance when stimulated by higher-power optical excitation.

In order to study the radiation performance of the proposed 100 μm interdigitated PCA, the measurement results of a large-aperture PCA with a PCA gap of 100 μm has been used for comparison. This large-aperture PCA provided by THz lab in QMUL is based on LT-GaAs substrate. Under the same laser and the same 30 V bias voltage, the contrast diagram of the radiated E-field (time domain) and the power spectrum (frequency domain) are shown in Figure 5.12 and Figure 5.13, respectively.

From the figures, it can be comcluded that the proposed 100 μm interdigitated PCA has similar THz radiation magnitude. The reference large-aperture PCA is based on LT-GaAs, and it is mounted on a specific designed PCA holder which provides more precise beam alignment. Also, the electrodes of the reference large-paerture PCA are connected to the bias voltage source through a more precise PCB circuit based on Au, the resistance from

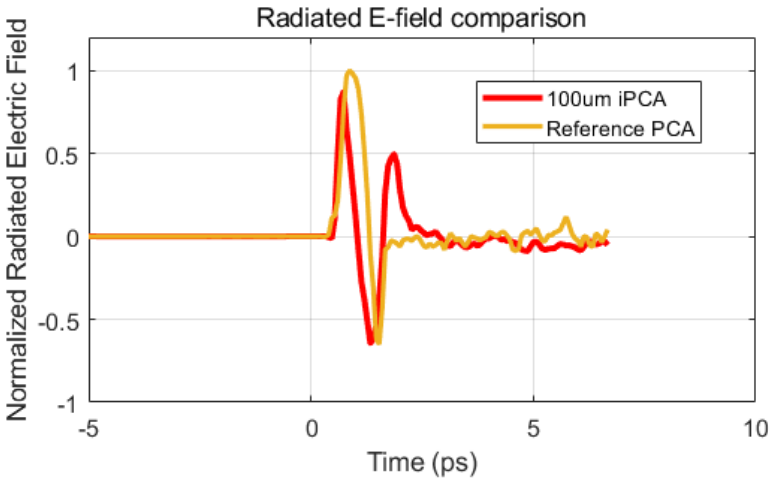

Figure 5.12: Normalized radiated electric field in the time domain of the 100 μm interdigitated PCA and the large-aperture PCA provided by QMUL. The red line is the proposed 100 μm interdigitated PCA, and the orange line is the reference large-aperture PCA. Both data are measured under same laser and bias voltage.

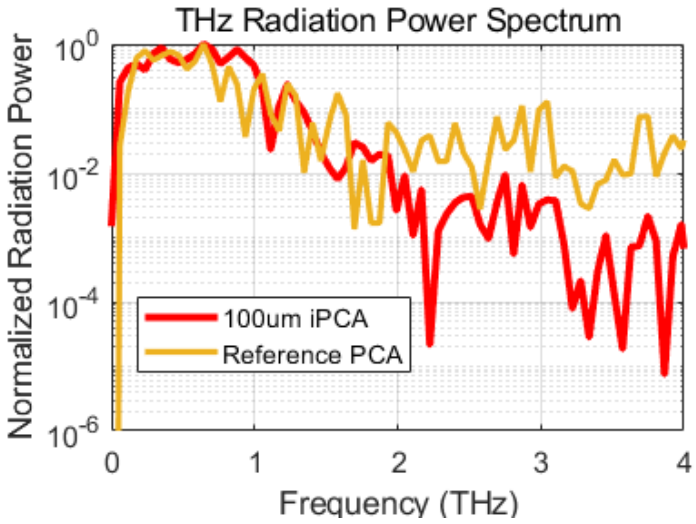

Figure 5.13: Radiated power spectrum in the frequency domain of the 100 μm interdigitated PCA and the large-aperture PCA provided by QMUL. The red line is the proposed 100 μm interdigitated PCA, and the orange line is the reference large-aperture PCA. Both data are measured under same laser and bias voltage.

the voltage source to the antenna electrodes is much smaller than that of our proposed 100 μm interdigitated PCA. Given that the proposed 100 μm interdigitated PCA still demonstrates similar performance under these objective conditions, it can be inferred that the performance of this proposed PCA is higher than the reference large-aperture PCA.

Due to time constraints, the additional tests that are originally planned for the two large-area interdigitated PCAs have not yet been completed. For example, the 2 mm interdigitated PCA requires to be measured using an amplifier laser excitation. These measurements will be carried out as future work.

5.5 Summary

In this chapter, the enhancement of PCA THz radiation using large-area electrodes have been fulfilled. The large-area interdigitated electrodes effectively expand the optical excitation area, allowing higher optical power to be applied. This structure enables stronger photocarrier generation hence improving THz radiation. A 100 μm interdigitated PCA and a 2 mm interdigitated PCA are presented and fabricated, and the experimental results of the former PCA is provided. The fabricated 100 μm interdigitated PCA is tested using 80 MHz oscillator optical pump with a 100 μm beam spot size and 200 mW optical power. The measurement results show a ultra-wideband operational frequency from 0.2 to 3 THz. This wide operational frequency range is considerable compared to reported conventional PCAs in different research. Due to the limited optical pumping power of the experimental device, the expected THz radiation of the proposed large-area interdigitated PCA will be further enhanced with higher-power laser compared to the measurement results provided in this chapter. A reference large-aperture PCA provided by QMUL lab has been measured as a comparison, and the analysis shows that the proposed 100 μm interdigitated PCA is expected to achieve higher performance under the same mounting conditions. The

outcome of this chapter not only demonstrates the significant improvement in PCA performance by large-are electrodes, but also contributes a ultra-wideband THz photoemitter to future THz technologies. The proposed large-area interdigitated PCA can serve as a potential THz emission source, providing a reference for future THz applications.

Chapter 6

Conclusion and Future Work

6.1 Conclusion

This PhD research aims to enhance the performance of THz PCA through structural and material innovations, and design, fabricate and test the proposed high-performance THz PCAs, thereby contributing to the advancement of THz PCA research and support future applications such as THz imaging and cancer detection. By integrating theoretical analysis, numerical simulation, and experimental fabrication, the work presented in this thesis provides a comprehensive exploration of multiple strategies for optimizing THz emission.

The research begins with a literature review of state-of-the-art PCA enhancement methods, including the introduction of novel materials, nano structures, large-area electrodes, and photonic structures. These theoretical investigations establish a solid foundation for subsequent experimental design, revealing the enhancement of optical-to-THz conversion efficiency and carrier generation within PCA gap. Building upon these research, several THz PCA designs have been developed and simulated. By analysis, advantages and challenges of each method are provided, among which MoS_2, plasmonic contact nanofingers,

large-area electrodes, and Si hyper hemispherical lens are selected and integrated into the proposed PCA structures. As a material rarely discussed in the field of PCAs, GQD is also applied in one of the proposed PCA designs in this PhD research, providing a valuable experimental case for future related studies.

In Chapter 3, A THz spiral PCA has been proposed and analyzed. Targeting on THz imaging for security inspection, this PCA is designed to work on a frequency range of 0.1 - 3 THz, and the peak performance is at 2.05 - 2.24 THz. The fabrication of this spiral PCA has been successfully proceeded in JWNC using E-beam lithograpy. SEM imaging confirms the high fabrication precision of these nanoscale features. GQD is employed to this spiral PCA design, and surface current measurement verifies that the photocurrent is enhanced by GQD. This experimental result is unprecedented in GQD-PCA research. Although the actual THz radiation has not been measured due to equipment limitations, this result demonstrates that GQD can increase the photocurrent within PCA gap, which is consistent with theoretical studies suggesting that GQDs can enhance carrier density. This outcome provides valuable experimental results, hence contributing to the development of GQD in the field of THz PCAs and related THz technologies.

In Chapter 4, A PCA based on novel geometric structure Tai-Chi has been proposed, and patterned monolayer MoS_2 flakes are utilized to enhance the optical-to-THz conversion efficiency. Aiming at detecting early-stage skin cancer that normally locate in epidermis, the Tai-Chi PCA is designed to have high radiation directivity, enabling it to precisely detect the potential tumour within epidermis tissues. The simulation results show that this design has good performance on the frequency range of 0.3 - 1.7 THz, and MoS2 successfully enhances the laser absorption at the PCA gap, thereby boosting the THz radiation. Furthermore, the simulation on a human skin model in CST indicates the PCA performs well at a depth of $\approx$ 0.4 - 1 mm from the human skin surface, showing a good prospective on skin cancer detection applications. The successful fabrication of the MoS_2-GaAs Tai-Chi PCA has been verified by Raman Spectroscopy and SEM. This Tai-Chi

PCA serves as a potential THz emitter for human skin cancer detection applications. Not only opening up the possibilities in medical diagnostics, this research also confirms the enhancement of THz PCAs by utilizing patterned MoS_2 monolayer, providing valuable and reliable insights for further studies in this field.

In Chapter 5, two large-area interdigitated PCAs are demonstrated. The results and analysis show that by expanding the optical excitation region, the PCA is capable to use high-power excitation, leading to stronger THz emission. The two large-area interdigitated PCAs are fabricated, and one of them has been tested. The experimental results highlight the advantages of using a large-area electrode structure to enhance emission. Moreover, the proposed ultra-wideband PCA emitter offers researchers in PCA field a reliable and promising direction.

Overall, this PhD research has advanced the understanding and development of high-performance THz PCAs through innovative structural design and material integration, and precise nano fabrication progress. The outcomes of this work not only enrich the theoretical research of THz technology but also provide valuable guidance for the design of next-generation THz sources in imaging, sensing, and medical applications.

6.2 Future Work

Future research will focus on further optimizing and experimentally validating of the performance of proposed PCAs in this PhD study. The next stage will include structural refinement and optimization of the MoS_2-based PCA, as well as completing measurements of its THz emission performance. Two measurement approaches are planned. The first approach is using a THz-TDS system equipped with 5 μm laser source. Inside-microscope is required in such THz-TDS system to ensure precise alignment of the laser spot and

the PCA gap. The second approach is to fabricate a PCA mount with a shielding lid containing a 5 μm aperture. In this setup, the PCA will be installed inside the mount, and the aperture will be positioned directly above the PCA gap, allowing 5 μm laser spot to pass through and excite the gap region. This design would enable the use of a larger laser beam while preserving excitation precision.

Further investigations will also explore the influence of GQD in enhancing THz emission of PCA, using the same experimental setup and measurement methods described above to evaluate the THz radiation output from more GQD-based PCA designs.

In addition, experiments will be conducted using an amplified laser source to measure the 2 mm interdigitated PCA, aiming to study the combined effect of large-area electrodes and high-power laser excitation on THz emission performance. These efforts will contribute to a deeper understanding of how geometric structure and optical power influence PCA radiation performance, and will provide practical insights for the design of next-generation high-power THz emitters.

Bibliography

[1] W. Hong et al. 'The Role of Millimeter-Wave Technologies of 5G/6G Wireless Communications'. In: *EEE Journal of Microwaves* (2021), pp. 101–122.

[2] M. Tonouchi. 'Cutting-edge terahertz technology'. In: *Nature Photonics* 1.2 (2007), pp. 97–105.

[3] S. Yadav, P. Lohia and D. K. Dwivedi. 'A novel Approach for Identification of Cancer Cells Using a Photonic Crystal Fiber-Based Sensor in the Terahertz Regime'. In: *Plasmonics* 18 (2023), pp. 1753–1769.

[4] Y.Lee. In: *Principles of terahertz science and technology*. Ed. by 1st ed. Springer, New York, 2008.

[5] H. Tabata. 'Application of terahertz wave technology in the biomedical field'. In: *IEEE Transactions on Terahertz Science and Technology* 5.6 (2015), pp. 1146–1153.

[6] J. A. Zeitler et al. 'Terahertz pulsed spectroscopy and imaging in the pharmaceutical setting – a review'. In: *Journal of Pharmacy and Pharmacology* 59.2 (2010), pp. 209–223.

[7] M. D. King, W. D. Buchanan and T. M. Korter. 'Understanding the terahertz spectra of crystalline pharmaceuticals: Terahertz spectroscopy and solid-state density functional theory study of (S)-(+)-ibuprofen and (RS)-ibuprofen'. In: *Journal of Pharmaceutical Sciences* 100.3 (2010), pp. 1116–1129.

[8] L. Ho, M. Pepper and P. Taday. 'Terahertz spectroscopy: signatures and fingerprints'. In: *Nature Photonics* 2 (2008), pp. 541–543.

[9] T. S. Rappaport et al. 'Wireless Communications and Applications Above 100 GHz: Opportunities and Challenges for 6G and Beyond'. In: *IEEE Access* (2019). 06 June 2019, pp. 78729–78757.

[10] A. Garufo et al. 'Leaky Lens Antenna as Optically Pumped Pulsed THz Emitter'. In: *2018 43rd International Conference on Infrared, Millimeter, and Terahertz Waves*. Nagoya, Japan, 2018.

[11] H. Pozniak. 'T-ray imaging gets under the skin: A method for analysing the structure of skin using a type of radiation known as T-rays could help improve the diagnosis and treatment of skin conditions'. In: *Engineering & Technology* 16.2 (2021), pp. 48–49.

[12] A. Banerjee, S. Vajandar and T. Basu. 'Prospects in medical applications of terahertz waves'. In: *Terahertz Biomedical and Heathcare Technologies: Materials to Device*. Ed. by Amit Banerjee et al. Vol. 16. 2. Elsevier, 2020, pp. 225–239.

[13] C. Wang and et al. 'An Efficient Algorithm Based on Frequency Scaling for THz Stepped-Frequency SAR Imaging'. In: *IEEE Transactions on Geoscience and Remote Sensing* 60 (2022), pp. 1–15.

[14] R. Asorey-Cacheda et al. 'Bridging Nano and Body Area Networks: A Full Architecture for Cardiovascular Health Applications'. In: *IEEE Internet of Things Journal* 10.5 (2023), pp. 4307–4323.

[15] E. Pickwell and V. P. Wallace. 'Biomedical applications of terahertz technology'. In: *Journal of Physics D: Applied Physics* 39.17 (2006).

[16] D. Li et al. 'Identification of early-stage cervical cancer tissue using metamaterial terahertz biosensor with two resonant absorption frequencies'. In: *IEEE Journal of Selected Topics in Quantum Electronics* 27.4 (2021), pp. 1–7.

[17] M. Gezimati and G. Singh. 'THz Imaging and Sensing for Healthcare: Current Status and Future Perspectives'. In: *IEEE Access* 11 (2023), pp. 18590–18619.

[18] M. Usman et al. 'Terahertz-Based Joint Communication and Sensing for Precision Agriculture: A 6G Use-Case'. In: *Frontiers in Communications and Networks* 3 (2022). 11 Mar 2022.

[19] S. Ansari et al. 'Urban air mobility—a 6G use case?' In: *Frontiers in Communications and Networks* 2 (2021). 27 Aug 2021.

[20] D. R. Bacon, J. Madeo and K. M. Dani. 'Photoconductive emitters for pulsed terahertz generation'. In: *Journal of Optics* 23.6 (2021), p. 064001.

[21] S. Ghorbani, M. Bashipour and M. Kolahdouz. 'Improving unbiased terahertz photoconductive antenna based on dissimilar Schottky barriers using plasmonic mode excitation'. In: *Optik* 194 (2019), p. 162975.

[22] D. Pavlidis. *Fundamentals of Terahertz Devices and Applications*. Florida: Wiley, 2021.

[23] A. Maestrini et al. 'Performance of a 1.2 THz frequency tripler using a GaAs frameless membrane monolithic circuit'. In: *2001 IEEE MTT-S International Microwave Symposium Digest*. Vol. 3. 2001, pp. 1657–1660.

[24] J. Tucek et al. 'A compact, high power, 0.65 THz source'. In: *IEEE International Vacuum Electronics Conference (IVEC)*. 2008, pp. 16–17.

[25] B. S. Williams. 'Terahertz quantum-cascade lasers'. In: *Nature Photonics* 1 (2007), pp. 517–525.

[26] Masahiro Asada and Satoshi Suzuki. 'Terahertz Emitter Using Resonant-Tunneling Diode and Applications'. In: *Sensors (Basel)* 21.4 (2021), p. 1384. DOI: 10.3390/s21041384.

[27] E. N. Boby et al. '6G and beyond: Investigation of broadband terahertz interdigitated photoconductive antenna by exploiting laser parameters'. In: *Microwave and Optical Technology Letters* 64 (2021), pp. 2197–2206.

[28] J. Bueno et al. 'Fabrication and Characterization of a Leacy-Lens Photoconductive Antenna on Low-Temperature Grown GaAs Merbranes'. In: *IEEE Transactions on Terahertz Science and Technology* 13.5 (2023), pp. 431–439.

[29] Z. T. Ma et al. 'Modulators for THz Communication: The Current State of the Art Research'. In: *Research* 2019 (2019), p. 6482975.

[30] D. M. Pozar. *Microwave Engineering*. 4th. Hoboken, NJ: Wiley, 2012.

[31] T. W. Crowe et al. 'Opening the terahertz window with integrated diode circuits'. In: *IEEE Journal of Solid-State Circuits* 40 (2005), pp. 2104–2110.

[32] R. J. Trew. 'High-frequency solid-state electronic devices'. In: *IEEE Transactions on Electron Devices* 52 (2005), pp. 638–649.

[33] H. Eisele and R. Kamoua. 'Submillimeter-wave InP Gunn devices'. In: *IEEE Transactions on Microwave Theory and Techniques* 52 (2004), pp. 2371–2378.

[34] H. Eisele. 'InP Gunn devices for 400-425 GHz'. In: *Electronics Letters* 42 (2006), pp. 358–359.

[35] N. Orihashi, S. Suzuki and M. Asada. 'One THz harmonic oscillation of resonant tunneling diodes'. In: *Applied Physics Letters* 87 (2005), p. 233501.

[36] R. Kohler et al. 'Terahertz semiconductor-heterostructure laser'. In: *Nature* 417 (2002), pp. 156–159.

[37] G. Scalari and J. Faist. '30 years of the quantum cascade laser'. In: *Communications Physics* 7 (2024), p. 394.

[38] D. H. Auston, K. P. Cheung and P. R. Smith. 'Picosecond photoconducting Hertzian dipoles'. In: *Applied Physics Letters* 45 (1984), pp. 284–286.

[39] Y. He et al. 'An overview of terahertz antennas'. In: *China Communications* 17.7 (2020), pp. 124–165.

[40] E. Isgandarov et al. 'Intense terahertz generation from photoconductive antennas'. In: *Frontiers of Optoelectronics* 14 (2021), pp. 64–93.

[41] N. Arora. 'Prospective Materials for Photoconductive Antennas for Terahertz Generation'. In: *Journal of Innovation and Social Science Research* 9.89 (2022), p. 110021.

[42] Newsijie Industry Research Center. *2022-2026 in-depth market research and investment strategy recommendation report of THz photoconductive antenna (PCA) industry*. Online. Accessed: 5 June 2025. 2022. URL: `https://www.163.com/dy/article/H0OFHRFK0514E30D.html`.

[43] P. K. Lu and M. Jarrahi. 'Frequency-domain terahertz spectroscopy using long-carrier-lifetime photoconductive antennas'. In: *Optics Express* 31.6 (2023), pp. 9319–9329.

[44] M. Bashirpour et al. 'Terahertz radiation enhancement in dipole photoconductive antenna on LT-GaAs using a gold plasmonic nanodisk array'. In: *Optics & Laser Technology* 120 (2019).

[45] N. Nissanov and G. Singh. 'Beamforming D-band phased array microstrip antennas'. In: *Science Direct* 3 (2022), p. 100196.

[46] R. Wang and et al. 'Interdigitated Photoconductive Antenna Pumped by Reconfigurable Structured Light for THz Emission and Modulation'. In: *IEEE Transactions on Microwave Theory and Techniques* 71.8 (2023), pp. 3661–3667.

[47] N. M. Burford and M. O. El-Shenawee. 'Review of Terahertz Photoconductive Antenna Technology'. In: *Optical Engineering* (2017), pp. 1–20.

[48] J. Liu and V. Nicolosi. 'When MXenes meet THz radiation'. In: *Nature Photonics* 31.6 (2023), pp. 556–557.

[49] P. S. Sachidanand et al. 'MoS2 nanostructures as transparant material: Optixal trasmittance measurements'. In: *Materials Today: Proceedings* 26.1 (2020), pp. 104–107.

[50] S. S. Sakar et al. 'Solution-processed MoS2 quantum dot/GaAs vertical heterostructure based self-powered photodetectors with superior detectivity'. In: *Nanotechnology* 31.13 (2020), p. 135203.

[51] S. Lepeshov et al. 'Enhancement of terahertz photoconductive antenna operation by optical nanoantennas'. In: *Laser & Photonics Reviews* 11.1 (2017), p. 1600199.

[52] V. Pacebutas and et al. 'THz time-domain-spectroscopy system based on femtosecond Yb:fiber laser and GaBiAs photoconucting components'. In: *Applied Physics Letters* 97 (2010), p. 031111.

[53] E. R. Brown, F. W. Auston and M. C. Nuss. 'Sub-picosecond photoconducting dipole antennas'. In: *IEEE Journal of Quantum Electronics* 24.2 (1988), pp. 255–260.

[54] K. G. Gan et al. 'Ultrahigh power-bandwidth-product performance of low-temperature-grown-GaAs based metal-semiconductor-metal travelling-wave photodetectors'. In: *Applied Physics Letters* 80.21 (2002), pp. 4054–4056.

[55] D. Ponomarev et al. 'Enhanced THz radiation through a thick plasmonic electrode grating photoconductive antenna with tight photocarrier confinement'. In: *Optics Letters* 48.6 (2023), pp. 1220–1223.

[56] D. Saeedkia. 'Terahertz photoconductive antennas: Principles and applications'. In: *Proceedings of the 5th European Conference on Antennas and Propagation*. Rome, Italy, 2011.

[57] J.A.Shaw. 'Radiometry and the friis transmission equation'. In: *American journal of physics* 81.1 (2013).

[58] A. Tamminen et al. 'Reflectarray design for 120-ghz radar application: measurement results'. In: *IEEE Transactions on Antennas and Propagation* 61.10 (2013).

[59] P. F. Goldsmith. *Quasioptical Systems: Gaussian Beam Quasioptical Propogation and Applications*. 2nd. Hoboken, NJ: Wiley-IEEE Press, 1998.

[60] X. Zhang et al. 'Performance Enhancement of Photoconductive Antenna Using Saw-Toothed Plasmonic Contact Electrode'. In: *Electronics* 10.21 (2021), pp. 2693–2702.

[61] N. I. Cabello and et al. 'Terahertz Emission Enhancement of Gallium-Arsenide-Based Photoconductive Antennas by Silicon Nanowire Coating'. In: *IEEE Transactions on Terahertz Science and Technology* 12.1 (2022), pp. 36–41.

[62] Y.-T. Li et al. 'Characterization of Sub-THz Photonic-Transmitters Based on GaAs–AlGaAs Uni-Traveling-Carrier Photodiodes and Substrate-Removed Broadband Antennas for Impulse-Radio Communication'. In: *IEEE Photonics Technology Letters* 20.16 (2008), pp. 1342–1344.

[63] V. Rathinasamy et al. 'Interdigitated photoconductive THz antenna for future wireless communications'. In: *Microwave and Optical Technology Letters* 64.12 (2022), pp. 2189–2196.

[64] B. Heshmat et al. 'Enhanced Terahertz Bandwidth and Power from GaAsBi-based Sources'. In: *Advanced Optical Materials* 1.10 (2013), pp. 714–719.

[65] A. Krotkus, A. Arlauskas and R. Adomavicius. 'Semiconductor Investigation by Terahertz Radiation Pulses'. In: *Proceedings of SPIE - The International Society for Optical Engineering*. 2012.

[66] M. Tani et al. 'Emission characteristics of photoconductive antennas based on low-temperature-grown GaAs and semi-insulating GaAs'. In: *Applied Optics* 36.30 (1997), pp. 7853–7859.

[67] M. R. Stone et al. 'Electrical and radiation characteristics of semilarge photoconductive terahertz emitters'. In: *IEEE Transactions on Microwave Theory and Techniques* 52.10 (2004), pp. 2420–2429.

[68] R. Stibal, J. Windscheif and W. Jantz. 'Contactless evaluation of semi-insulating GaAs wafer resistivity using the time-dependent charge measurement'. In: *Semiconductor Science and Technology* 6.10 (1991), p. 995.

[69] S. Gupta and et al. 'Subpicosecond carrier lifetime in GaAs grown by molecular beam epitaxy at low temperatures'. In: *Applied Physics Letters* 59.25 (1991), pp. 3276–3278.

[70] F. W. Smith et al. 'Picosecond GaAs-based photoconductive optoelectronic detectors'. In: *Applied Physics Letters* 54.10 (1989), pp. 890–892.

[71] Alexander Dohms et al. 'Rh-doped, InGaAs-based Quantum-Photoconductor with Superior Carrier Mobility-Lifetime Trade-off for THz Time-Domain Spectroscopy'. In: *Journal of Infrared, Millimeter, and Terahertz Waves* 46 (55 2025).

[72] S. J. Jo, S.-G. Ihn and J.-I. Song. 'Carrier dynamics of low-temperature-grown $In_{0.53}Ga_{0.47}As$ on GaAs using an InGaAlAs metamorphic buffer'. In: *Applied Physics Letters* 86.11 (2005), p. 111903.

[73] A. Takazato et al. 'Terahertz wave emission and detection using photoconductive antennas made on low-temperature-grown InGaAs with 1.56μm pulse excitation'. In: *Applied Physics Letters* 91.1 (2007), p. 011102.

[74] K. Piwowarski et al. 'Modeling of Changes in the Resistivity of Semi Insulating Gallium Phosphide under the Influence of Lighting'. In: *Energies* 16.4 (2023), p. 1725.

[75] E. Gaubas, M. Bauza and J. Vanhellemont. 'Carrier lifetime studies in Ge using microwave and infrared light techniques'. In: *Materials Science in Semiconductor Processing* 9.4-5 (2006), pp. 781–787.

[76] A. Singh et al. 'Gapless Broadband Terahertz Emission from a Germanium Photoconductive Emitter'. In: *ACS Photonics* 5.7 (2018), pp. 2718–2723.

[77] Ioffe Institute. *Properties of Germanium (Ge)*. Online. Accessed: 30 August 2025. 2025. URL: `https://www.ioffe.ru/SVA/NSM/Semicond/Ge/electric.html`.

[78] S. Bhunia and D. N. Bose. 'Microwave synthesis, single crystal growth and characterization of ZnTe'. In: *Journal of Crystal Growth* 186 (4 1998), pp. 535–542.

[79] M. Martin and E. R. Brown. 'Critical comparison of GaAs and InGaAs THz photoconductors'. In: *Proceedings of SPIE* 8261 (2012), p. 826102.

[80] S. L. Chuang. *Physics of Photonic Devices*. Hoboken: Wiley, 2009, p. 113.

[81] H. Nemec, A. Pashkin and P. Kuzel. 'Carrier dynamics in low-temperature grown GaAs studied by terahertz emission spectroscopy'. In: *Journal of Applied Physics* 90.3 (2001), pp. 1303–1306.

[82] C. Kadow et al. 'Self-assembled ErAs islands in GaAs for THz applications'. In: *Physica E: Low-dimensional Systems and Nanostructures* 7.1-2 (2000), pp. 97–100.

[83] R. Yano et al. 'Arsenic pressure dependence of carrier lifetime and annealing dynamics for low-temperature grown GaAs studied by pump–probe spectroscopy'. In: *Journal of Applied Physics* 94 (6 2003), pp. 3966–3971.

[84] Doo-Hyeb Youn et al. 'Effects of post-growth annealing on the structure and electro-optical properties of low-temperature grown GaAs'. In: *Journal of Applied Physics* 103 (12 2008), p. 123528.

[85] M. V. Afsar and K. J. Button. 'Millimeter wave dielectric properties of materials'. In: *Infrared and Millimeter Waves*. Vol. 12. Chapter 1. New York, USA: Academic Press, 1984.

[86] BATOP Optoelectronics. *PCA - Photoconductive Antenna*. Online. Accessed: 8 July 2025. 2024. URL: `https://www.batop.de/information/PCA_infos.html`.

[87] S. S. Gearhart and G. M. Rebeiz. 'A Monolithic 250 GHz Schottky-Diode Receiver'. In: *IEEE Transactions on Microwave Theory and Techniques* 42.12 (1994), pp. 2504–2511. DOI: `10.1109/22.339789`. URL: `https://doi.org/10.1109/22.339789`.

[88] Ning Zhu and Richard W. Ziolkowski. 'Photoconductive THz Antenna Designs with High Radiation Efficiency, High Directivity and High Aperture Efficiency'. In: *IEEE Transactions on Terahertz Science and Technology* 3.6 (Nov. 2013), pp. 721–730.

[89] Florian Formanek et al. 'Aspheric Silicon Lenses for Terahertz Photoconductive Antennas'. In: *Applied Physics Letters* 94.2 (2009), p. 021113.

[90] Qing Yu et al. 'All-Dielectric Meta-lens Designed for Photoconductive Terahertz Antennas'. In: *IEEE Photonics Journal* 9.4 (July 2017), pp. 1–9.

[91] P. M. Sberna et al. 'Leaky Lens Photo-Conductive Antennas on LT GaAs Membranes'. In: *Proceedings of the 2021 46th International Conference on Infrared, Millimeter and Terahertz Waves (IRMMW-THz)*. Chengdu, China, 2021, pp. 1–1.

[92] A. Neto. 'UWB, Non Dispersive Radiation From the Planarly Fed Leaky Lens Antenna—Part 1: Theory and Design'. In: *IEEE Transactions on Antennas and Propagation* 58.7 (2010), pp. 2238–2247.

[93] K. F. Mak and J. Shan. 'Photonics and optoelectronics of 2D semiconductor transition metal dichalcogenides'. In: *Nature Photonics* 10.4 (2016), pp. 216–226.

[94] Yu Le et al. 'Gap plasmon-enhanced photoluminescence of monolayer MoS2 in hybrid nanostructure'. In: *Chinese Physics B* 27.4 (2018), p. 047302.

[95] Chi Wang et al. 'Enhancing directivity of terahertz photoconductive antennas using spoof surface plasmon structure'. In: *New Journal of Physics* 24.7 (2022), p. 073046.

[96] Marco M. Furchi et al. 'Mechanisms of Photoconductivity in Atomically Thin MoS2'. In: *Nano Letters* 14.11 (2014), pp. 6165–6170.

[97] K. F. Mak et al. 'Atomically thin MoS2: a new direct-gap semiconductor'. In: *Physical Review Letters* 105 (2010), p. 136805.

[98] Z. Lin and et al. 'Defect engineering of two-dimensional transition metal dichalcogenides'. In: *2D Materials* 3 (2016), p. 022002.

[99] A. Castellanos-Gomez et al. 'Spatially resolved optical absorption spectroscopy of single- and few-layer MoS2 by hyperspectral imaging'. In: *Nanotechnology* 27 (2016), p. 115705.

[100] H. Shu et al. 'Greatly enhanced optical absorption of a defective MoS2 monolayer through oxygen passivation'. In: *ACS Applied Materials & Interfaces* 8 (2016), pp. 13150–13156.

[101] S. Das et al. 'Ultrafast transient sub-bandgap absorption of monolayer MoS2'. In: *Light: Science & Applications* 10 (2021), p. 27.

[102] Callum J. Docherty et al. 'Ultrafast transient terahertz conductivity of monolayer MoS2 and WSe2 grown by chemical vapor deposition'. In: *ACS Nano* 8.11 (2014), pp. 11147–11153.

[103] Yuanyuan Huang et al. 'Terahertz surface emission from layered MoS2 crystal: competition between surface optical rectification and surface photocurrent surge'. In: *The Journal of Physical Chemistry C* 122.1 (2018), pp. 481–488.

[104] Yujie Zhong et al. 'Tunable terahertz broadband absorber based on MoS2 ring-cross array structure'. In: *Optical Materials* 114 (2021), p. 110996.

[105] Z. Fei et al. 'Gate-tuning of graphene plasmons revealed by infrared nano-imaging'. In: *Nature* 487 (2012), pp. 82–85.

[106] M. Freitag et al. 'Photocurrent in graphene harnessed by tunable intrinsic plasmons'. In: *Nature Communications* 4 (2013), pp. 1–8.

[107] V. W. Brar et al. 'Electronic modulation of infrared radiation in graphene plasmonic resonators'. In: *Nature Communications* 6 (2015), pp. 1–7.

[108] M. Masyukov et al. 'Optically tunable terahertz chiral metasurface based on multilayered graphene'. In: *Scientific Reports* 10 (2020), p. 3157.

[109] S. P. Milovanovic and F. M. Peeters. 'Strained Graphene Structures: From Valleytronics to Pressure Sensing'. In: *NATO Science for Peace and Security Series A: Chemistry and Biology*. Dordrecht, Netherlands: Springer, 2018, pp. 3–17.

[110] J.-X. Liu et al. 'Effect of Graphene on the Sunlight Absorption Rate of Silicon Thin Film Solar Cells'. In: *Plasmonics* 14.2 (2019), p. 353.

[111] S.-Y. Wang et al. 'Interaction of electromagnetic waves with multilayer bi-anisotropic graphene structure'. In: *2013 USNC-URSI Radio Science Meeting (Joint with AP-S Symposium)*. Lake Buena Vista, USA, 2013, p. 53.

[112] Y. Shao, J.-J. Yang and M. Huang. 'A Review of Computational Electromagnetic Methods for Graphene Modeling'. In: *International Journal of Antennas and Propagation* 2016 (2016), p. 7478621.

[113] X.-H. Wang, W.-Y. Yin and Z. Chen. 'Broadband modeling surface plasmon polaritons in optically pumped and curved graphene structures with an improved leapfrog ADI-FDTD method'. In: *Optics Communications* 334 (2015), pp. 152–155.

[114] V. Nayyeri, M. Soleimani and O. M. Ramahi. 'Modeling graphene in the finite-difference time-domain method using a surface boundary condition'. In: *IEEE Transactions on Antennas and Propagation* 61.8 (2013), pp. 4176–4182.

[115] D.-W. Wang et al. 'Wideband modeling of graphene-based structures at different temperatures using hybrid FDTD method'. In: *IEEE Transactions on Nanotechnology* 14.2 (2015), pp. 250–258.

[116] V. W. Brar et al. 'Highly confined tunable mid-infrared plasmonics in graphene nanoresonators'. In: *Nano Letters* 13.6 (2013), pp. 2541–2547.

[117] J. Yang et al. 'Transmission properties and molecular sensing application of CGPW'. In: *Optics Express* 23.25 (2015), pp. 32289–32299.

[118] P. Burghignoli et al. 'Space-domain method of moments for graphene nanoribbons'. In: *Proceedings of the 8th European Conference on Antennas and Propagation (EuCAP '14)*. Hague, Netherlands, 2014.

[119] R. Araneo et al. 'Modal propagation and crosstalk analysis in coupled graphene nanoribbons'. In: *IEEE Transactions on Electromagnetic Compatibility* 57.4 (2015), pp. 726–733.

[120] A. Fallahi et al. 'Nonlocal electromagnetic response of graphene nanostructures'. In: *Physical Review B* 91 (2015), p. 121405.

[121] G. W. Hanson. 'Dyadic Green's functions and guided surface waves for a surface conductivity model of graphene'. In: *Journal of Applied Physics* 103.6 (2008), p. 064302.

[122] V. P. Gusynin, S. G. Sharapov and J. P. Carbotte. 'Magneto-optical conductivity in Graphene'. In: *Journal of Physics: Condensed Matter* 19 (2007), p. 026222.

[123] V. Ryzhii et al. 'Terahertz lasers based on optically pumped multiple graphene structures with slot-line and dielectric waveguides'. In: *Journal of Applied Physics* 107.5 (2010).

[124] F. T. Vasko and V. Ryzhii. 'Photoconductivity of intrinsic graphene'. In: *Physical Review B* 77.19 (2008).

[125] A. A. Dubinov et al. 'Terahertz surface plasmons in optically pumped graphene structures'. In: *Journal of Physics: Condensed Matter* 23.14 (2011).

[126] M. Zolfagharloo-Koohi and M. Neshat. 'Antenna efficiency in graphene-based THz photoconductive antennas'. In: *2014 22nd Iranian Conference on Electrical Engineering (ICEE)*. Tehran, Iran, 2015.

[127] R. Emadi et al. 'Analysis and Design of Photoconductive Antenna Using Spatially Dispersive Graphene Strips with Parallel-Plate Configuration'. In: *IEEE Journal of Selected Topics in Quantum Electronics* 24.2 (2018), pp. 1–9.

[128] S. Abadal et al. 'Graphene-Based terahertz antennas for area-constrained applications'. In: *2017 40th International Conference on Telecommunications and Signal Processing (TSP)*. Barcelona, Spain, 2017.

[129] A. G. Alharbi and V. Sorathiya. 'Ultra-Wideband Graphene-Based Micro-Sized Circular Patch-Shaped Yagi-like MIMO Antenna for Terahertz Wireless Communication'. In: *Electronics* 11.9 (2022), p. 1305.

[130] S. B. Amlashi et al. 'Surface Electromagnetic Performance Analysis of a Graphene-Based Terahertz Sensor Using a Novel Spectroscopy Technique'. In: *IEEE Journal on Selected Areas in Communications* 39.6 (2021), pp. 1797–1816.

[131] H. Wu and et al. 'High-Performance 3D-Graphene/GaAs Photodetectors for Applications in Logic Devices and Imaging Sensing'. In: *IEEE Electron Device Letters* 45.7 (2024), pp. 1245–1248.

[132] Mark D. Thomson et al. 'Coherent Terahertz Detection via Ultrafast Dynamics of Hot Dirac Fermions in Graphene'. In: *ACS Nano* 18.6 (2024), pp. 4765–4774.

[133] Long Xiao, Riccardo Degl' Innocenti and Zhiping Wang. 'Key Factors in Achieving High Responsivity for Graphene-Based Terahertz Detection'. In: *Advanced Photonics Research* 5.8 (2024).

[134] François Joint et al. 'Terahertz Antenna Impedance Matched to a Graphene Photodetector'. In: *ACS Applied Electronic Materials* 6.6 (2024), pp. 4819–4825.

[135] D. Zhang, Z. Xu, G. Cheng et al. 'Strongly Enhanced THz Generation Enabled by a Graphene Hot-Carrier Fast Lane'. In: *Nature Communications* 13 (2022), p. 6404.

[136] Ziyi Liu et al. 'Size Effect of Graphene Quantum Dots on Photoluminescence'. In: *Molecules* 26.13 (2021), p. 3922.

[137] J. Soleymani et al. 'Targeting and Sensing of Some Cancer Cells Using Folate Bioreceptor Functionalized Nitrogen-Doped Graphene Quantum Dots'. In: *International Journal of Biological Macromolecules* 118 (2018), pp. 1021–1034.

[138] A. El Fatimy, R. Myers-Ward, A. Boyd et al. 'Epitaxial Graphene Quantum Dots for High-Performance Terahertz Bolometers'. In: *Nature Nanotechnology* 11 (2016), pp. 335–338. URL: https://doi.org/10.1038/nnano.2015.303.

[139] S. Song et al. 'Terahertz Optical Properties and Carrier Behaviors of Graphene Oxide Quantum Dot and Reduced Graphene Oxide Quantum Dot via Terahertz Time-Domain Spectroscopy'. In: *Nanomaterials (Basel)* 13.13 (2023), p. 1948.

[140] L. Jiang et al. 'Patterning of Plasmonic Nanoparticles into Multiplexed One-Dimensional Arrays Based on Spatially Modulated Electrostatic Potential'. In: *ACS Nano* 5.10 (2011), pp. 8288–8294.

[141] C. W. Berry and M. Jarrahi. 'Terahertz Generation Using Plasmonic Photoconductive Gratings'. In: *New Journal of Physics* 14 (2012).

[142] G. Seniutinas et al. 'THz Photomixer with a 40nm-wide Nanoelectrode Gap on Low-temperature Grown GaAs'. In: *Micro/Nano Materials, Devices, and Systems*. Vol. 8923. 2013.

[143] J. A. Dionne et al. 'Planar Metal Plasmon Waveguides: Frequency-dependent Dispersion, Propagation, Localization, and Loss Beyond the Free Electron Model'. In: *Physical Review B* 72.7 (2005).

[144] B. Heshmat et al. 'Nanoplasmonic Terahertz Photoconductive Switch on GaAs'. In: *Nano Letters* 12.12 (2012), pp. 6255–6259.

[145] T. Ishi et al. 'Si Nano-photodiode with a Surface Plasmon Antenna'. In: *Japanese Journal of Applied Physics* 44.L364 (2005).

[146] L. Tang et al. 'Nanometre-scale Germanium Photodetector Enhanced by a Near-infrared Dipole Antenna'. In: *Nature Photonics* 2.4 (2008), pp. 226–229.

[147] J. Dintinger et al. 'Terahertz All-Optical Molecule-Plasmon Modulation'. In: *Advanced Materials* 18 (2006), pp. 1645–1648.

[148] C. W. Berry, J. Moore and M. Jarrahi. 'Design of Reconfigurable Metallic Slits for Terahertz Beam Modulation'. In: *Optics Express* 19.2 (2011), pp. 1236–1245.

[149] M. Unlu and M. Jarrahi. 'Miniature Multi-contact MEMS Switch for Broadband Terahertz Modulation'. In: *Optics Express* 22.26 (2014), pp. 32245–32260.

[150] M. Unlu et al. 'Switchable Scattering Metasurfaces for Broadband Terahertz Modulation'. In: *Scientific Reports* 16.4 (2014).

[151] M. R. M. Hashemi et al. 'Electronically-Controlled Beam-Steering through Vanadium Dioxide Metasurfaces'. In: *Scientific Reports* 6 (2016).

[152] S. Lepeshov et al. 'Boosting Terahertz Photoconductive Antenna Performance with Optimised Plasmonic Nanostructures'. In: *Scientific Reports* 8 (2018).

[153] N. T. Yardimci and M. Jarrahi. 'Nanostructure-Enhanced Photoconductive Terahertz Emission and Detection'. In: *Nano Micro Small* 14 (2018).

[154] A. Jooshesh et al. 'Nanoplasmonics Enhanced Terahertz Sources'. In: *Optics Express* 22.23 (2014), pp. 27992–28001.

[155] S.-G. Park et al. 'Terahertz Photoconductive Antenna with Metal Nanoislands'. In: *Optics Express* 20.23 (2012), pp. 25530–25535.

[156] S.-G. Park et al. 'Enhancement of Terahertz Pulse Emission by Optical Nanoantenna'. In: *ACS Nano* 6.3 (2012), pp. 2026–2031.

[157] C. W. Berry et al. 'Plasmonic photoconductive antennas for high-power terahertz generation and high-sensitivity terahertz detection'. In: *Proceedings of the 8th European Conference on Antennas and Propagation (EuCAP 2014)*. The Hague, Netherlands, 2014, pp. 2643–2646.

[158] S. B. Amlashi et al. 'An Efficient Plasmonic Photoconductive Antenna for Terahertz Continuous-Wave Applications'. In: *Proceedings of the 2021 15th European Conference on Antennas and Propagation (EuCAP)*. Dusseldorf, Germany, 2021.

[159] A. Jooshesh et al. 'Plasmon-Enhanced Below Bandgap Photoconductive Terahertz Generation and Detection'. In: *Nano Letters* 15.12 (2015).

[160] Nezih T. Yardimci et al. 'High-Power Terahertz Generation Using Large-Area Plasmonic Photoconductive Emitters'. In: *IEEE Transactions on Terahertz Science and Technology* 5.2 (2015), pp. 223–229.

[161] N. Khiabani et al. 'A Novel Sub-THz Photomixer with Nano-Trapezoidal Electrodes'. In: *IEEE Transactions on Terahertz Science and Technology* 4.4 (2014), pp. 501–508.

[162] Shang-Hua Yang and Mona Jarrahi. 'Enhanced light–matter interaction at nanoscale by utilizing high-aspect-ratio metallic gratings'. In: *Optics Letters* 38.18 (2013), pp. 3677–3679.

[163] C. W. Berry et al. 'High Power Terahertz Generation Using 1550 nm Plasmonic Photomixers'. In: *Applied Physics Letters* 104.7 (2014).

[164] C. Berry, N. Wang, M. Hashemi et al. 'Significant Performance Enhancement in Photoconductive Terahertz Optoelectronics by Incorporating Plasmonic Contact Electrodes'. In: *Nature Communications* 4 (2013), p. 1622.

[165] N. T. Yardimci and M. Jarrahi. 'High Sensitivity Terahertz Detection through Large-Area Plasmonic Nano-Antenna Arrays'. In: *Scientific Reports* 7 (2017).

[166] Mona Jarrahi. 'Advanced Photoconductive Terahertz Optoelectronics Based on Nano-Antennas and Nano-Plasmonic Light Concentrators'. In: *IEEE Transactions on Terahertz Science and Technology* 5.3 (2015), pp. 391–397.

[167] P. K. Lu et al. 'Carrier Dynamics in Semiconductors Studied with Time-Resolved Terahertz Spectroscopy'. In: *Reviews of Modern Physics* 83 (2011), pp. 543–586.

[168] O. A. Castañeda-Uribe et al. 'Comparative Study of Equivalent Circuit Models for PCAs: Screening Effect and Saturation'. In: *Optics Express* 26.22 (2018), pp. 29017–29032.

[169] V. V. Kononenko et al. 'A Diamond Terahertz Large Aperture Photoconductive Antenna Biased by a Longitudinal Field'. In: *Photonics* 10.10 (2023), p. 1169.

[170] E. R. Brown et al. 'Milliwatt Output Levels and Superquadratic Bias Dependence in a Low-Temperature-Grown GaAs Photomixer'. In: *Applied Physics Letters* 64 (1994), pp. 3311–3313.

[171] M. Awad et al. 'Characterization of Low Temperature GaAs Antenna Array Terahertz Emitters'. In: *Applied Physics Letters* 91 (2007), p. 181124.

[172] T. Hattori et al. 'Intense Terahertz Pulses from Large-Aperture Antenna with Interdigitated Electrodes'. In: *Japanese Journal of Applied Physics* 45 (2006), pp. L422–L424.

[173] N. V. Zenchenko et al. 'Enhanced Terahertz Emission in a Large-Area Photoconductive Antenna through an Array of Tightly Packed Sapphire Fibers'. In: *Applied Physics Letters* 124.12 (2024), p. 121107.

[174] S. Winnerl et al. 'Generation and Detection of THz Radiation With Scalable Antennas Based on GaAs Substrates With Different Carrier Lifetimes'. In: *IEEE Journal of Selected Topics in Quantum Electronics* 14.2 (2008), pp. 449–457.

[175] Richard Faulks et al. 'Enhanced Terahertz Receiver Using a Distributed Bragg Reflector Coupled to a Photoconductive Antenna'. In: *IEEE Photonics Technology Letters* 21.21 (2009), pp. 1603–1605.

[176] Y. Wang et al. 'Optimised THz photoconductive devices based on low-temperature grown III–V compound semiconductors incorporating distributed Bragg reflectors'. In: *IET Optoelectronics* 11.2 (2017), pp. 53–57.

[177] T. A. Birks, J. C. Knight and P. S. Russell. 'Endlessly Single-Mode Photonic Crystal Fiber'. In: *Optics Letters* 22 (1997), pp. 961–963.

[178] E. Rahmati and M. Ahmadi-Boroujeni. 'Improving the Efficiency and Directivity of THz Photoconductive Antennas by Using a Defective Photonic Crystal Substrate'. In: *Optics Communications* 412 (2018), pp. 74–79.

[179] M. Shalini and M. Ganesh Madhan. 'Photoconductive Bowtie Dipole Antenna Incorporating Photonic Crystal Substrate for Terahertz Radiation'. In: *Optics Communications* 517 (2022), p. 128327. DOI: 10.1016/j.optcom.2022.128327.

[180] I. Malhotra, K. R. Jha and G. Singh. 'Design of Highly Directive Terahertz Photoconductive Dipole Antenna Using Frequency-Selective Surface for Sensing and Imaging Applications'. In: *Journal of Computational Electronics* 17 (2018), pp. 1721–1740.

[181] *T-Ray 5000 TCU*. Accessed: 2025-11-01. 2007. URL: https://file.yizimg.com/15397/20161116-114120271.pdf.

[182] Hua Wei. 'The Prospects for T-Hz Detection Techniques Development'. In: *Infrared Technology* 32.4 (2010), pp. 231–234.

[183] Hisamatsu Nakano et al. 'A Spiral Antenna Backed by a Conducting Plane Reflector'. In: *IEEE Transactions on Antennas and Propagation* 34.6 (1986), pp. 791–796.

[184] Vaisshale Rathinasamy et al. 'Interdigitated Photoconductive Terahertz Antenna for Future Wireless Communications'. In: *Microwave and Optical Technology Letters* 64.12 (2022), pp. 2189–2196.

[185] A. Dhiflaoui, A. Yahyaoui, J. Yousaf et al. 'Numerical Analysis of Wideband and High Directive Bowtie THz Photoconductive Antenna'. In: *Applied Computational Electromagnetics Society Journal* 35.6 (2020), pp. 662–673.

[186] Rajita Ramanarayanan, Fadeela Chundekat Ummer and Sindhu Swaminathan. 'Exploring dynamics of resonance energy transfer in hybrid Quantum Dot Sensitized Solar Cells (QDSSC)'. In: *Materials Research Express* 7.2 (2020), p. 025517.

[187] Cecil S. Joseph et al. 'Continuous wave terahertz transmission imaging of non-melanoma skin cancers'. In: *Lasers in Surgery and Medicine* 43.6 (Aug. 2011), pp. 457–462.

[188] Hua Chen et al. 'The Diagnosis of Human Liver Cancer by using THz Fiber-Scanning Near-Field Imaging'. In: *Chinese Physics Letters* 30.3 (Mar. 2013), p. 030702. DOI: 2.

[189] Anthony J. Fitzgerald et al. 'Terahertz pulsed imaging of human breast tumors'. In: *Radiology* 239.2 (May 2006), pp. 533–540.

[190] Dibo Hou et al. 'Terahertz spectroscopic investigation of human gastric normal and tumor tissues'. In: *Physics in Medicine & Biology* 59.18 (Sept. 2014), pp. 5423–5440.

[191] Leila H. Eadie et al. 'Optimizing multi-dimensional terahertz imaging analysis for colon cancer diagnosis'. In: *Expert Systems with Applications* 40.6 (May 2013), pp. 2043–2050.

[192] Kalyan Kundu and N. N. Pathak. 'Terahertz Technology and Its Importance in the Field of Biomedical Application: A Review'. In: *Next Generation Wireless Communication*. Ed. by M. El Ghzaoui et al. Signals and Communication Technology. Cham: Springer, 2024.

[193] Cormac Flynn, Andrew Taberner and Poul Nielsen. 'Modeling the Mechanical Response of *in vivo* Human Skin under a Rich Set of Deformations'. In: *Annals of Biomedical Engineering* 39.7 (2011), pp. 1935–1946.

[194] Stanislav I. Alekseev and Marvin C. Ziskin. 'Human Skin Permittivity Determined by Millimeter Wave Reflection Measurements'. In: *Bioelectromagnetics* 28.5 (2007), pp. 331–339.

[195] EdrawSoft. *Template 1005968*. Accessed October 2, 2025. 2025. URL: `https://www.edrawmax.com/templates/1005968/` (visited on 02/10/2025).

[196] Samuel E. Lynch, Robert B. Colvin, Harry N. Antoniades et al. 'Growth Factors in Wound Healing: Single and Synergistic Effects on Partial Thickness Porcine Skin Wounds'. In: *The Journal of Clinical Investigation* 84.2 (1989), pp. 640–646.

[197] K. M. Yaws, D. G. Mixon and W. P. Roach. 'Electromagnetic Properties of Tissue in the Optical Region'. In: *Optical Interactions with Tissue and Cells XVIII*. Vol. 6435. SPIE. International Society for Optics and Photonics, 2007, p. 643507.

[198] Emma Pickwell et al. 'Simulation of Terahertz Pulse Propagation in Biological Systems'. In: *Applied Physics Letters* 84.12 (2004), pp. 2190–2192.

[199] Matthias Walther et al. 'Terahertz Conductivity of Thin Gold Films at the Metal–Insulator Percolation Transition'. In: *Physical Review B* 76.12 (2007), p. 125408.

[200] Harold A. Wheeler. 'Formulas for the Skin Effect'. In: *Proceedings of the IRE* 30.9 (1942), pp. 412–424.

[201] Xianding Yan et al. 'Dielectric Property of MoS_2 Crystal in Terahertz and Visible Regions'. In: *Applied Optics* 54.22 (2015), pp. 6732–6736.

[202] MCR Nano. *Raman Spectrum of Molybdenum Disulfide (MoS2)*. Accessed: 2025-10-16. n.d. URL: https://www.mcrnano.com/post/raman-spectrum-of-molybdenum-disulfide-mos2?srsltid=AfmBOoqNHsBSRcRXbx_Axmva8u0nlNqgeJ2rN3kX0